OBSERVATIONS OF INTERNAL WAVES IN THE UPPER OCEAN

Robert Pinkel

Scripps Institution Of Oceanography

Prepared for:

Office of Naval Research
Advanced Research Projects Agency

1 May 1975

MARINE PHYSICAL LABORATORY
of the Scripps Institution of Oceanography
San Diego, California 92132

OBSERVATIONS OF INTERNAL WAVES IN THE UPPER OCEAN

Robert Pinkel

Sponsored by
Advanced Research Projects Agency
ARPA Order Number 2185
Program Code Number 1N10

Contract N00014-69-A-0200-6041
Contract Effective Date: 1 April 1972
Contract Expiration Date: 1 August 1975
Amount of Contract: $1,573,332

Scientific Officer: Director, Undersea Programs
Office of Naval Research, Applications & Analysis Division
Department of the Navy, 800 N. Quincy Street, Arlington, Virginia 22217

Principal Investigator: F.N. Spiess/V.C. Anderson
(714) 452-2304

1 May 1975

SIO REFERENCE 75-10

UNCLASSIFIED

SECURITY CLASSIFICATION OF THIS PAGE (When Data Entered)

REPORT DOCUMENTATION PAGE		READ INSTRUCTIONS BEFORE COMPLETING FORM
1. REPORT NUMBER SIO Reference 75-10	2. GOVT ACCESSION NO.	3. RECIPIENT'S CATALOG NUMBER AD-A013 337
4. TITLE (and Subtitle) OBSERVATIONS OF INTERNAL WAVES IN THE UPPER OCEAN		5. TYPE OF REPORT & PERIOD COVERED Summary
		6. PERFORMING ORG. REPORT NUMBER MPL-U-36/75
7. AUTHOR(s) Robert Pinkel		8. CONTRACT OR GRANT NUMBER(s) N00014-69-A-0200-6041 NR 260-104
9. PERFORMING ORGANIZATION NAME AND ADDRESS University of California, San Diego, Marine Physical Laboratory of the Scripps Institution of Oceanography, San Diego, California 92132		10. PROGRAM ELEMENT, PROJECT, TASK AREA & WORK UNIT NUMBERS
11. CONTROLLING OFFICE NAME AND ADDRESS Office of Naval Research, Code 210, Department of the Navy, Arlington, Virginia 22217		12. REPORT DATE 1 May 1975
		13. NUMBER OF PAGES 121 pages
14. MONITORING AGENCY NAME & ADDRESS(if different from Controlling Office)		15. SECURITY CLASS. (of this report) Unclassified
		15a. DECLASSIFICATION/DOWNGRADING SCHEDULE

16. DISTRIBUTION STATEMENT (of this Report)

Document cleared for public release and sale; its distribution is unlimited.

17. DISTRIBUTION STATEMENT (of the abstract entered in Block 20, if different from Report)

18. SUPPLEMENTARY NOTES

19. KEY WORDS (Continue on reverse side if necessary and identify by block number)

Internal waves
Temperature profiles
Coherence measurements
Isotherm displacement
Spectra comparison

20. ABSTRACT (Continue on reverse side if necessary and identify by block number)

Profiles of temperature versus depth in the top 440 m of the sea were taken repeatedly at three horizontal locations surrounding the Research Platform FLIP. The time fluctuation of the temperature profiles was used to determine isotherm displacement and slope variation in the region 60-400 m.

Measurements were taken during three FLIP operations. Two were off the California coast, in November 1972 and June 1973.

over

20. ABSTRACT

Horizontal and vertical coherence measurements indicate that the internal wavefield can be divided into two frequency regions.

Above 2 cph the bandwidth of energetic horizontal and vertical wavenumbers is comparatively narrow. The isotherm displacement spectrum and slope spectrum have irregular slopes. A comparison of the two spectra indicate that first mode is strongly dominant.

Below 2 cph, the bandwidth of energetic wavenumbers is broader, corresponding to many energetic modes. The displacement spectrum has an Ω^{-2} frequency dependence down to about two cycles per day. The slope spectrum has an approximate $\Omega^{-1/2}$ spectral form in this region. This indicates that the bandwidth of energetic horizontal wavenumbers decreases with decreasing frequency, corresponding to a bandwidth of vertical wavenumber approximately constant with frequency. A vertical spectral analysis of the data substantiates this general picture, while revealing the presence of a low frequency high mode region of surprising spectral intensity. This "shoulder" region might be the spectral signature of horizontally advecting features in the temperature field which are not necessarily associated with vertical density perturbations. However, estimates of horizontal wavenumber indicate that these features, as well as those of longer wavelength, tend to satisfy the linear internal wave dispersion relation.

UNIVERSITY OF CALIFORNIA, SAN DIEGO
MARINE PHYSICAL LABORATORY OF THE
SCRIPPS INSTITUTION OF OCEANOGRAPHY
SAN DIEGO, CALIFORNIA 92132

OBSERVATIONS OF INTERNAL WAVES IN THE UPPER OCEAN

Robert Pinkel

Sponsored by
Advanced Research Projects Agency
through
Office of Naval Research
N00014-69-A-0200-6041
NR 260-104

SIO REFERENCE 75-10

1 May 1975

F.N. SPIESS, DIRECTOR
MARINE PHYSICAL LABORATORY

MPL-U-36/75

TABLE OF CONTENTS

OBSERVATIONS OF INTERNAL WAVES IN THE UPPER OCEAN

Robert Pinkel

University of California, San Diego
Marine Physical Laboratory of the
Scripps Institution of Oceanography
San Diego, California 92132

ABSTRACT

Profiles of temperature versus depth in the top 440 m of the sea were taken repeatedly at three horizontal locations surrounding the Research Platform FLIP. The time fluctuation of the temperature profiles was used to determine isotherm displacement and slope variation in the region 60-400 m.

Measurements were taken during three FLIP operations. Two were off the California coast, in November 1972 and June 1973. The third was north-northwest of Hawaii in November 1973.

Horizontal and vertical coherence measurements indicate that the internal wavefield can be divided into two frequency regions.

Above 2 cph the bandwidth of energetic horizontal and vertical wavenumbers is comparatively narrow. The isotherm displacement spectrum and slope spectrum have irregular slopes. A comparison of the two spectra indicate that first mode is strongly dominant.

Below 2 cph, the bandwidth of energetic wavenumbers is broader, corresponding to many energetic modes. The displacement spectrum has an Ω^{-2} frequency dependence down to about two cycles per day. The slope spectrum has an approximate $\Omega^{-1/2}$ spectral form in this region. This indicates that the bandwidth of energetic horizontal wavenumbers decreases with decreasing frequency, corresponding to a bandwidth of vertical wavenumber approximately constant with frequency. A vertical spectral analysis of the data substantiates this general picture, while revealing the presence of a low frequency high mode region of surprising spectral intensity. This "shoulder" region might be the spectral signature of horizontally advecting features in the temperature field which are not necessarily associated with vertical density perturbations. However, estimates of horizontal wavenumber indicate that these features, as well as those of longer wavelength, tend to satisfy the linear internal wave dispersion relation.

CHAPTER I

INTRODUCTION

The presence of internal wave-like motions in the deep sea has long been known. The role these motions play in the energy transfer and mixing of the ocean is still not clear.

The linear mathematical theory of internal wave propagation was first presented by Stokes in 1847 and has been thoroughly explored since then. Extensive theoretical studies of the interaction of internal waves with themselves and the ocean environment have been made. Additional understanding awaits meaningful oceanic measurements.

Observational efforts have yet to provide a clear picture of the internal wave field in the open sea. The wide range of spatial and temporal scales of internal waves make a single, all inclusive measurement effort impractical. The experiments that have been performed have generally been of two classes. Very high quality single instrument experiments have been conducted, either by towing an instrument to obtain a spatial data series, or letting it drift, to obtain a time series. These can give knowledge of the amount of motion present and its distribution with horizontal or temporal scale, but offer only indirect indication as to whether internal wave dynamics truly governs the motions. A comparison of the temporal and

three dimensional spatial variability of the motions is needed to establish the relevance of the linear internal wave dispersion relation. Large multidimensional array experiments have been performed. Records taken by different instruments in these arrays have generally shown surprisingly little resemblance, due either to the complexity of the wave field or to experimental difficulties.

The measurements to be discussed are from a moderate sized four dimensional (space-time) array, mounted on the Research Platform FLIP. The array was constructed as large as practicable while still being able to deploy very low noise sensors. With this four dimensional coverage it is possible to get a detailed view of the motions over a small area of the ocean around FLIP, with consequent poorer resolution of the larger scale motions. This thesis will discuss the results of the first series of operations of this experiment. The objectives of this preliminary study are to categorize the distribution of energy with space and time scales and to ascertain the applicability of linear internal wave theory to the motions observed in the upper ocean.

CHAPTER II

DESCRIPTION OF EXPERIMENT

Experimental Apparatus

This experiment utilizes temperature as a tracer to detect vertical displacements associated with internal waves. The basic data set consists of profiles of temperature versus depth in the upper 440 m of the sea, sampled repeatedly at three horizontal locations surrounding FLIP.

The primary sensor used was the F-M Thermometer developed by Mr. Earl Squier (1967). The probe consisted of three thermistor beads incorporated into the feedback loop of a phase shift oscillator circuit. The changing resistance of the beads resulted in a varying output frequency. These thermometer packages were characterized by their high sensitivity ($\sim$.003 °C r.m.s. typically) and minimal low frequency drift ($\sim$ .05 °C r.m.s. over several weeks of operation). The "rise time" of the thermometers was .25 sec.

Each of the 3 profiling units consisted of several components. An F-M thermometer and a vibratron pressure sensor were mounted on a streamlined, weighted, five feet long stainless steel probe. The probe was lowered into the sea by 3/16" double armored steel cable. One hundred and ninety meters up the cable, a second F-M thermometer was attached. The profiler was then lowered until the upper

thermometer was at the base of the mixed layer (typically 65 m). From this position, a remotely controlled five horsepower electric winch cycled the thermometers down and up through 190 meters at a rate of 4 m/sec. This yielded a temperature profile of the top 380 meters of the thermocline (Fig. 3). Profiles were repeated every two minutes. Measurements were taken while the probes descended. Preliminary analysis was done while they were being raised.

To produce the required horizontal separations, it was necessary to obtain lightweight booms which could be mounted on and deployed from FLIP. Two aluminum girder booms, seventy-five feet long, were constructed and installed on the port and aft faces of FLIP's superstructure. The starboard boom, sixty feet in length, was a converted aluminum spinnaker pole from the schooner GOODWILL. When deployed, a triangular array with separations 38, 39 and 44 meters was formed (Figs. 1, 2). The size of the array was limited by practical considerations associated with the handling of the booms at sea.

The azimuthal positioning of the array was affected strongly by the wind, which tended to orient FLIP such that the keel was 20° to the left of the wind direction. To maintain a constant heading for sufficient time to gather internal wave directional information, an automatic orientation control system was employed. This consisted of two hydraulically actuated off-axis propellers which were mounted on FLIP's hull and controlled by the ship's gyro-compass. Given the considerable windage of the array, the orientation system was overpowered by winds over $\sim$10 knots. However, with FLIP in the

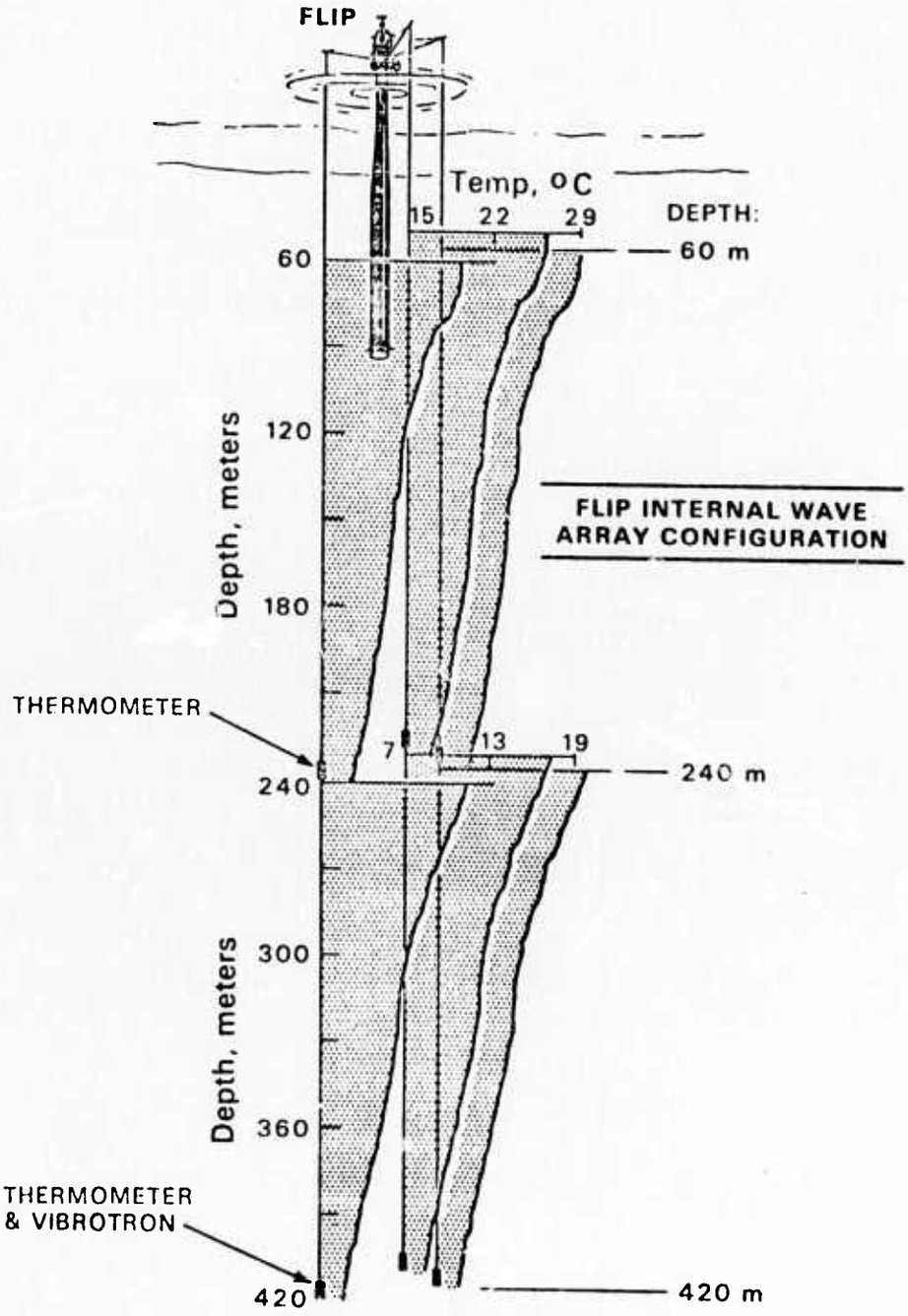

Figure 1. FLIP internal wave array configuration

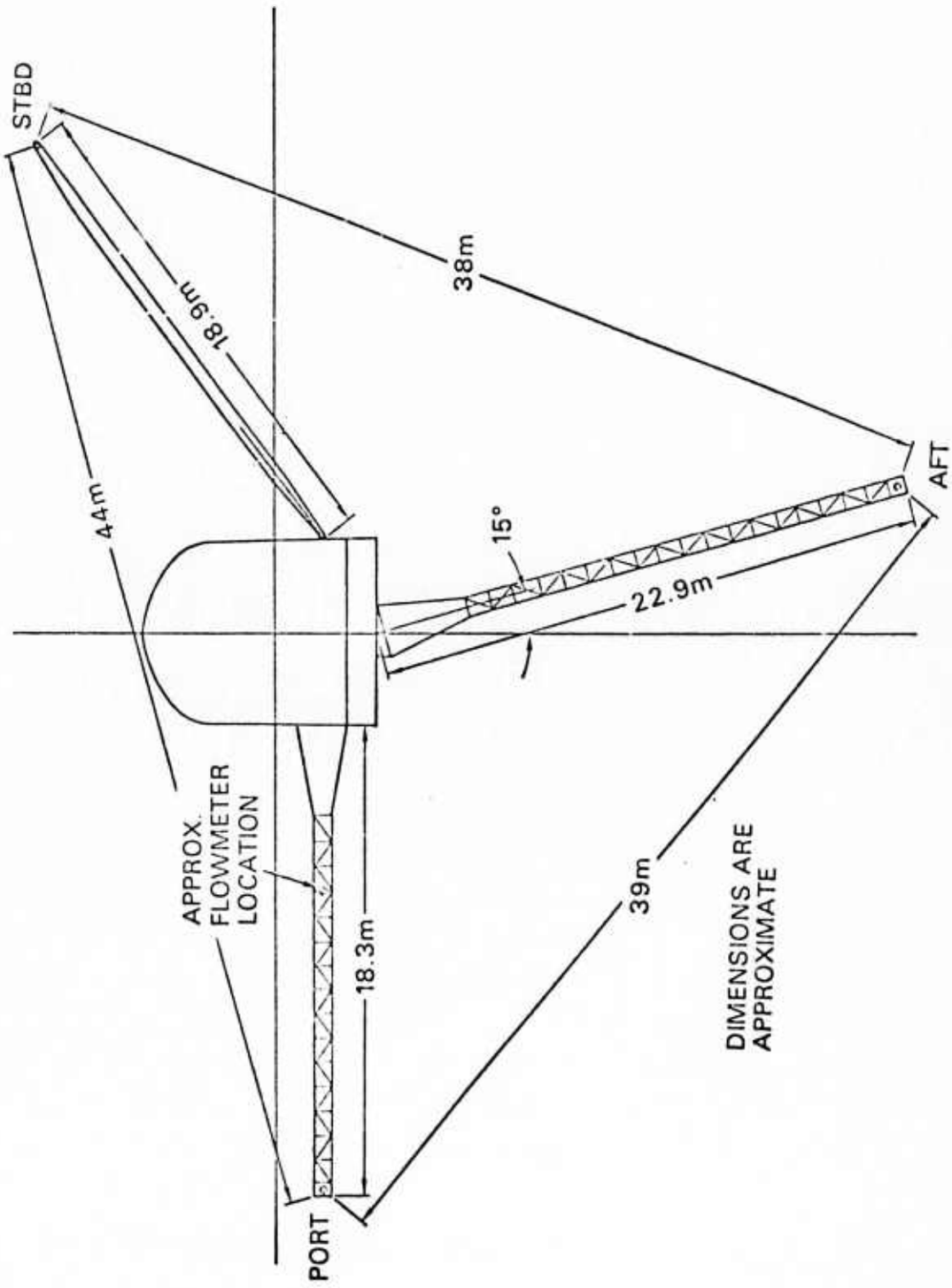

Figure 2. Top view of FLIP internal wave array

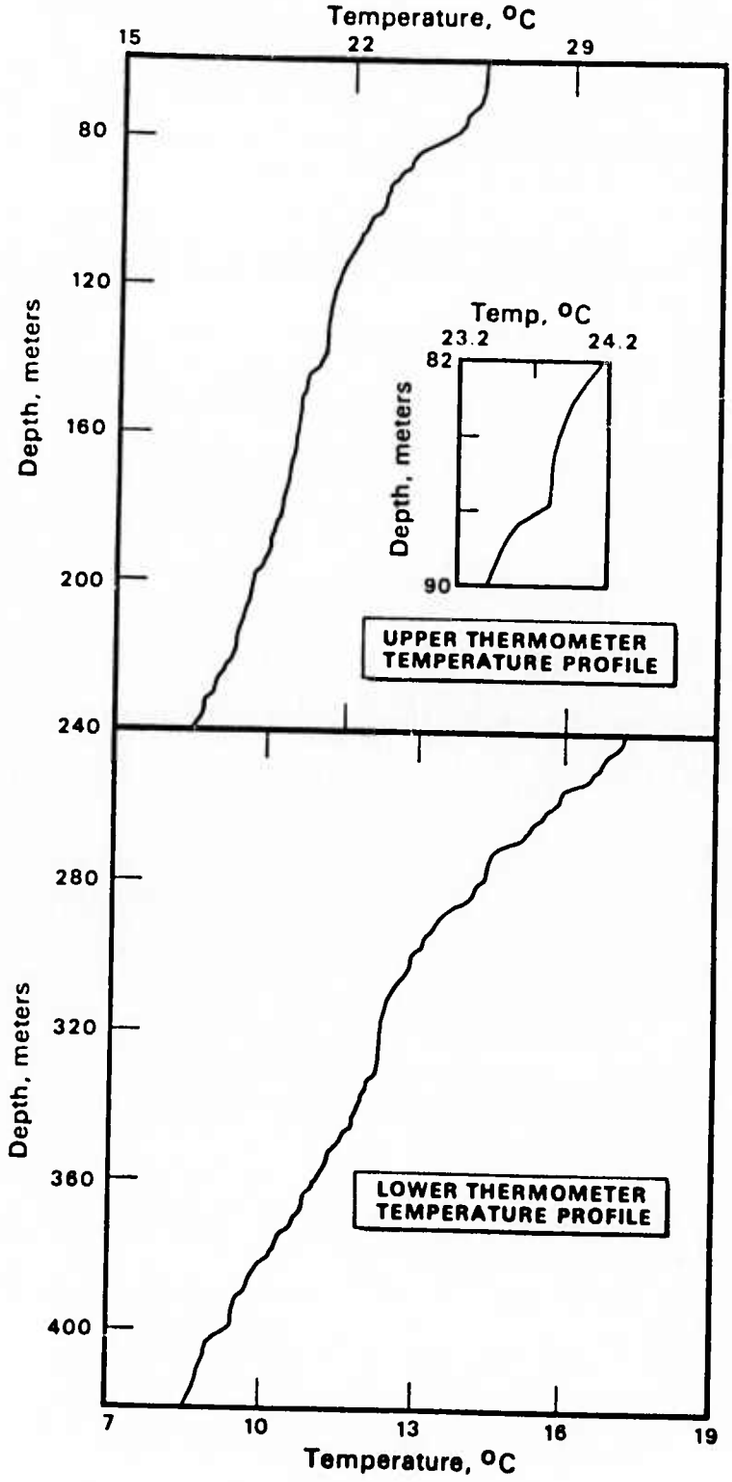

Figure 3. Typical temperature profile

equilibrium, into-the-wind position, the orientation system could reduce the azimuthal fluctuations to approximately ± 8°. Major wind shifts and squalls would necessitate the repositioning of the array.

In addition to the basic temperature data, supplemental information was recorded from a variety of sensors which were borrowed from others. An instrument package, incorporating a sound velocimeter, thermistor, vibratron, Doppler flow speed, and flow direction sensor was loaned by Mr. Earl Squier of the Marine Physical Laboratory of Scripps Institution of Oceanography for use during all of our operations. With this device, necessary vertical profiles of horizontal currents and density could be obtained. Wind speed, direction and atmospheric pressure were recorded during portions of June 1973 and November 1973 FLIP cruises using instruments of Dr. Carl Friehe (Department of AMES, University of California, San Diego). Surface wave measurements were conducted during the November 1972 and June 1973 trips with sensors supplied by Dr. Hal Guthart and Mr. Bob Martin of Stanford Research Institute.

Data handling functions were performed at sea by a Hewlett Packard 2116B computer system developed by Dr. Bruce Williams, Marine Physical Laboratory, Scripps Institution of Oceanography. Fifteen F-M and five analog data channels were scanned while the probes fell. Incoming information was stored in memory and written on nine track magnetic tape immediately after the probes completed their descent. All at-sea analysis and data display tasks were performed while the probes were rising, between drops. During this period the computer

performed a series of interpolations, picking out the set of depths at which a pre-selected set of temperatures had occurred in the profile of each of the thermometers. When temperature inversions were present, the shallowest depth at which the given temperature was encountered was arbitrarily chosen. These isotherm depths were then stored in memory and later written on tape along with the profile data from the next drop. Selected isotherm depths from each probe were also stored on the computer's disk for display and analysis purposes at sea. The disk held approximately 24 hours isotherm data. The isotherm interpolation required about ten seconds time during the probes' ascent; the roughly forty seconds time remaining was used for display of the isotherm information or raw data on the computer's cathode ray storage scope.

Data Collection

Measurements were made during three FLIP cruises. The first two were conducted off the California coast during November 1972 and June 1973. The starting location for both was 31°N, 121°W, a region of four km deep water, with flat bottom and scattered seamounts. This site is 120 km offshore (southwest) of the Patton Escarpment, a three km step-like break in the continental shelf. In this region, the southward flowing water of the California Current intermix with the northward, more intermittent flow of the Davidson Current.

The November 1972 operation lasted three weeks. It was interrupted briefly when FLIP drifted eastward toward the continental

shelf and had to be re-towed into deep water. On the June 1973 cruise FLIP was on station four weeks. The weather was quite varied on both cruises. Maximum winds were typically 25-35 knots. Periods of calm were frequent. Pronounced weather changes occurred on a four day - one week time scale.

It was not known how representative these California measurements were of the wave field in the central areas of the deep sea. The proximity of the continental shelf (5-15 internal tidal wavelengths distant) was one cause of concern. The shelf has been identified as a possible source (Rattray, et al., 1969; Wunsch and Hendry, 1972) and sink (Wunsch, 1968) of internal wave energy. The complex horizontal current structure of the region could also be expected to influence internal wave propagation. As a result, it was decided to make a short cruise north/northwest of Hawaii during early November 1973. Eleven days of data were taken starting at 25°N, 159°W in four km deep water. The sea floor was smooth with no seamounts in the immediate area. Conditions were quite moderate for the first week, and rough with 25 knot winds for the remaining four days. In all, approximately fifty days of usable data were collected. During that time at least one, and typically all three, profilers were in operation. Electrical problems with underwater connectors were the most common difficulty encountered. Severe squalls occasionally necessitated shutdown of the aft profiler. During these high winds FLIP's drift would become sufficient to cause the instruments to be swept into the hull. Squalls would also overpower FLIP's orientation

system, azimuthally spinning the ship and interrupting time series measurement of the directional properties of the wave field. Power generation difficulties aboard FLIP and at sea refueling were rare causes of complete cessation of the experiment.

Profiles of the Vaisala Frequency

Representative profiles of the Vaisala frequency

$$N(z) = \left(\frac{g}{\rho}\left(\frac{\partial \rho}{\partial z} - \frac{\rho g}{c^2}\right)\right)^{1/2}$$

for the cruises are presented in Figure 4. Typically, the November 1973 Hawaii cruise had the greatest Vaisala frequency; the June 1973 California cruise the smallest. These profiles are composites, resulting from many sound velocity-temperature-depth lowerings from FLIP. An STD system was also used in the June 1973 cruise. These profiles will be utilized to tune the analysis procedures to be described.

It was found that the Vaisala profile in the upper thermocline changes significantly on a time scale comparable to that of low frequency internal waves. An extreme example of the degree of modification in the upper thermocline which can occur is given in Figure 5. Thirteen hours of temperature profile data, taken on November 16, 1972 are presented. Successive profiles are separated by four minutes. The severe modification in the temperature structure above 120 meters

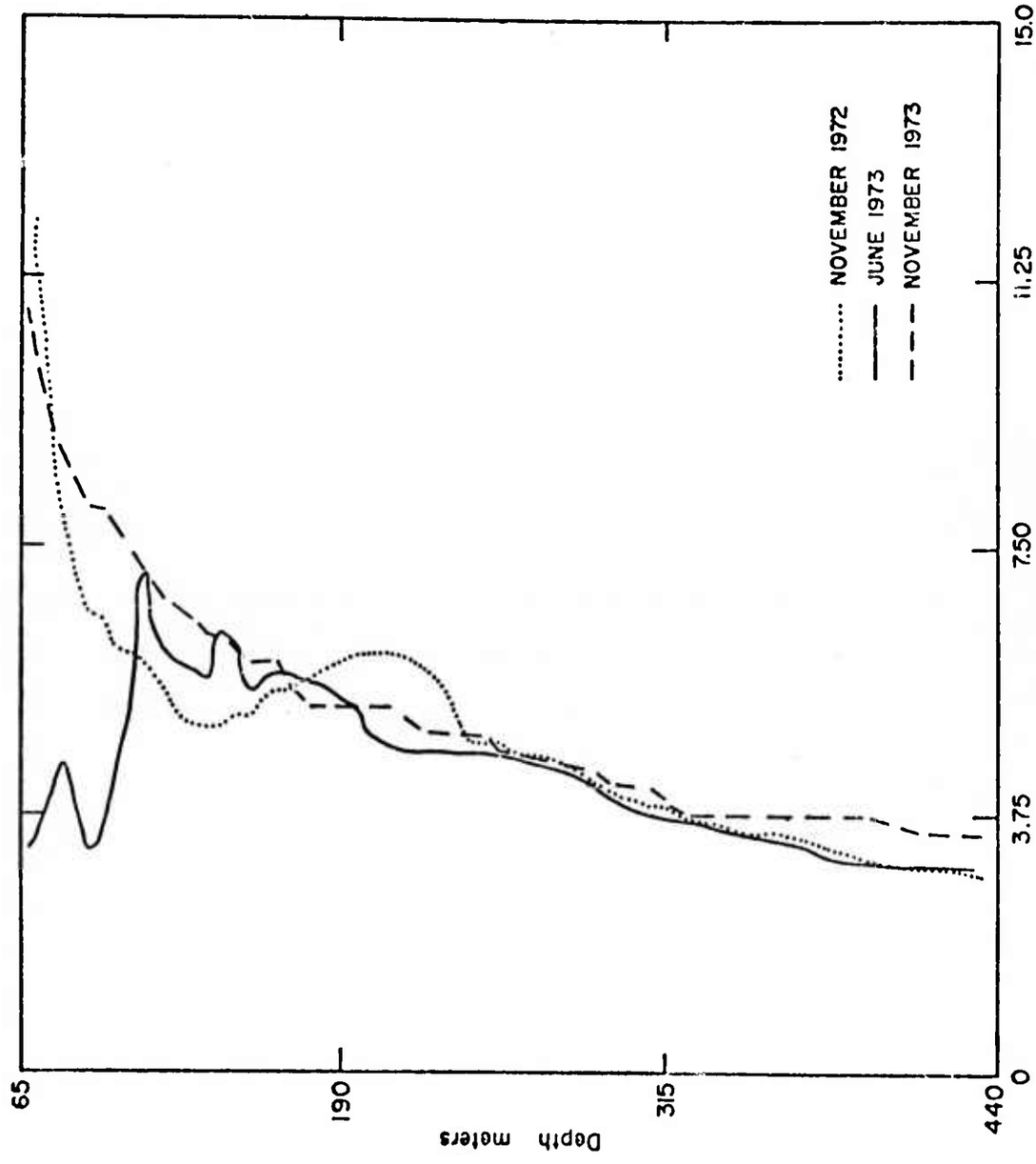

Figure 4. Representative profiles of Vaisala frequency

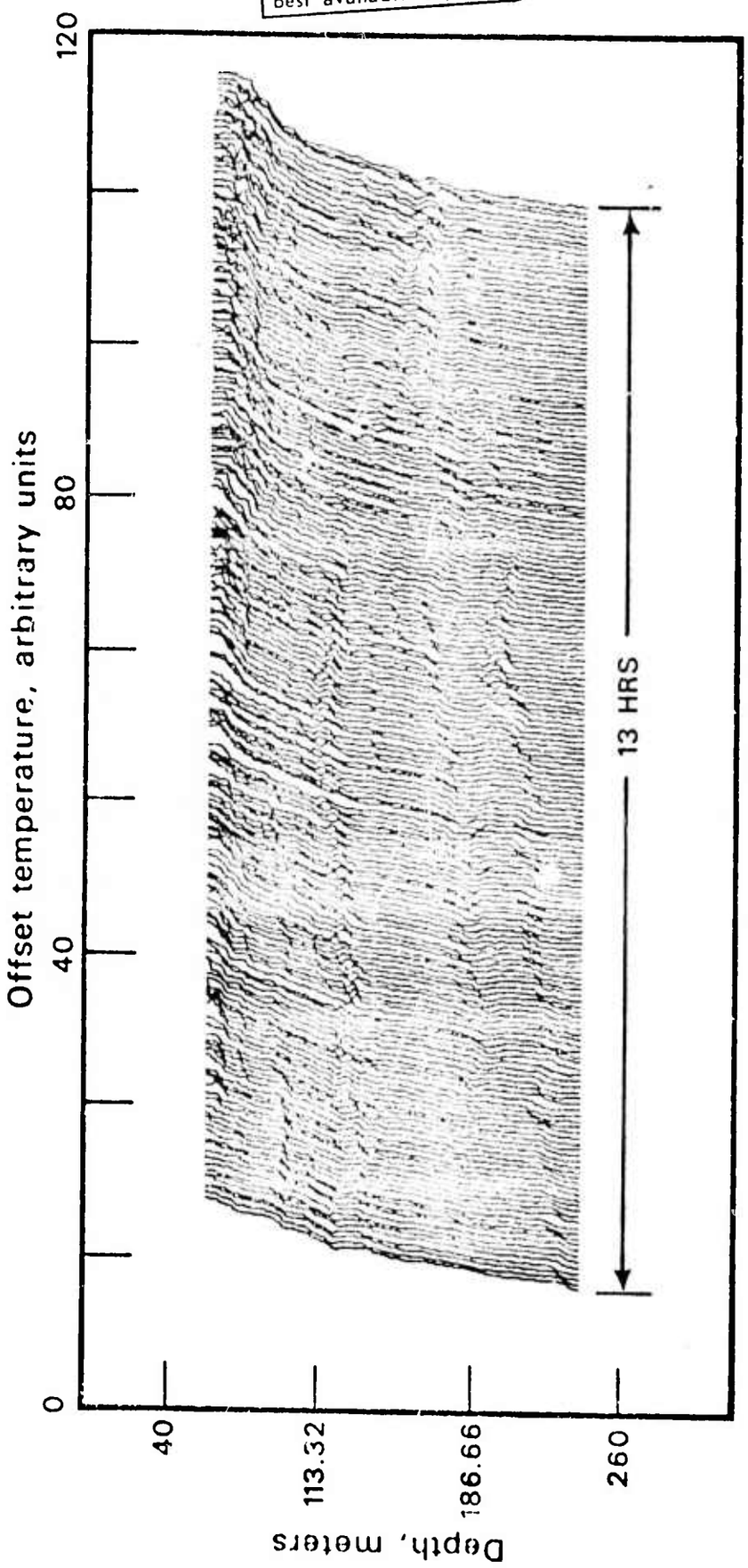

Figure 5. Thirteen hour sequence of temperature profile data FLIP starboard upper thermometer

over the thriteen hour series is striking. The many short lived inversions visible suggest that vertical mixing processes might be active in this region.

The migrating zones of locally high temperature gradient also stand out. It is doubtful that these features are a result of small vertical scale internal waves, straining an otherwise smooth temperature field. The profile is frequently completely deformed into a dynamically stable temperature inversion, which cannot possibly result from internal wave vertical displacements.

Mixing and advective effects are clearly modifying these profiles. It must be assumed that their influence on the density field will be significant also. Small scale details in the density profile presumably evolve more rapidly than the large scale features. As a consequence, a vertical length scale can be defined under which the density profile significantly changes over the time period necessary to obtain statistically stable measurements of the wave field. The analysis method to be utilized will fail to characterize motions of vertical scale less than this satisfactorily. It will be seen that noise in the analysis resulting from the time variation of the Vaisala profile and experimental error in its estimation will significantly contaminate the measurements of motions of less than 40 meter vertical wavelength.

Description of the Data

A thirteen hour segment of isotherm data from the starboard

profiler is presented in Figure 6. This sample is not representative of the bulk of the observations. However, it contains examples of most of the features found in the data. The isotherms followed by each thermometer are chosen at equal increments of temperature (~.1°C for the upper thermometer and ~.05°C for the lower). Close spacing of the isotherms indicates a high vertical temperature gradient. Gaps represent isothermal regions or temperature inversions. The large gap from 220 to 280 meters lies between the lowest isotherm followed by the upper thermometer and the highest isotherm followed by the lower.

The generally smooth nature of the time oscillations of the isotherms can be clearly seen. This implies a relative absence of energy in the motions at frequencies high compared to the Nyquist frequency of 15 cph. Exceptions are apparent where isotherms jump from top to bottom of nearly isothermal zones and visa versa. These jumps are due to slight temperature changes within the zones (perhaps associated with horizontal advection). They clearly do not represent vertical motions of the water and can be easily corrected, using vertical velocity information from the isotherms above and below the jump.

Considering now only the smoothly oscillating component of the data, two features are quite apparent. The higher frequency motions appear to be quite persistent with depth. Local crests present at eighty meters can frequently be seen, with the same phase, one hundred fifty meters below. In contrast, the lower frequency

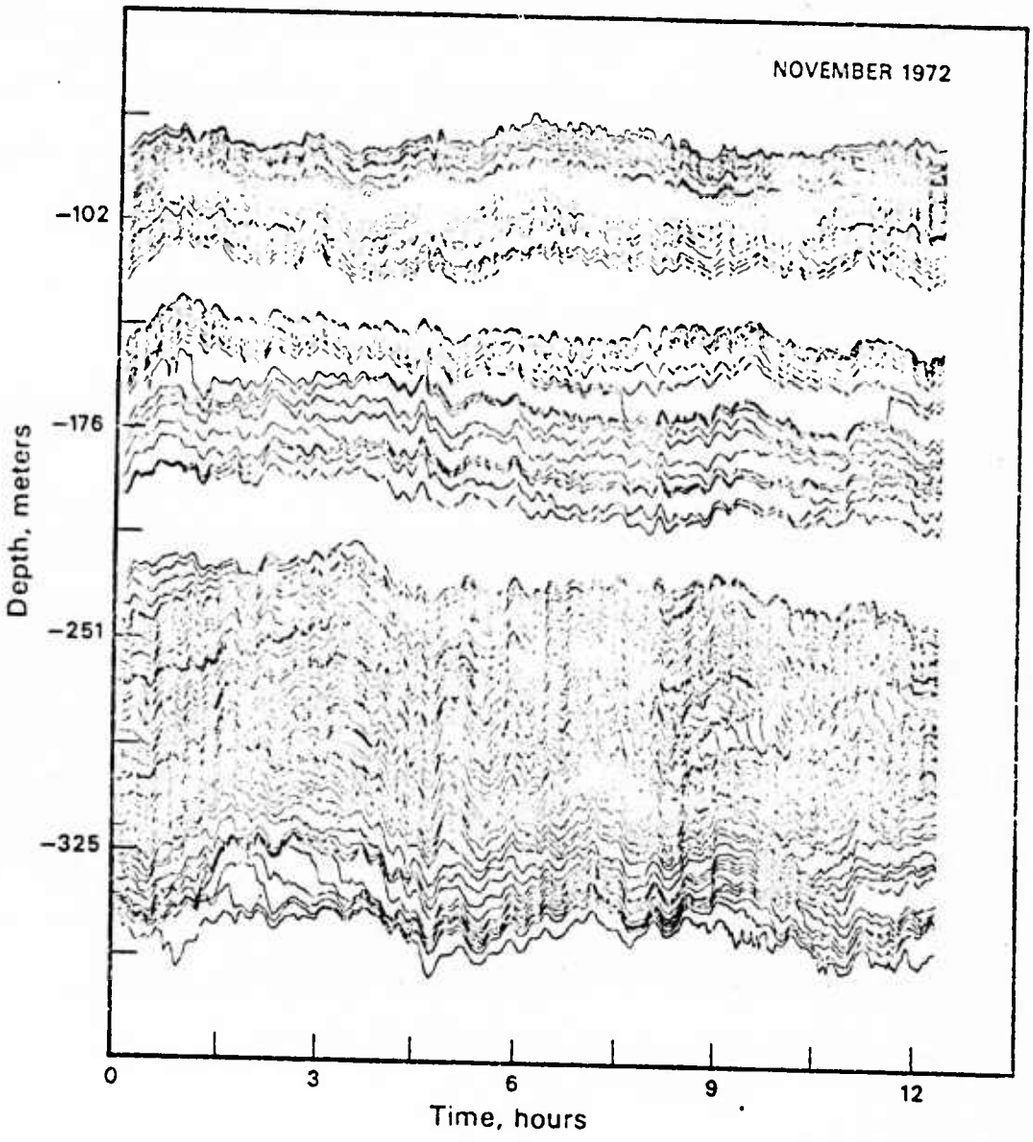

Figure 6. Thirteen hour series of isotherm fluctuation data FLIP starboard profiler

oscillations tend to exhibit greater variation with depth. Only at frequencies less than 3 cph are large phase changes in the vertical noticeable. In many records, the M2 internal tide can be seen to undergo a vertical phase reversal in less than 100 m. It is clear from this record that vertical wavelengths long compared to several hundred meters dominate the wave field at frequencies greater than 3 cph. At lower frequencies, shorter vertical wavelengths are associated with the observed vertical variations.

Fundamental Experimental Uncertainties

The isotherm fluctuations will be used to infer changes in the r.m.s. potential energy

$$E_p \equiv 1/2\ \rho\ N^2(z)\ \langle \eta^2 \rangle$$

ρ = density gm/cm^3

$N(z)$ = Vaisala frequency

η = displacement of an isopycnal surface above its mean position

and the r.m.s. vertical kinetic energy

$$E_k = 1/2\ \rho \langle w^2 \rangle$$

w = vertical velocity

in the upper thermocline. Since temperature rather than density is measured, error is introduced into the potential energy determination whenever temperature becomes a poor tracer of density. Mixing,

diffusion, and lateral advection are the principal sources of this error. Uncertainty in the vertical kinetic energy estimation is introduced by the fictitious vertical velocity

$$\varepsilon(z,t) = - \overline{u(z,t)} \cdot \nabla_H T / \frac{\partial T}{\partial z}$$

which results from the horizontal advection of the water through the array. This effect would be present even if density and not temperature were measured. It is traditionally discussed in terms of the Doppler shifting of measured frequencies.

Neither error can be a priori distinguished from vertical internal wave velocities using temperature data alone. Yet the role they play is not mysterious. Their effect on the interpretation of the measurements is discussed below.

The potential energy error results from temperature being a poor tracer of vertical motions. Figure 6 reveals several examples suggestive of mixing or horizontal intrusive events causing vertical fluctuation of the isotherms. Consider the motions occurring at depth 325 m; time 8-12 hours. Isotherm after isotherm is seen to migrate from top to bottom of a region of low temperature gradient, possibly associated with the advance of a warm lens of water into the FLIP sampling area. Note that all motions of this sort in Figure 6 are typically confined to an isolated 10-25 m depth zone. The event dominates the signal at one depth but has little apparent effect on the isotherm motions 30 or 40 meters away. Thus, given the 350-400

meter vertical picture from the array, it is seldom difficult to separate out the longer vertical scale wave motions from the local intrusive mixing effects. However, there is no way to separate the shorter (~20 m) vertical scale wave motions from the more gradual, less "obvious" intrusions without direct density measurements. As a result, a detailed study of the short vertical scale fluctuations will not be attempted.

Error in the vertical kinetic energy estimates is associated with the Doppler shifting of measured frequencies. If ω is the true, intrinsic frequency of a wave, and Ω the observed Doppler shifted frequency, the relative frequency error $\delta\omega$ is given by

$$\delta\omega \equiv \frac{\Omega-\omega}{\omega} = -\frac{\bar{C}_p \cdot \bar{u}(z)}{|C_p|^2}$$

where $\bar{C}_p$ is the horizontal phase velocity of the wave. As internal wave horizontal phase velocities are not large compared to typical relative advective velocities ($u(z) \approx 10$ cm/sec) significant Doppler shifting might be expected.

In principle, with the four dimensional data set provided by this experiment and the assumption of an internal wave dispersion relationship, the intrinsic frequency could be obtained from measurements of the horizontal and vertical spatial frequencies. Success in this approach is curtailed both by the limited resolution of the array and the inapplicability of the theoretical linear dispersion relation, as a result, primarily of the pronounced current shear in the upper

thermocline. The data will thus be analyzed and displayed in terms of the encounter frequency Ω. Measurements taken during periods of excessively high relative FLIP drift will be discarded. Where significant wave energy is found associated with slower phase velocities it must be born in mind that it has possibly been severely Doppler shifted.

CHAPTER III

THE STATISTICAL DESCRIPTION OF THE MOTION

The isotherm motions measured can be mathematically modeled by

$$\eta(\bar{x},z,t) = \int_{\kappa=0}^{\infty} \int_{\theta=0}^{2\pi} \int_{\omega=0}^{\infty} dA(\kappa,\theta,\omega)W(\kappa,\omega,z)e^{i\bar{\kappa}\cdot\bar{x}-\omega t}$$

where W is a solution to the linear, shear free internal wave equation

$$\frac{\partial^2 W}{\partial z^2} + \kappa^2 \frac{N^2(z)-\omega^2}{(\omega^2-f^2)} W = 0$$

$$W = 0 \quad \text{at} \quad z = 0$$

and is normalized such that

$$\frac{1}{2D} \int_{D} \rho(z)\, N^2(z)\, W^2(\kappa,\omega,z)dz = 1 .$$

This representation is similar to the equivalent continuum approach of Garrett and Munk (1972) and is discussed in greater detail

in Appendix I.

The r.m.s. potential energy is given by

$$\hat{E}_p = 1/2\ \rho(z)N^2(z)\ \langle \eta^2 \rangle$$

$$= 1/2\ \rho(z)N^2(z) \int_{\kappa=0}^{\infty} \int_{\theta=0}^{2\pi} \int_{\omega=0}^{\infty} \langle dAdA^*(\kappa,\theta,\omega) \rangle\ W^2(\kappa,\omega,z)$$

$$= 1/2\ \rho(z)N^2(z) \int_{\kappa=0}^{\infty} \int_{\theta=0}^{2\pi} \int_{\omega=0}^{\infty} \hat{dE}(\kappa,\theta,\omega)\ W^2(\kappa,\omega,z)$$

where

$$\hat{dE}(\kappa,\theta,\omega) \equiv \langle dAdA^*(\kappa,\theta,\omega) \rangle$$

is the potential energy spectrum. The objective of this section is the estimation of the spectrum.

The spectrum can be related to the data set through the covariance function

$$\hat{C}(\bar{x}_1-\bar{x}_2,z_1,z_2,t_1-t_2) = \langle \eta(x_1,z_1,t_1)\eta(x_2,z_2,t_2) \rangle$$

or more conveniently, its time Fourier transform, the cross spectrum

$$\hat{CR}(\bar{x}_1-\bar{x}_2,z_1,z_2,\omega) = F(\hat{C}(\bar{x}_1-\bar{x}_2,z_1,z_2,\Delta t_{12});\Delta t_{12})$$

$$= \langle F(\eta(\bar{x}_1,z_1,t_1);t_1)\ F^*(\eta(x_2,z_2,t_2);t_2)\rangle$$

where $F(a;y)$ represents the Fourier transform of a with respect to y. Ideally, the spectrum can then be obtained through Fourier transform of the horizontal dependence of the cross spectrum

$$W(\kappa,\omega,z_1)\ W(\kappa,\omega,z_2)\ d\hat{E}(\kappa,\omega,\theta) = F(\hat{CR}(\Delta\bar{x},z_1,z_2,\omega);\ \bar{x})\ .$$

Alternatively, a wavenumber magnitude-frequency spectrum results from vertical integral transformation of the cross spectrum, utilizing the internal wave vertical wavefunctions introduced above.

$$d\hat{E}(\kappa,\omega) = \int_0^{2\pi} d\hat{E}(\kappa,\theta,\omega) = \int_0^{-H} dz_1\ \left(\frac{N^2(z_1)-\omega^2}{\omega^2 - f^2}\right.$$

$$W(\kappa,\omega,z_1) \int_0^{-H} dz_2\left(\frac{N^2(z_2)-\omega^2}{\omega^2-f^2}\right) W(\kappa,\omega,z_2)\ \hat{CR}(o,z_1,z_2,\omega)\ .$$

The equivalence of these two approaches depends on the assumption that linear, snear free internal wave dynamics well relates the horizontal, vertical and temporal scales of the observed motions. Given the typical magnitude of horizontal shears in the thermocline, the validity of this assumption is doubtful. An effort will be made

to compare these approaches at the end of this chapter.

This experiment does not provide sufficient information to perform either of the above integral transform direct spectral estimation methods. Nevertheless, a sample cross spectrum $CR(\bar{x}_i - \bar{x}_j, z_i, z_j, \Omega)$ can be evaluated from the data obtained, and less direct methods used to infer the form of $d\hat{E}(\kappa,\theta,\omega)$. The various spectral estimators to be used in this study will all be related to $CR(\bar{x}_i - \bar{x}_j, z_i, z_j, \Omega)$.

To calculate the sample cross spectral estimate, the measured region of the water column was divided into forty fixed depth intervals. For every drop, the mean internal wave vertical displacement was calculated in each of the depth intervals at each of the three profilers. Forty x 3 time series of mean isotherm displacement were thus produced. These fixed depth series were divided into 17.07 hour (512 drop) records, first differenced, multiplied by a triangular data window, and fast Fourier transformed. The resulting spectral window, $\text{sinc}^4(2\Delta f)$, had elemental bandwidth 2/17 cph. Twenty-three overlapping 17 hour series were analyzed from the November 1972 cruise, thirty for the June 1973 cruise and seventeen from the November 1973 operation.

In the sections that follow, the sample spectral estimators will be presented and their relation to the spectral density function $dE(\kappa,\theta,\omega)$ discussed. First the frequency dependence will be examined, then the frequency and depth dependence; then frequency and horizontal dependence. Finally, the four dimensional behavior of the spectrum will be investigated.

The Vertical Displacement Frequency Spectrum

The vertical displacement frequency spectrum

$$S(z,\Omega) \equiv CR(o,z,z,\Omega) \qquad m^2/cph$$

is related to the spectral density function by

$$S(z,\Omega) = \int_{\kappa=0}^{\infty} \int_{\theta=0}^{2\pi} dE(\kappa,\theta,\omega)\, W^2(\kappa,\Omega,z).$$

For a given frequency and depth, the value of the displacement spectrum is given by the $\overline{\kappa}$ - integrated sum of all energy at that frequency, modulated by the square of the vertical wavefunctions $W^2(\kappa,\Omega,z)$ evaluated at the given depth. For frequencies far above the inertial frequency, $S(z,\Omega)$ is directly proportional to the potential energy spectrum (energy/vol/cph) with proportionality constant $1/2\ \rho(z)N^2(z)$. The spectra to be presented below are thus an indicator of the distribution of internal wave potential energy with frequency.

A displacement spectrum of the 20° isotherm taken from 10 days of the Hawaii data, is presented in Figure 7. Below 2 cph the spectrum can be approximately characterized by an Ω^{-2} slope. Between 2 cph and the local Vaisala frequency there is frequently some irregularity in the slope; in this case a peak is present. At the Vaisala frequency, the spectrum cuts off sharply, falling 15 to 25 dB in

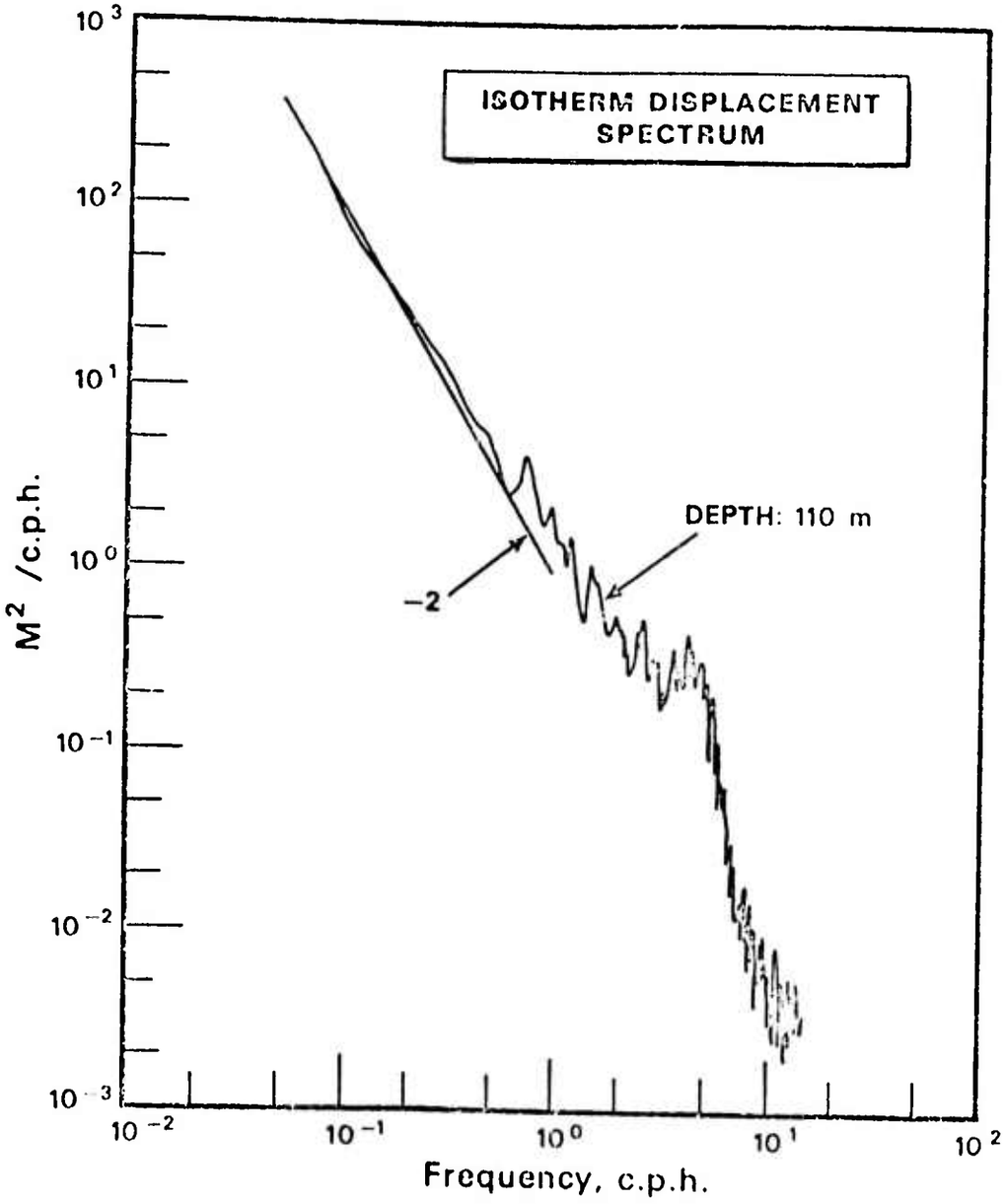

Figure 7. Hawaii isotherm displacement spectrum, 40 degrees of freedom

energy down to a spectral region dominated by thermometer noise. The slope of the spectral cutoff is typically ω^{-10} (however the spectral processing techniques used were not intended to produce an optimal spectral estimate in the region of the cutoff. The ω^{-10} slope must be considered an imprecise estimate). The high frequency noise level, if assumed to be white noise, corresponds to an r.m.s. uncertainty in the depth of an isotherm of ~30 cm. Lower noise measurements taken in June off California indicate a r.m.s. precision of ~15 cm, which approaches the point where the concept of a smoothly varying isothermal surface is no longer viable in the upper ocean.

The absence of a pronounced spectral cutoff in many previous internal wave experiments utilizing fixed depth instruments has been attributed by Phillips (1971) and Garrett and Munk (1971) to spectral contamination effects associated with nonlinearities in the vertical gradients of the properties measured. Assuming a step-like vertical gradient, an ω^{-2} contamination spectral form was indicated by their studies. The level of contamination could be sufficient to dominate the signal in the internal wave band, in addition to obscuring the cutoff.

To verify their suggestion, a sub-experiment was conducted during a July 1971 cruise off the California coast. A temperature sensor was lowered to a fixed depth (80 m) while a profiler was in operation 10 meters away. Eight hours of data were taken to provide a 16 degree of freedom look at the high frequency end of the spectrum. The displacement spectrum of the isotherm, Figure 8, shows a

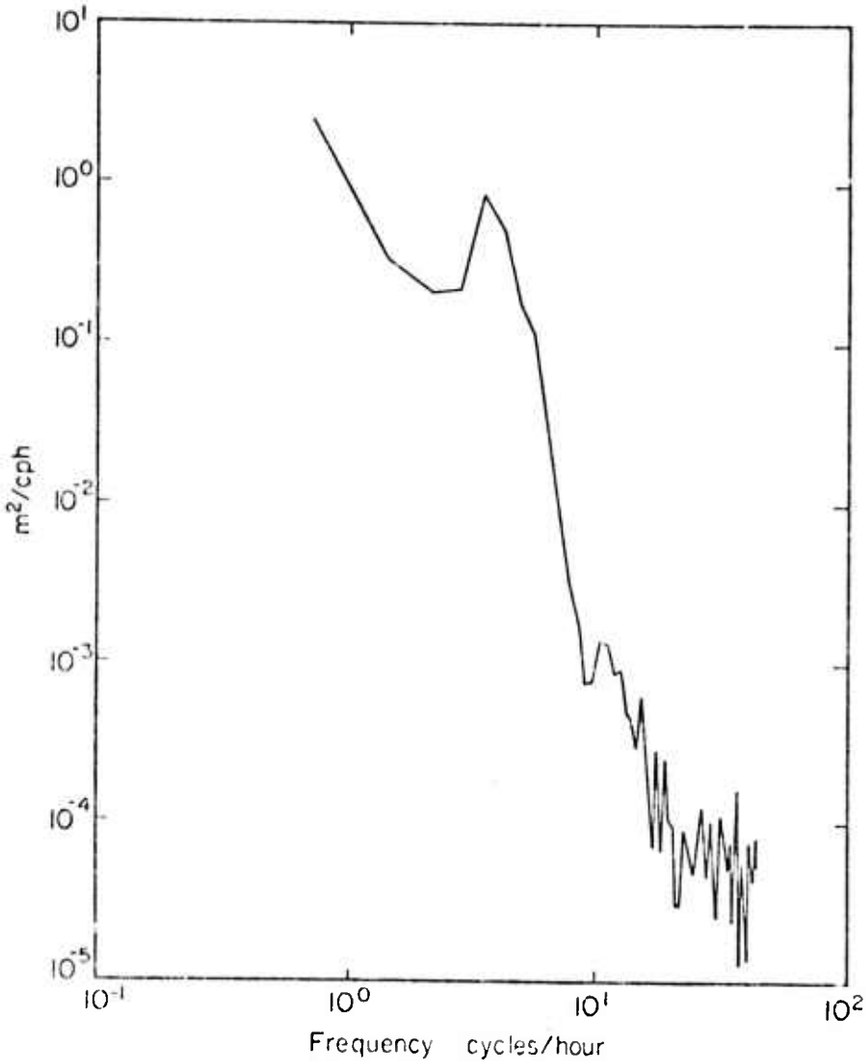

Figure 8. California isotherm displacement spectrum. July 1971, 5.6 hour record, ~45 cph Nyquist frequency, 16df.

pronounced peak prior to a severe ~40 dB Vaisala cutoff. The spectrum of temperature fluctuations, Figure 9, displays a noticeable ~10 dB Vaisala cutoff, followed, at higher frequency, by the predicted Ω^{-2} contamination spectrum. The "fine structure contamination" did not dominate the signal in the internal wave frequency band during this observation. Recently Briscoe (personal communication) has obtained fixed depth temperature spectra from a TRI-mooring in the Atlantic Ocean which also appear to be relatively uncontaminated by nonlinearities in the temperature gradient and are reminiscent of the isotherm displacement spectrum presented above.

The spectral peak prior to the Vaisala cutoff has been a source of great puzzlement. An explanation has been suggested by Desaubies (pers. comm.) and Garrett and Munk (pers. comm.) which can be loosely paraphrased as follows: Assuming a Vaisala profile monotonically decreasing with depth, for a given frequency, ω, one can define a cutoff depth, $D(\omega)$ such that $N(D(\omega)) = \omega$. Below this depth, wave functions $W(\kappa,\omega,z)$ decay exponentially for all κ. Slightly shallower than this "turning depth", depending on κ, all wave functions will have a relative maxima, exhibiting a behavior similar to the Airy function. At depths further into the wave guide, the phases of the vertical functions will tend to de-correlate, due to the differing vertical "wavelengths" associated with differing κ. Recalling the definition of the displacement spectrum

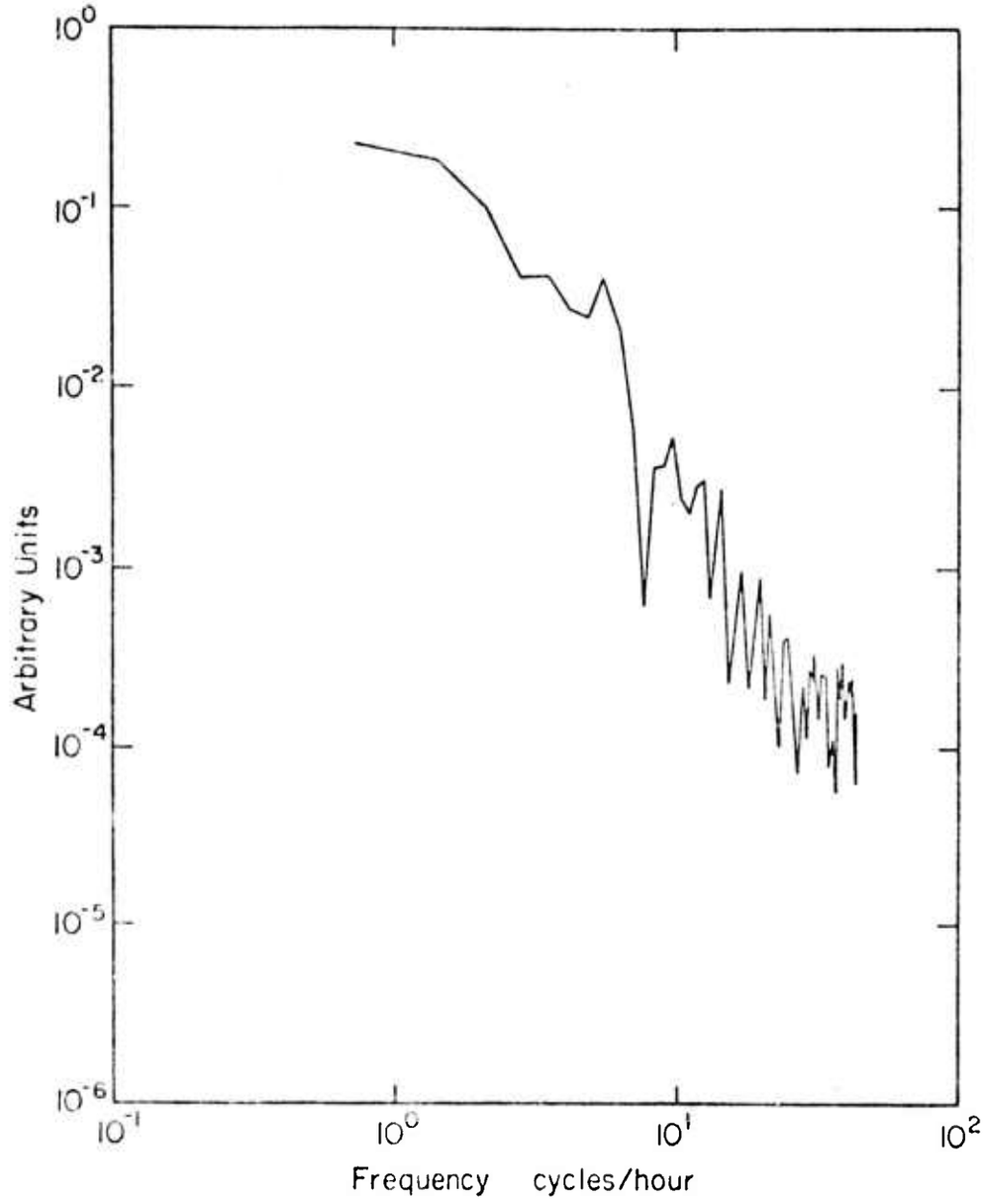

Figure 9. California fixed depth temperature spectrum July 1971, 5.6 hour record, ~45 cph Nyquist frequency, 16 df.

$$S(z,\Omega) = \int_0^{\infty} \int_0^{2\pi} \langle dAdA^*(\kappa,\theta,\omega)\rangle \, W^2(\kappa,\Omega,z)$$

$\kappa \quad \theta$

we see that the κ integration will tend to weight some regions of wavenumber-frequency space more than others, depending on whether the corresponding $W^2(\kappa,\Omega,z)$ is near a node or a maximum. However, at depths just above $D(\omega)$, all wave functions should be near a relative maximum. The resulting constructive interference would produce a peak in the displacement spectrum. Correspondingly, at a given depth, the spectral peak should occur at frequencies slightly below the Vaisala cutoff.

This simplified discussion rests heavily on the assumption that $\langle dAdA^*(\kappa,\theta,\Omega)\rangle$ varies smoothly with ω and κ. Otherwise, it would be impossible to distinguish between the effects of the above mentioned interference phenomena and the Ω,κ variation of $\langle dAdA^*(\kappa,\theta,\Omega)\rangle$ itself.

Figure 10 displays the same displacement spectrum as Figure 7, plotted together with the spectrum of the 15° isotherm (mean depth 380 m). As the data were taken at the same time, spectral differences presumably result from the depth variability of the square of the vertical wavefunction, $W^2(\kappa,\Omega,z)$. Several differences are clearly apparent . The spectrum of the colder isotherm tends to have greater variance than that of the warmer at frequencies below the Vaisala cutoff. The cutoff occurs at a lower frequency, indicative of the decrease in the Vaisala frequency with depth. Also, the pronounced

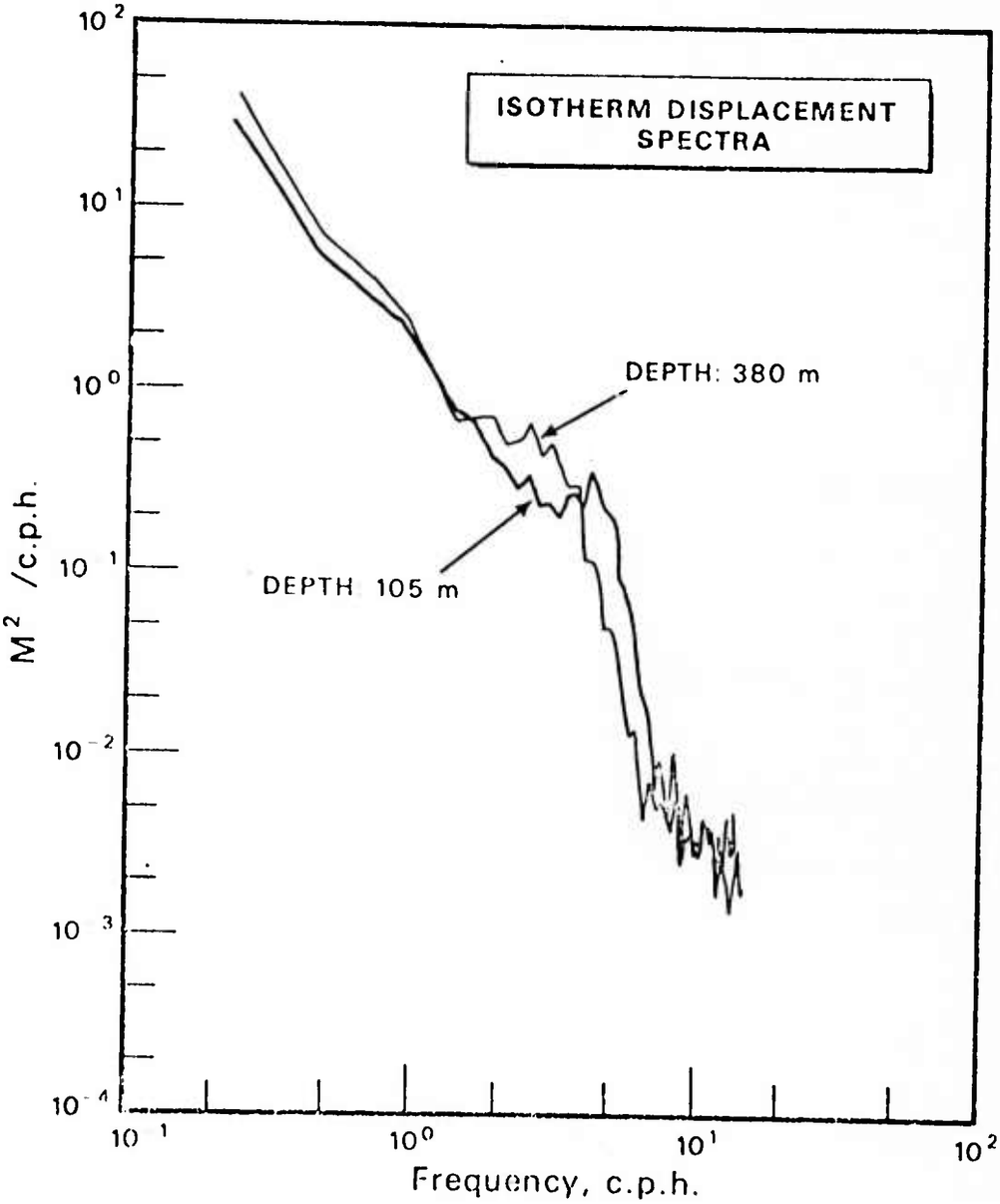

Figure 10. Hawaii isotherm displacement spectra 105 m - 380 m, 72 df

spectral peak observed at 90 m is not present at 380 m.

To extend this comparison, six Hawaii displacement spectra (72 degrees of freedom) are plotted in Figure 11. The uppermost spectrum is plotted with the correct scale, the others are successively shifted by 10 dB to prevent the plots from overlapping. The depth variations in spectral slope, cutoff slope and high frequency peak are here clearly apparent. Presented in the same format are displacement spectra from the November 1972 California (Fig. 12) and June 1973 California (Fig. 13) cruises. The November 1972 spectra, estimated at 64 degrees of freedom are the least energetic, and tend to have the weakest cutoffs. The pre-cutoff multiple spectral peaks which appear to be statistically significant in the upper spectra "fade away" by the lower spectrum.

The more energetic June California data (48 df) show no clearly defined pre-cutoff peaks; rather a broad rise is present (upper spectra) or nothing at all (lowermost spectrum). The cutoff slopes are quite pronounced, and the high frequency noise levels are the lowest of any of the three curises.

Figures 14 and 15 are overlays of the preceeding plots, which permit direct comparison of the late fall/late spring California spectra and late fall California and Hawaii spectra. Note that in the region of the water column measured, the November Hawaii wave field has approximately 1.5 times the potential energy of the November California wave field.

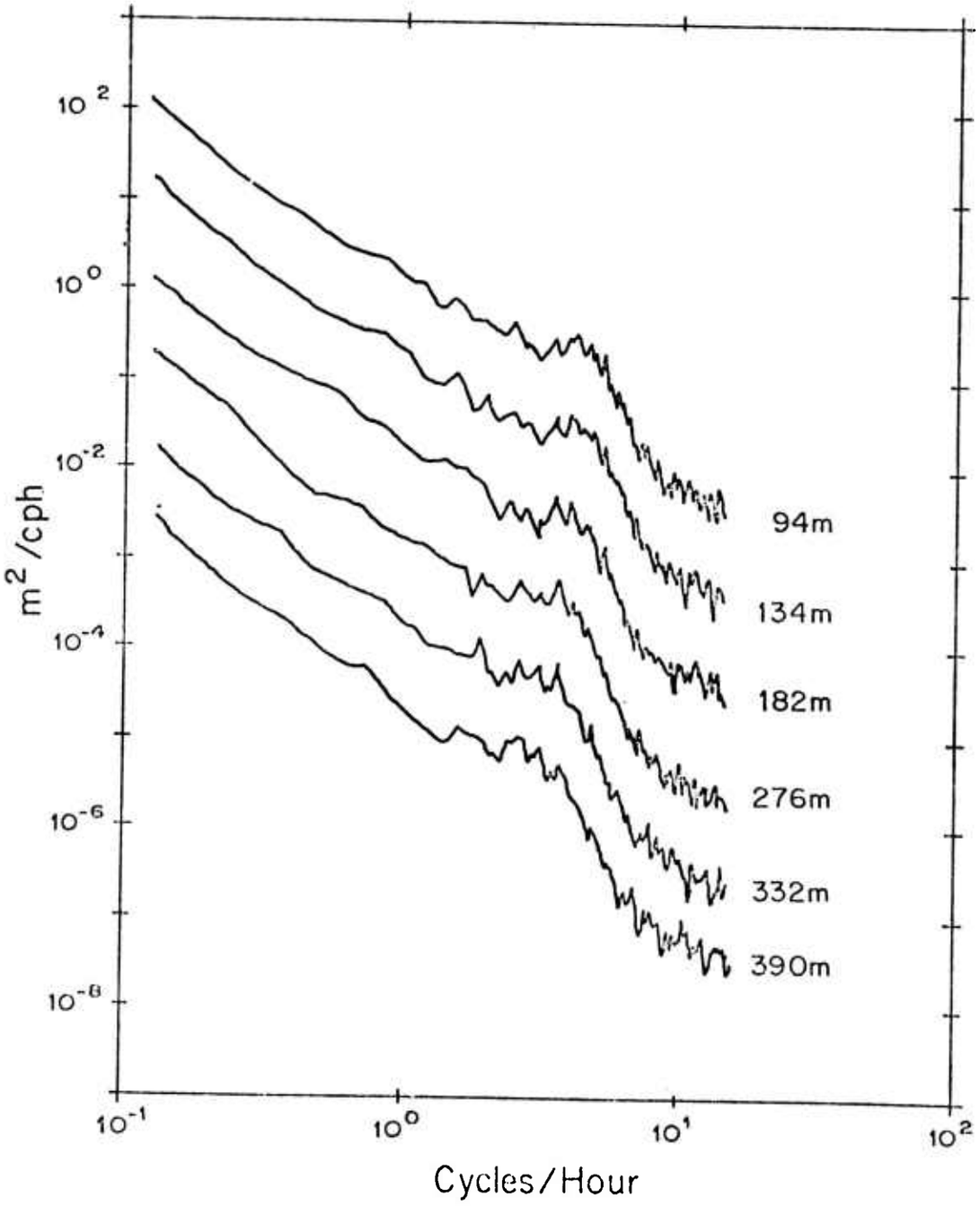

Figure 11. Hawaii isotherm displacement spectra 72 df. Spectra are offset by successive 10 db increments from uppermost spectrum.

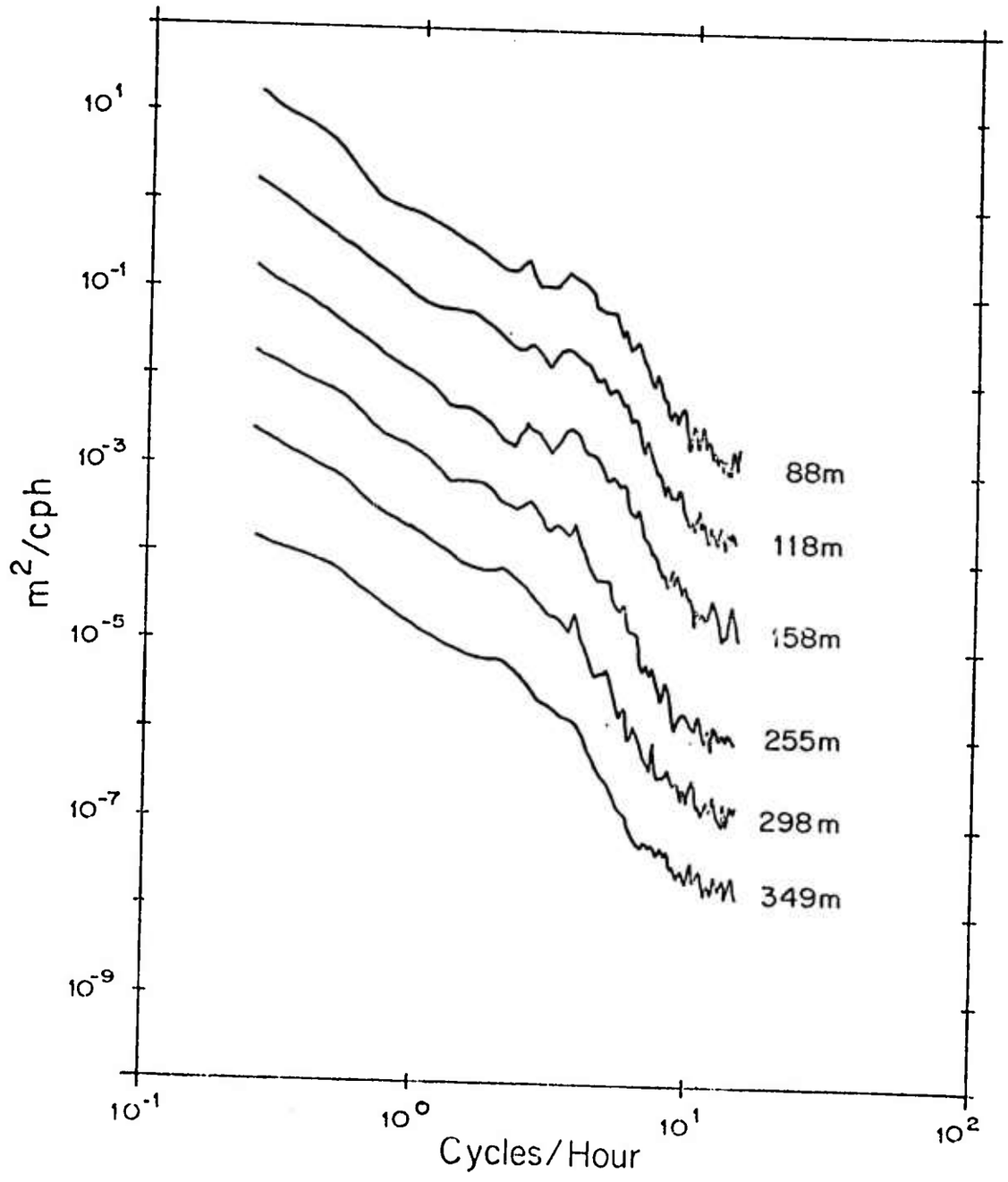

Figure 12. California November 1972: Isotherm displacement spectra 64 df.

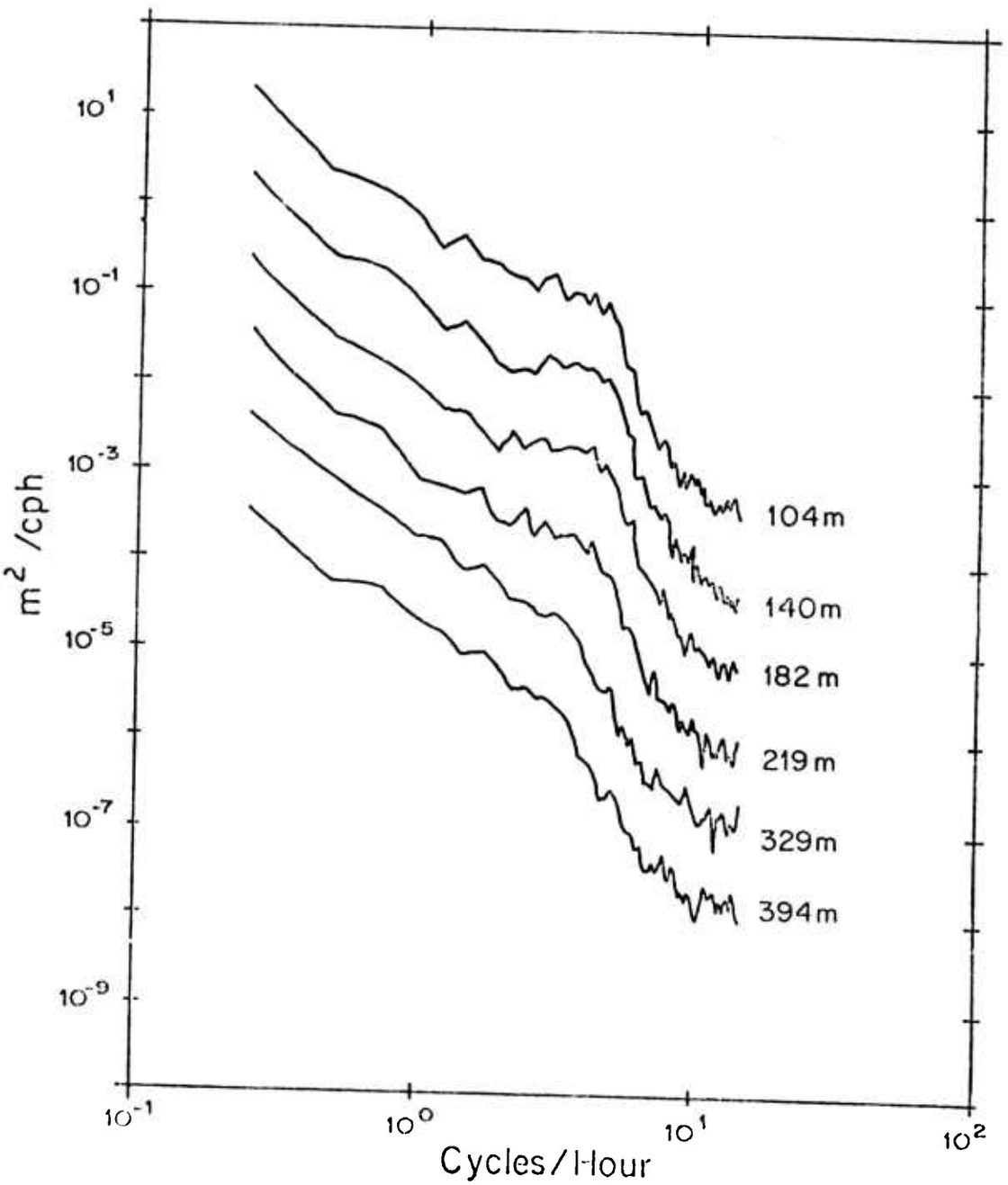

Figure 13. California June 1973: Isotherm displacement spectra 48 df.

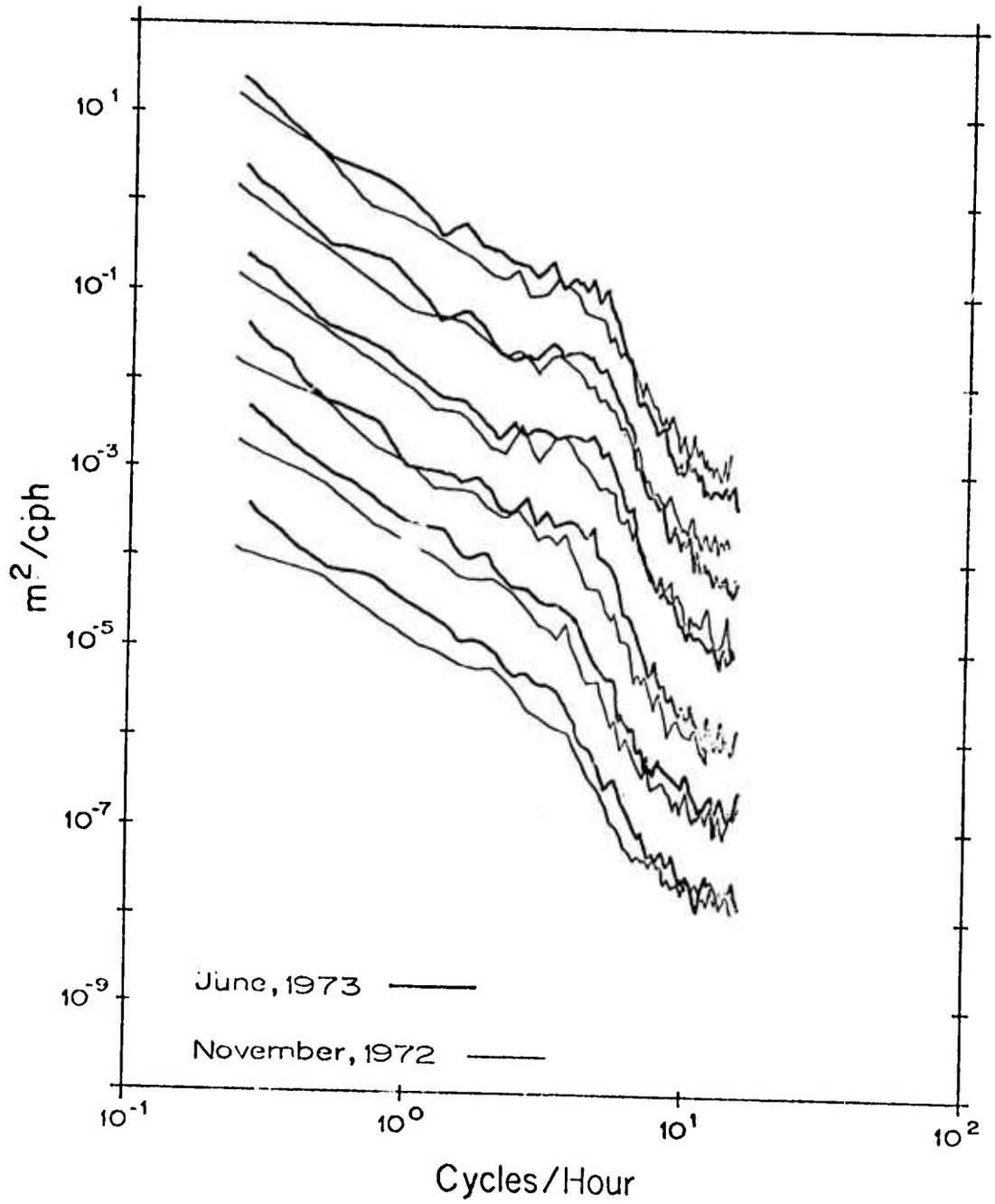

Figure 14. Fall - Spring California spectral comparison.

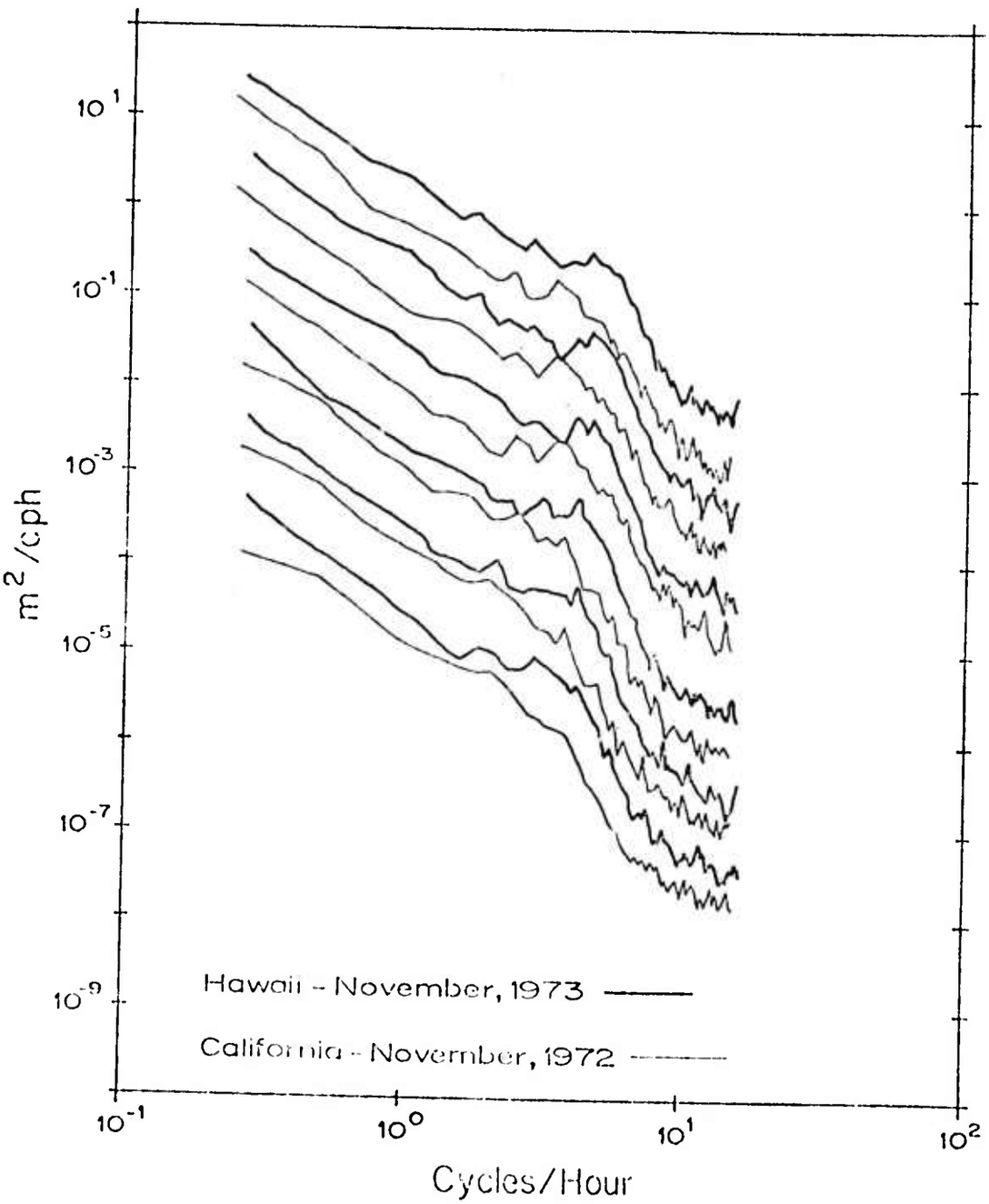

Figure 15. California - Hawaii spectral comparison.

The Vertical Velocity Spectrum

The spectrum of isotherm vertical velocity is related to the isotherm displacement spectrum by the factor Ω^2

$$V(z,\Omega) \equiv \langle \left| \frac{\partial \eta}{\partial t} (\bar{x},z,\Omega) \right|^2 \rangle = \Omega^2 \, S(z,\Omega) .$$

Spectra of vertical velocity for the three cruises are presented in Figures 16-18. Table I lists the associated variances. The pre-cutoff spectral rise in the displacement spectrum is transformed, by the Ω^2 weighting, into a distinct peak in the vertical velocity spectrum. Frequently half of the total vertical velocity variance measured is located in this 2-3 cph wide pre-cutoff peak.

At greater depths this velocity spectral peak might well be more localized in frequency. It will be suggested that more modes are present at lower frequencies. Given the general reduction in the Vaisala frequency with depth, more modes will be present near the cutoff frequency to sharpen the spectral peak. Deeper measurements by Voorhis(1968), Cairns (in press) and Briscoe (pers. comm.) appear to substantiate this assertion.

Given the large number of observations, it seems reasonable to conclude that internal wave induced Vaisala "ringing" of the deep sea is a common phenomena, which is associated with up to half the vertical kinetic energy present in the sea.

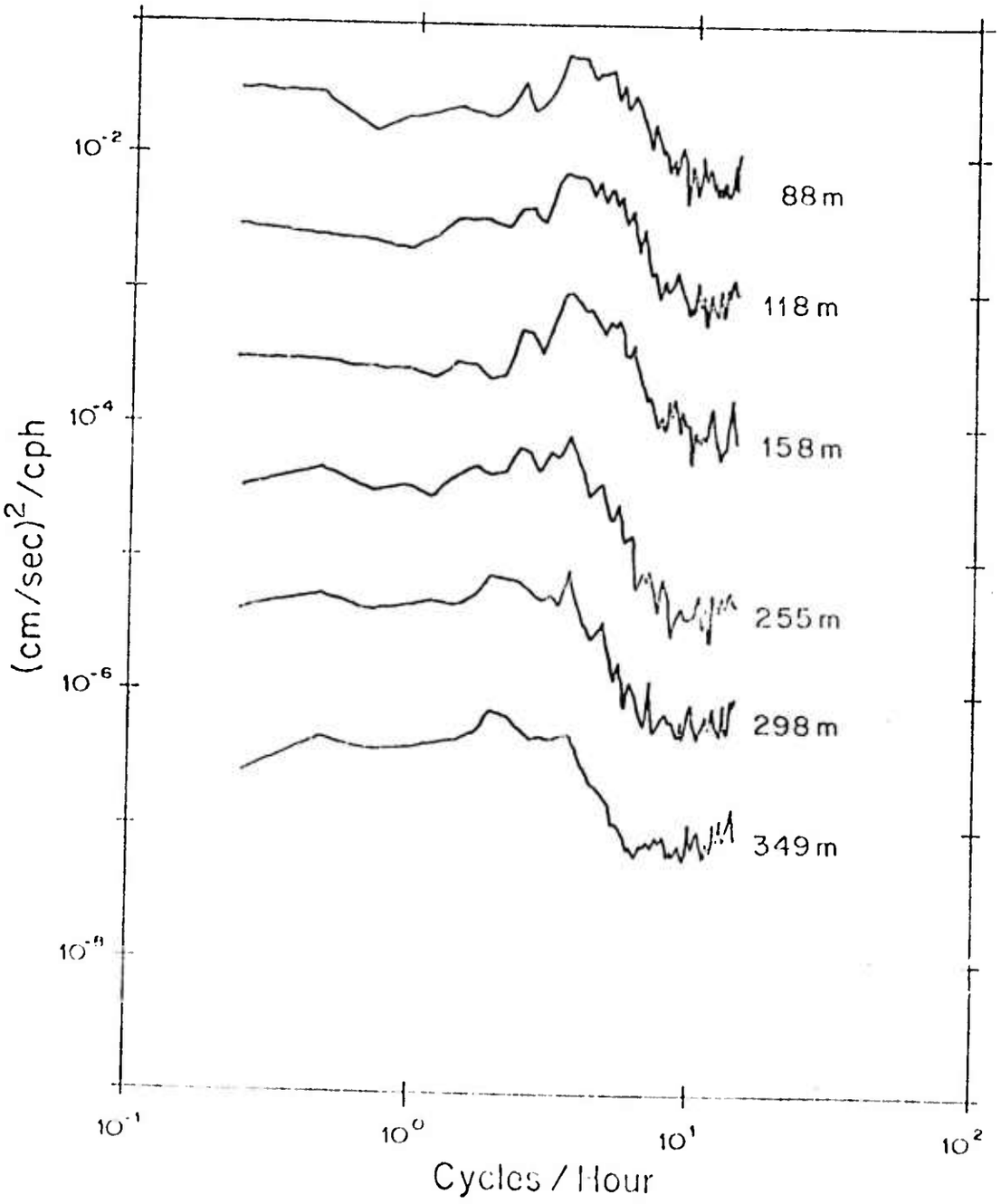

Figure 16. November 1972: Vertical velocity spectra 64 df.

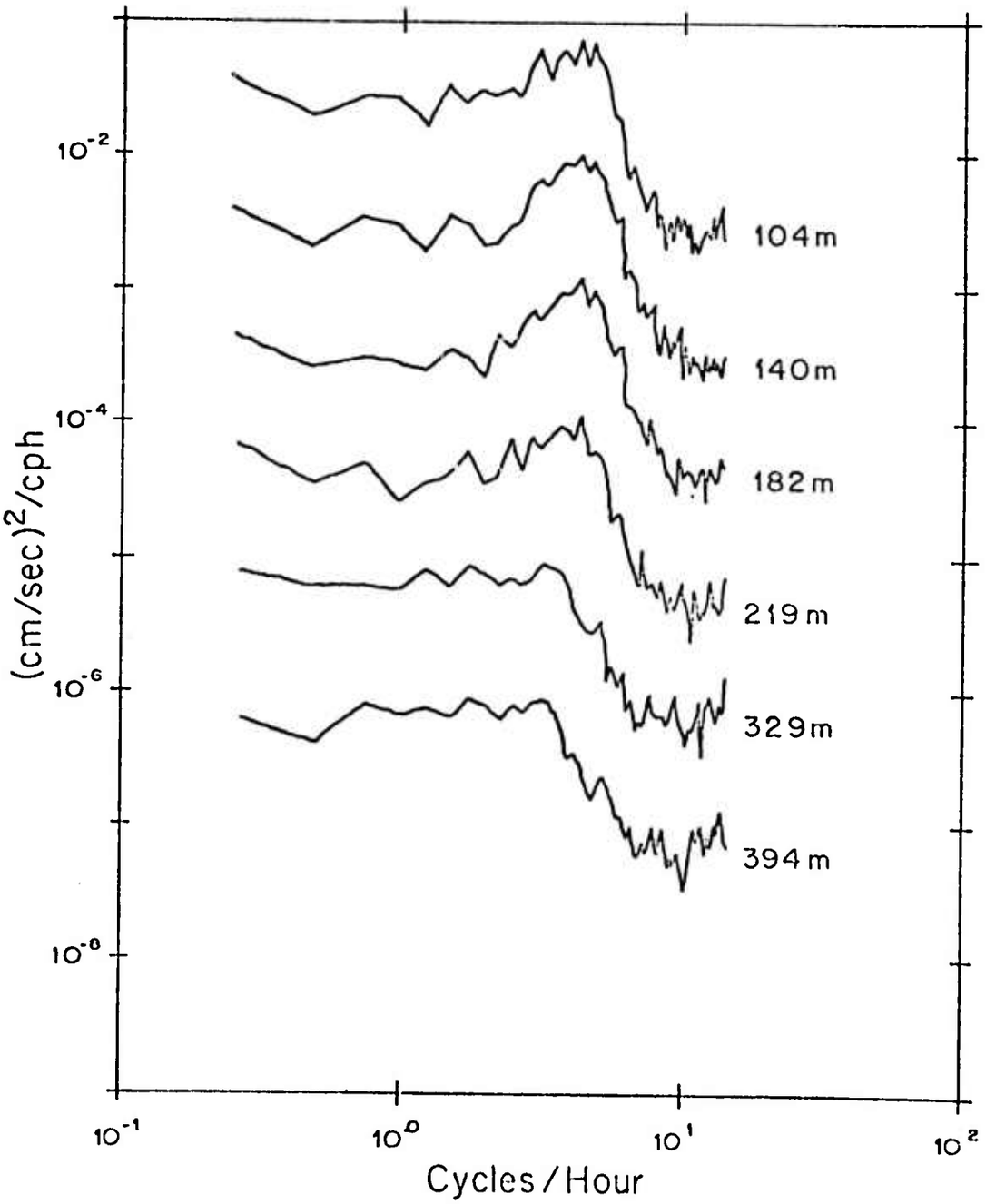

Figure 17. June 1973: Vertical velocity spectra 48 df.

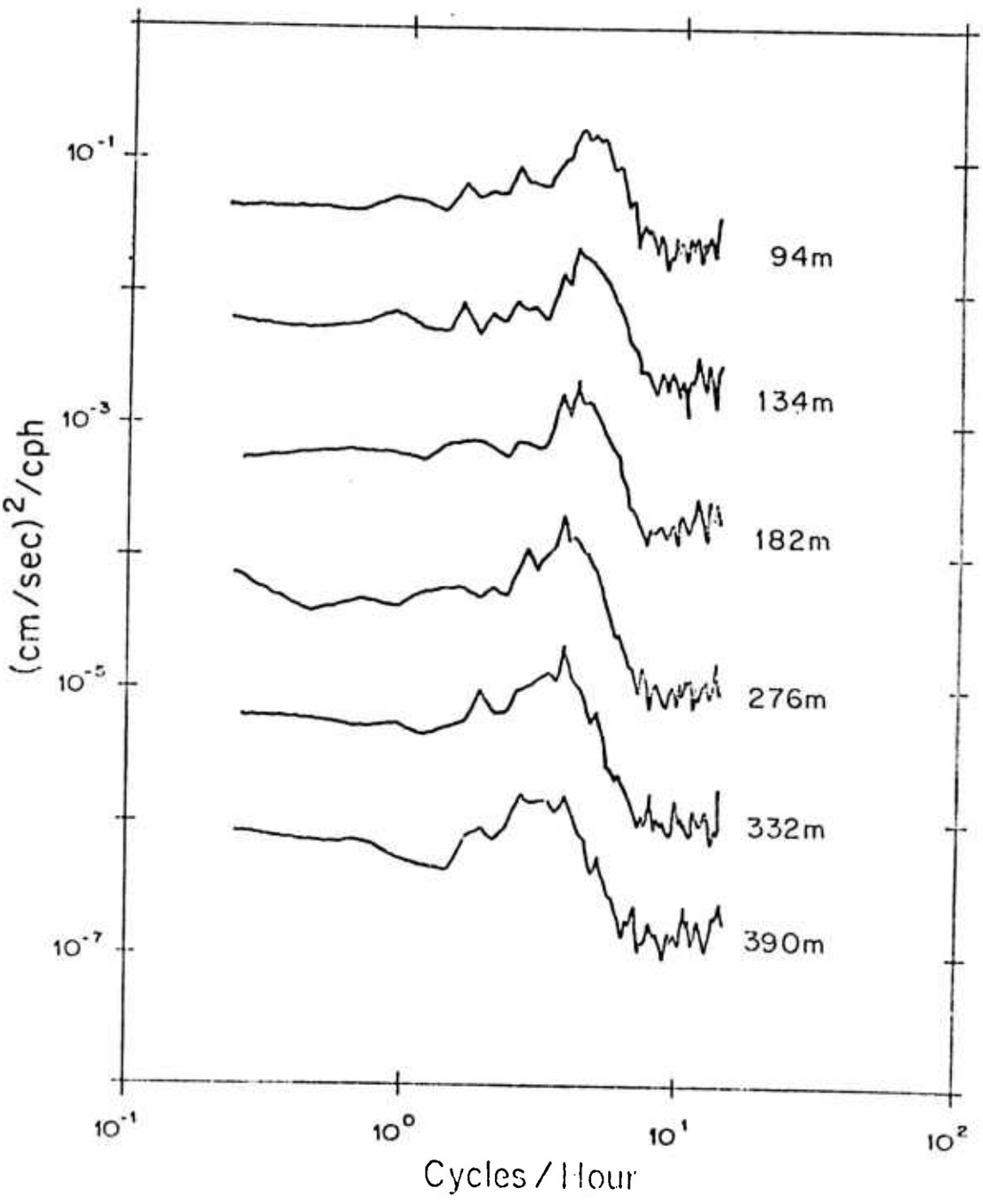

Figure 18. November 1973: Vertical velocity spectra 72 df.

TABLE I

VERTICAL VELOCITY VARIANCE

November 1972		June 1973		November 1973	
Depth m	Variance cm^2/sec^2	Depth m	Variance cm^2/sec^2	Depth m	Variance cm^2/sec^2
88	.2924	104	.2713	94	.7860
118	.3748	140	.3460	134	.8211
158	.3920	182	.3901	182	.6984
255	.2847	219	.3687	276	.5383
298	.3018	329	.3657	332	.5301
239	.2663	394	.3498	390	.5808

The Vertical Cross Spectrum

The depth variability of the wave field can be further studied through estimates of the vertical cross spectrum

$$VC(z_1,z_2,\Omega) = CR(0,z_1,z_2,\Omega) \ .$$

Cross spectra are, in general, complex functions of frequency and spatial separation. Considering sinusoidal waveforms, Munk et al. (1964) has related the real part of the cross spectrum (co-spectrum) to the sum of the energy propagating from measurements points $\bar{x}_1$ to $\bar{x}_2$ and $\bar{x}_2$ to $\bar{x}_1$. The imaginary part (quadrature spectrum) was related to the difference in energy propagation. It can be verified that the same result applies for internal wave vertical functions. It follows that our wave field model, which assumes no net vertical energy flux, requires that the vertical cross spectrum will be real

$$VC(z_1,z_2,\Omega) = \langle \eta(x_0,z_1,\Omega)\eta^*(x_0,z_2,\Omega)\rangle$$

$$= \int_0^\infty \int_0^{2\pi} \langle dA dA^*(\kappa,\theta,\Omega)\rangle \ W(\kappa,\Omega,z_1)W(\kappa,\Omega,z_2) \ .$$

κ θ

The ratio of quadrature spectrum estimate to the co-spectrum estimate will thus serve to quantify the extent to which the assumption of standing waves in the vertical is appropriate.

To increase the statistical stability of the vertical cross spectral estimate, a depth lag averaging technique was utilized. In

a given frequency band, averages were formed of cross spectral estimators of like value of the W.K.B. stretched separation depth

$$\Delta Z = \frac{1}{\bar{N}} \int_{z_1}^{z_2} N(z)dz,$$

producing a final estimate which is a function not of z_1 and z_2 but only the stretched separation distance ΔZ. Implicit in this procedure is the assumption that, aside from the scale distortion caused by the variation of N in the vertical, the wave field is otherwise statistically stationary with depth.

Contour plots of the vertical co-spectrum and quadrature spectrum of the Hawaii data are presented in Figure 19. Both spectra are normalized by $\mathrm{Re}(VC(o,\Omega))$. The quadrature spectrum varies irregularly, rarely exceeding $\pm$ .1. The quadrature spectrum/co-spectrum ratio is correspondingly small, except at large separations, where the co-spectrum also becomes small. Given these spectra, the assumption of zero net vertical energy flux appears to be a justifiable first approximation.

The Vertical Squared Coherence

A normalization of the vertical cross spectrum, the vertical squared coherence

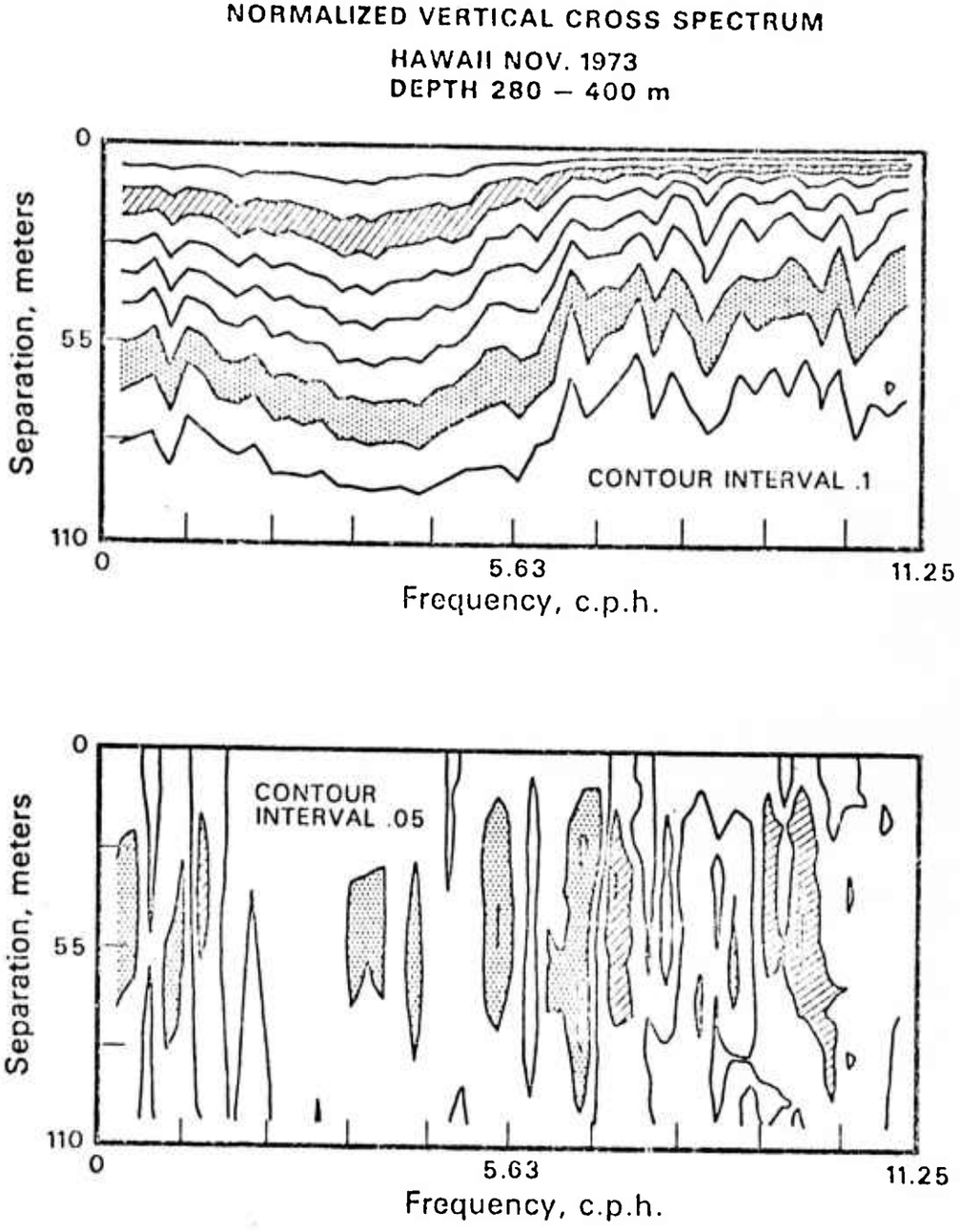

Figure 19. Normalized vertical co-spectrum (upper) and quadrature spectrum (lower) 52 df. Slashed region denotes co-spectrum between .7 and .8; quadrature spectrum between .05 and .1; dotted region denotes co-spectrum between .2 and .3; quadrature spectrum between -.05 and -.1

$$VR^2(\Delta z,\Omega) = \frac{VC(\Delta z,\Omega)^2}{VC(o,\Omega)^2}$$

is most frequently used to gain insight into the distribution of energy with vertical "mode". Munk and Phillips (1968) using sinusoids, have identified small values of the squared coherence in a given frequency band with the relationship

$$\Delta k_z \, \Delta z \sim O(1)$$

where Δk_z is an effective bandwidth of energetic wavenumbers. Using Bessel functions as representative of internal vertical wavefunctions, Garrett and Munk (1972) found the same expression generally applicable.

It should be noted that the assumption of random phase is necessary in the development of the above relationship. In the present case, the measurements might be sufficiently near the sea surface that the phase of the vertical wavefunctions might not yet be decorrelated. A more precise relationship could be developed. However, the coherence provides information primarily about the major spectral concentrations, and is not sensitive to secondary concentrations down many db from the main peaks, which might play a disproportionally large role in the dynamics of the wave field. As a result, major effort will be expended in a more direct estimation of the κ dependence of $d\hat{E}(\kappa,0,\Omega)$.

The difficulty with the coherence technique is that experimental noise can have a strong effect on the measured coherences,

resulting in erroneous bandwidth interpretations. Random instrument noise typically acts to reduce the coherence calculated between pairs of probes. In the present case, where measurements at many depths are made with a single instrument, noise tends to offset the isotherm displacement estimates uniformly, increasing the measured coherences. The coherence spectra to be shown display significant coherences at frequencies above the Vaisala cutoff. This is attributable to the dominance of thermometer noise in the data in this frequency range. At frequencies below N(z), where there is a significant internal wave signal (the signal to noise ratio is much greater) this effect is not important. The error effects can be "reversed" by calculation of vertical coherences between isotherms followed by separate thermometers (Fig. 21). Further, the "slant" coherence between isotherms followed from separate profilers on FLIP was calculated. This was based on information taken from separate vibratrons and therometers. Vibratron noise contributed insignificantly to the difference between the vertical and slant coherence.

Contour plots of the squared coherence estimate versus stretched depth separation and frequency are given in Figure 20. The actual pattern of the contours is quite striking, and represents a significant departure from past observations. At all frequencies where there is substantial wave energy, the coherence is above .5 (coherence squared above .25) out to a separation of 50 m. The coherence associated with a given vertical separation tends to increase slowly and irregularly with increasing frequency to 2.5 cph. Then the

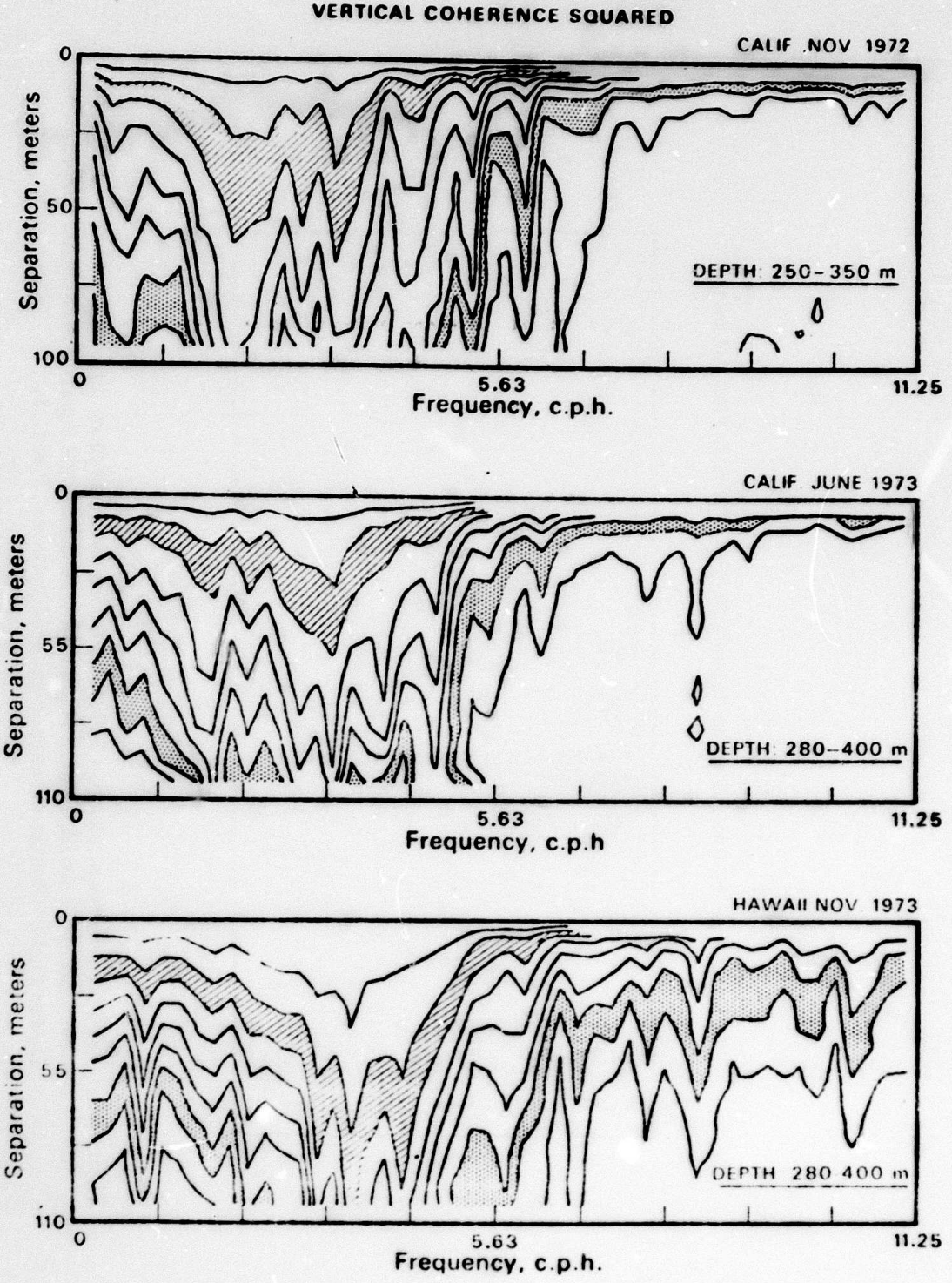

Figure 20. Vertical coherence squared. November 1972-72 df; June 1973-48 df; November 1973-52 df; slashed region denotes coherence squared between .7 and .8; dotted region denotes coherence squared between .2 and .3.

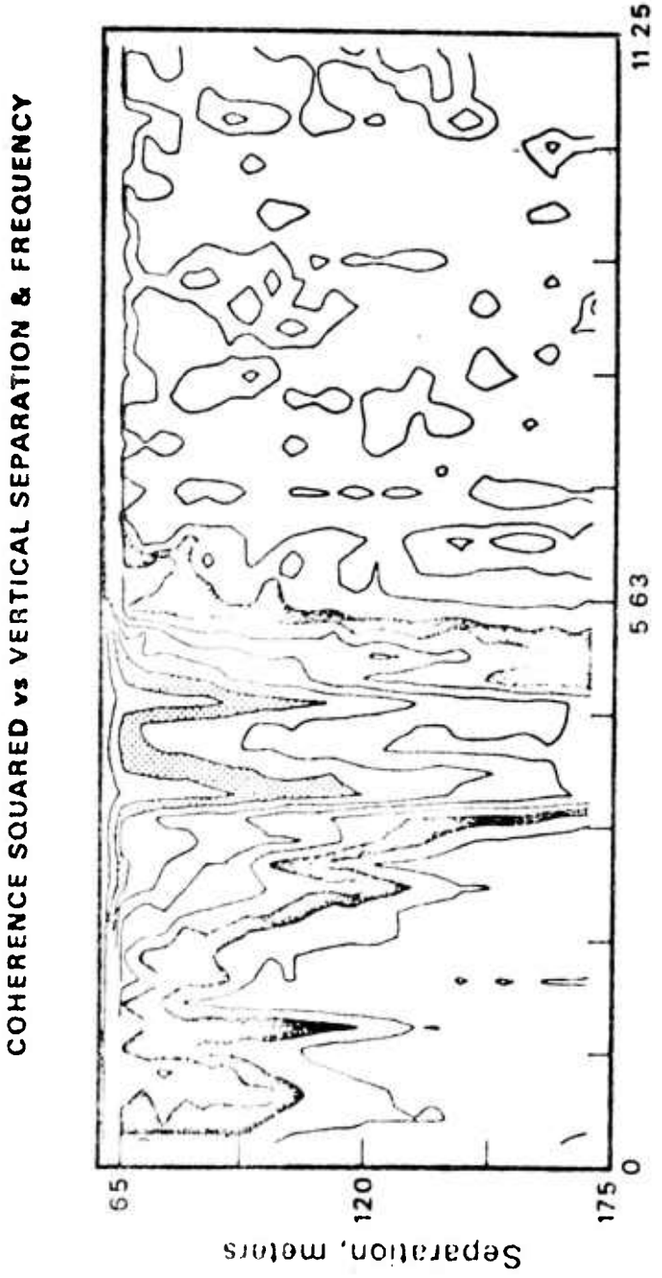

Figure 21. Vertical coherence squared between isotherms followed by different thermometers November 1973-36 df; shaded region denotes coherence squared between .2 and .3. Dotted region denotes coherence squared between .7 and .8.

increase becomes extremely rapid. From 4 cph to the Vaisala cutoff the vertical motions in the upper thermocline are significantly coherent for depth separations in excess of 170 meters. Above N(z), the coherence drops abruptly. Its behavior is determined by the above mentioned thermometer noise (Fig. 20) or the statistical instability of the estimate (Fig. 21).

The high values of the squared coherence and the trend toward increasing coherence with increasing frequency (for fixed separation) sharply contrast with much of the vertical coherence information obtained by previous workers (Seidler, White). Particularly disparate is the pioneering study of Webster (1972) who used moored, fixed depth current meters. His observations indicated that the depth separation associated with the .5 coherence contour should decrease with increasing frequency, reaching a separation of 13 meters at 1 cph. Garrett and Munk (1972) have attributed this discrepancy to the microstructure contamination of Webster's fixed depth instruments.

Recent results of Cairns, measuring temperature from a profiling midwater float (personal communication) and Briscoe, measuring temperature from a surface spar buoy (personal communication) tend to substantiate the general pattern seen in this experiment.

The vertical coherence results suggest that high frequency vertical motions in the upper thermocline are dominated by motion of small vertical wavenumber. Lower frequency motions are associated either with larger vertical wavenumbers, a wider range of energetic wavenumbers, or some combination of the two effects. Next a direct

resolution of the vertical spectrum will be attempted in hopes of further examining the above uncertainty.

The Wavenumber Frequency Spectrum from Vertical Separation

The objective of this section is the estimation of the wavenumber frequency spectrum

$$dE(\kappa,\omega) \equiv \int_{\theta=0}^{2\pi} dE(\kappa,\theta,\omega)$$

from the depth/time variability of the wave field. The motivation for this effort can be seen in Figure 22, in which the complex isotherm displacement Fourier coefficients $\eta(\bar{x}_o,z,\Omega)$ in a given frequency band are plotted versus depth. The smooth undulation of the Fourier coefficients with depth is the inducement to attempt a vertical spectral analysis of the data.

The procedure to be used is considerably more complex than standard time series analysis techniques due to the depth variability of the Vaisala frequency. There are two important operational consequences of this nonstationarity. First, unlike standard time series analysis, the potential energy is not directly given by the total integrated variance of the measured signal. Statistical operations which conserve potential energy, not variance, must be employed. Second, sinusoids are not the natural set of orthogonal functions appropriate for the decomposition of the signal. Fourier analysis

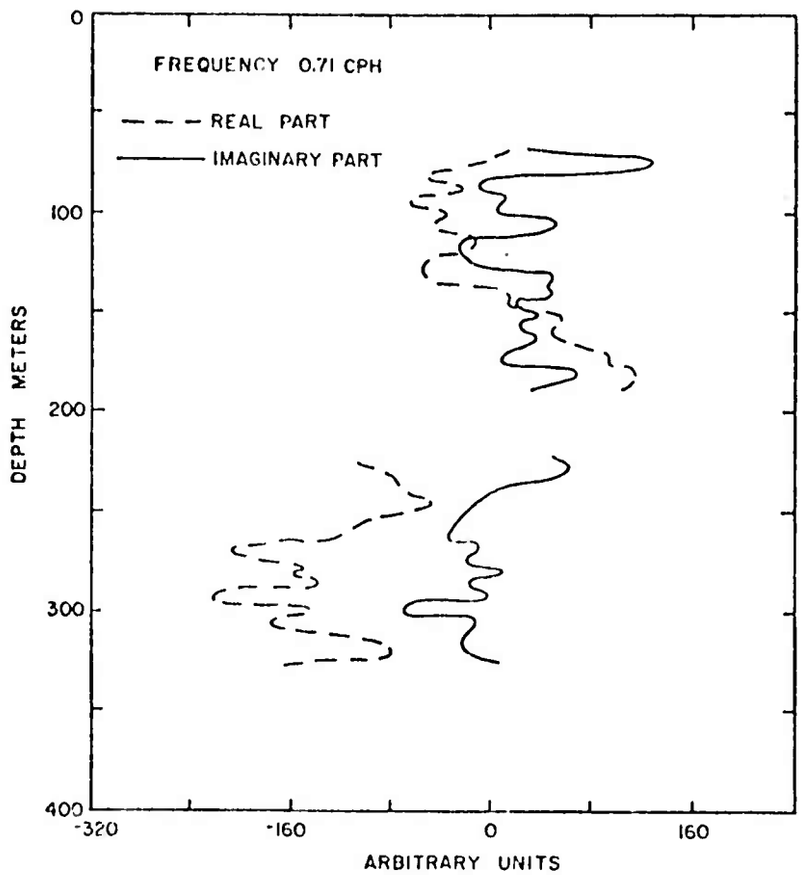

Figure 22. Depth variation of complex Fourier coefficients $\eta(x_j, z, \Omega)$. November 1972 data, $\Delta\Omega = .12$ cph.

would result in vertical "wavenumber" coefficients which are not statistically independent. Indeed, the concept of a vertical wavenumber is meaningful only in the W.K.B.sense. In the analysis outlined below, the necessity for dealing with vertical wavenumber will be avoided; equivalent horizontal wavenumber magnitude

$$k_H = k_z(z) \left(\frac{N^2(z) - \Omega^2}{\Omega^2 - f^2}\right)^{-1/2}$$

will be utilized instead.

For each horizontal position $\bar{x}_j$, there are averaged values of $\eta(\bar{x}_j, z_i, \Omega)$ in forty depth intervals z_i. These complex non-stationary depth series are to be expanded as a sum of yet unspecified orthogonal functions.

$$\eta(x_j, z_i, \Omega) = \sum_{n=1}^{40} a_n(x_j, \Omega)\, F_n(z_i)$$

with

$$a_n = \int_D \eta(z)\, F_n(z)\, Y(z)\, dz$$

where D is the depth interval spanned by the array, F_n is the n^{th} function in the orthogonal set, and Y is a weight function to be determined.

The functions $\{F_n\}$ should be chosen such that the resulting separation coefficients $\{a_n\}$ are statistically independent, i.e.,

$$\langle a_i a_j^* \rangle = \langle |a_i|^2 \rangle \delta_{ij} .$$

Also, in order that the average potential energy be given by the sum of the squares of the coefficients $\{a_n\}$ it is necessary that

$$\sum_{n=1}^{40} \langle |a_n|^2 \rangle = 1/2 \, \rho D^{-1} \int_D N^2(z) \langle |\eta(z,\Omega)|^2 \rangle \, dz.$$

It can be demonstrated (Appendix II) that the functions $F_n(z_i) = G_n(z_i)/N(z_i)$, where G_n are the eigenfunctions of the N weighted vertical co-spectral matrix,

$$[N(z_i) \text{ Re } VC \, (z_i, z_j, \Omega) \, N(z_j)]$$

are the desired orthogonal functions, under weighting $N^2(z_i)$. The resulting separation coefficients $\{a_n\}$ are independent. The variance $\langle |a_i|^2 \rangle$ is given by the i^{th} eigenvalue of the matrix and the total variance

$$\sum_{i=1}^{40} \langle |a_i|^2 \rangle,$$

is proportional to the r.m.s. potential energy.

The eigenvalues of the weighted co-spectral matrix are thus a complete energy conserving, statistical description of this linear,

nonstationary process. However, only in special cases will the functions $\{F_n(z_i)\}$ resemble the dynamic functions (in this case the $W(\kappa,\Omega,z_i)$) which are physically meaningful in describing the process. It is necessary to relate the distribution of potential energy among the functions $\{F_n\}$ (as given by the eigenvalues of the matrix) to $\hat{dE}(\kappa,\Omega)$.

The relationship between the eigenvalues and the energy spectrum is given by

$$a_n = \int_D \eta\, F_n\, N^2\, dz$$

$$= \int_\kappa \int_\theta dA(\kappa,\theta,\Omega) e^{i\bar{\kappa}\cdot\bar{x}} \left\{ \int_D W(\kappa,\Omega,z)\, F_n(z)\, N^2(z) dz \right\}$$

$$= \int_\kappa \int_\theta dA\, e^{i\bar{\kappa}\cdot\bar{x}}\, C_n(\kappa,\Omega)$$

where

$$C_n(\kappa,\Omega) \equiv \int_D W\, F_n\, N^2\, dz$$

and

$$\lambda_n \equiv \langle a_n^2 \rangle = \int dE(\kappa,\Omega)\, C_n^2(\kappa,\Omega).$$

If $C_n^2(\kappa,\Omega)$ were a delta-like function, strongly peaked at some $\kappa = k_n$, the λ_n could be taken as a weighted estimate of the spectrum near k_n. In the present case the form of the eigenfunctions is strongly influenced by the vertical sampling interval and the functions $\{C_n^2(\kappa,\Omega)\}$ are not sharply peaked.

It is reasonable to compose an estimate $E_k(\Omega)$ of $\hat{dE}(\kappa,\Omega)$ as a linear sum of the eigenvalues:

$$E_k(\Omega) = \sum_{n=1}^{40} \alpha_{kn}\, \lambda_n$$

$$E_k(\Omega) = \int_\kappa \sum_{n=1}^{40} \alpha_{kn}\, C_n^2\,(\kappa,\Omega) dE(\kappa,\Omega)$$

$$E_k(\Omega) = \int_\kappa W_k(\kappa,\Omega)\; \hat{dE}(\kappa,\Omega)\,.$$

The α_{kn} are usually chosen to make the spectral window

$$W_k(\kappa,\Omega) \equiv \sum_n \alpha_{kn}\, C_n^2(\kappa,\Omega)$$

as delta-like as possible. This is done by minimizing the square of the window outside of a desired passband.

In this case, where it was assumed that the spectrum $\hat{dE}(\kappa,\Omega)$ would tend to decrease with increasing κ, the square of the weighted

window $\kappa^{-n} W_k(\kappa,\Omega)$ was minimized outside of the passband. This had the effect of minimizing the error in the spectral estimate

$$\varepsilon_k = \int_{\kappa \neq k_H} W_k(\kappa,\Omega)\ \hat{dE}(\kappa,\Omega) = \int_{\kappa \neq k_H} W_k(\kappa,\Omega)/\kappa^n$$

assuming a κ^{-n} form for dE.

Trial sections of data were repeatedly analyzed with windows weighted by a factor κ^{-2}, $\kappa^{-1.5}$, κ^{-1} and κ^{0}. The weighting had only a slight effect on the slopes of the resulting spectral estimates $E_k(\Omega)$. A κ^{-1} weighting was finally chosen as it tended to produce a slightly smoother spectral estimate.

For each cruise, sixteen weighted vertical co-spectral matrices were calculated from the sample cross-spectrum for sixteen frequency bands, .23 cph to 3.75 cph. The analysis was not performed at higher frequencies as the high vertical coherences observed above 4 cph suggested that the first mode was strongly dominant in this region. The eigenfunctions and eigenvalues for these 40 x 40 matrices were then obtained.

From measured representative Vaisala profiles for each cruise, theoretical vertical wavefunctions $W(\kappa,\Omega,z)$ were numerically calculated by integrating the linear internal wave equation with the initial condition $W = 0$ at $z = 0$. For each frequency, the equation was integrated for 120 evenly spaced values of κ. The wavenumber increment Δk was chosen such that the maximum wavenumber $\kappa_{max} = 120\ \Delta k$

corresponded to a wave function which had twenty zero crossings from the surface down to 440 m. The functions were normalized such that

$$\frac{\rho}{2D} \int_D N^2 W^2 dz = 1 .$$

Using the previously calculated eigenfunctions, a 40 by 120 array of coefficients

$$C_n(\kappa,\Omega) = C_{n\kappa}(\Omega) = \int_D N^2(z)\, F_n(z)\, W_\kappa(\Omega,z)dz$$

was calculated in each frequency band.

The coefficients α were then found which minimized

$$w_k{}^2(\kappa,\Omega)/\kappa^2 \equiv W_{k\kappa}(\Omega)/\kappa^2$$

outside of the desired passband, subject to the constraint $W_{k\kappa} = 1$ in the passband.

Forty spectral estimates $E_k(\Omega)$ were produced in each frequency band for values of $k = 3 * \ell * \Delta k$, $\ell = 1, 40$. The k correspond to wavefunctions making from 1/2 through 20 oscillations in the top 440 m. With window resolution set at 6 Δk, adjacent estimates were dependent. A contour plot of a representative window function $W_{k\kappa}(\Omega)$ is presented in Figure 23.

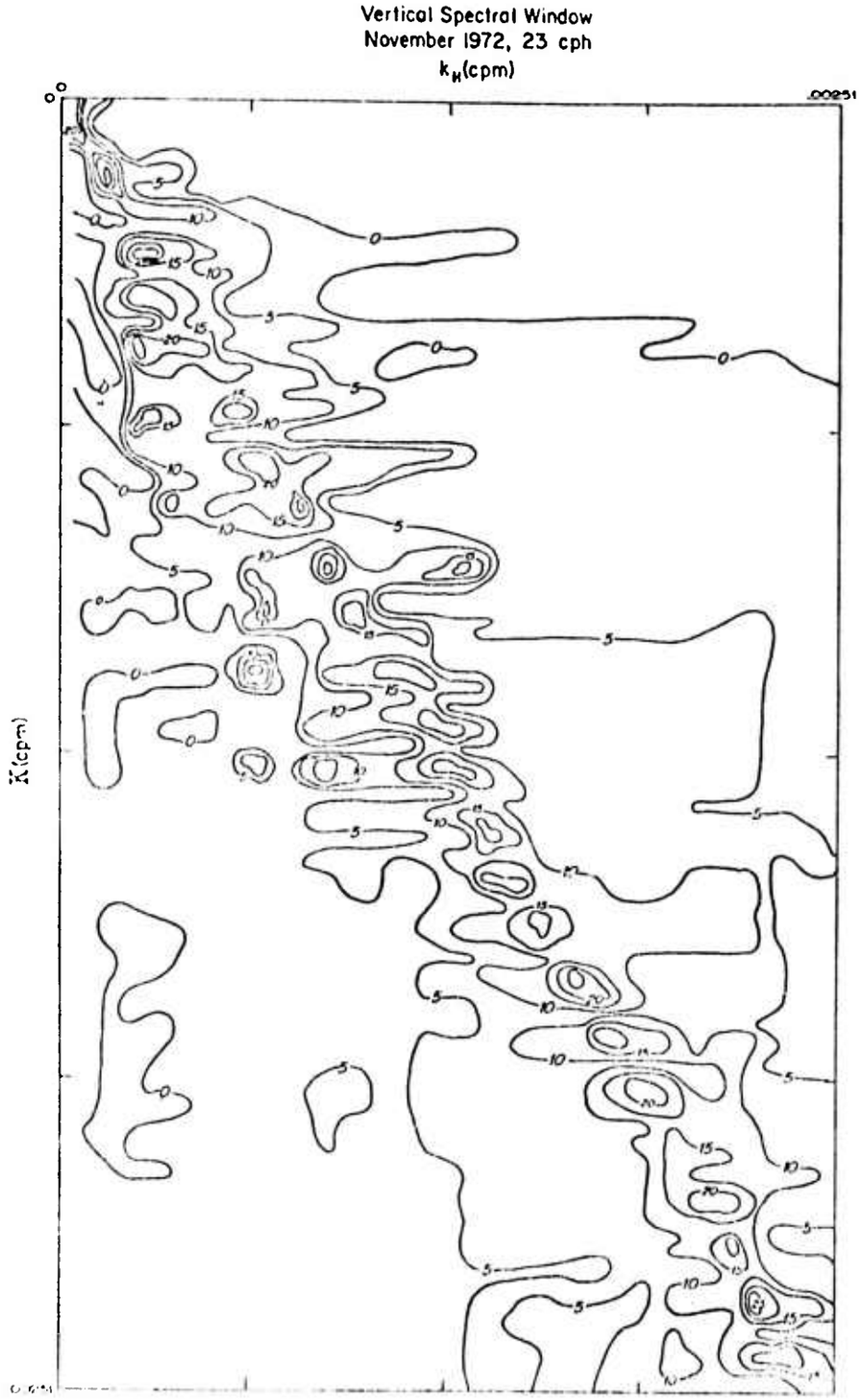

Figure 23. Vertical spectral window. November 1972, .23 cph.

Spectral estimates $E_k(\Omega)$ are plotted for several Ω in Figures 24-26. At all frequencies the dominant energy is associated with vertical scales long compared to the vertical length of the array. The extent to which this long wavelength energy contaminates the rest of the spectrum, given by the spectral window, is plotted as a solid line.

Three spectral regions are apparent. The spectral maximum occurs at long wavelength. At low frequencies, less than ~1.5 cph, the array resolution is sufficient to limit this peak to the first twelve modes. Above ~3 cph the first two modes are clearly dominant. This pattern is compatible with the vertical coherence information previously presented.

The long wavelength maximum drops at an approximate $\kappa^{-1.5}$ to κ^{-2} slope down to a spectral "shoulder". This shoulder region has a κ^{0} to κ^{-1} slope. Only in the lower frequency bands is it clearly above the spectral noise levels.

At higher wavenumbers, the spectral intensity in each frequency band drops precipitously and is quickly contaminated by the sidebands of the long wavelength spectral peak.

This information can be alternately portrayed as a contour map of potential energy versus frequency and horizontal wavenumber (Figs. 27-29). For the November 1972 data, CALCOFI hydrographic data were available from top to bottom of the ocean. Coupled with FLIP-board density estimates in the top 400 m, information was available to generate numerically the linear, shear-free internal wave dispersion

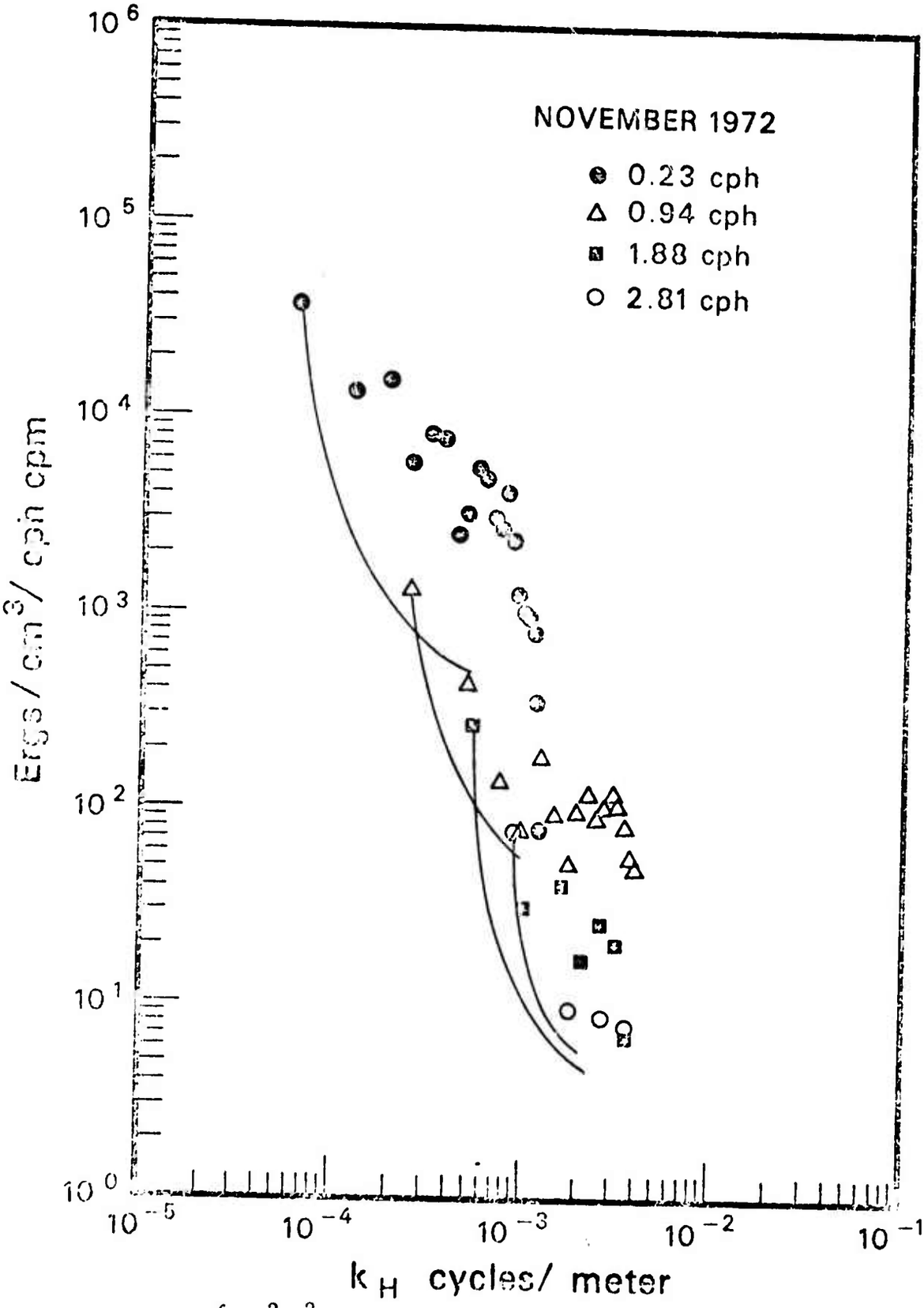

Figure 24. $[1/2D \int_D \rho N^2 W^2 dz \cdot E_{k_H}(\Omega)]$ November 1972. Frequency bandwidth 0.23 cph; ergs/cm^3/cph cpm.

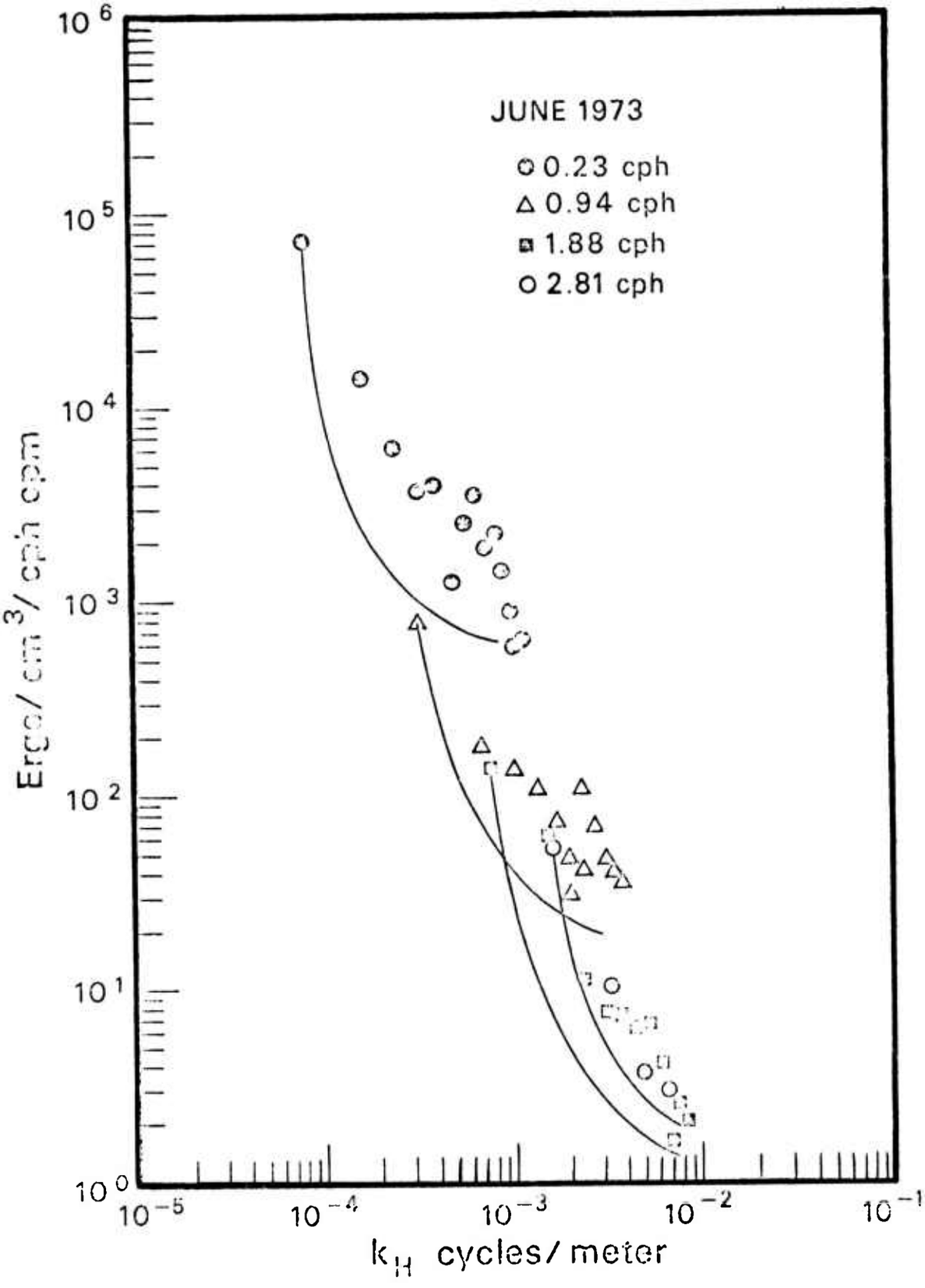

Figure 25. $[1/2D \int_D \rho N^2 W^2 dz] \cdot E_{k_H}(\Omega)$ June 1973. Frequency bandwidth 0.23 cph; wavenumber bandwidth 0.58×10^{-4} cpm; ergs/cm^3/cph cpm

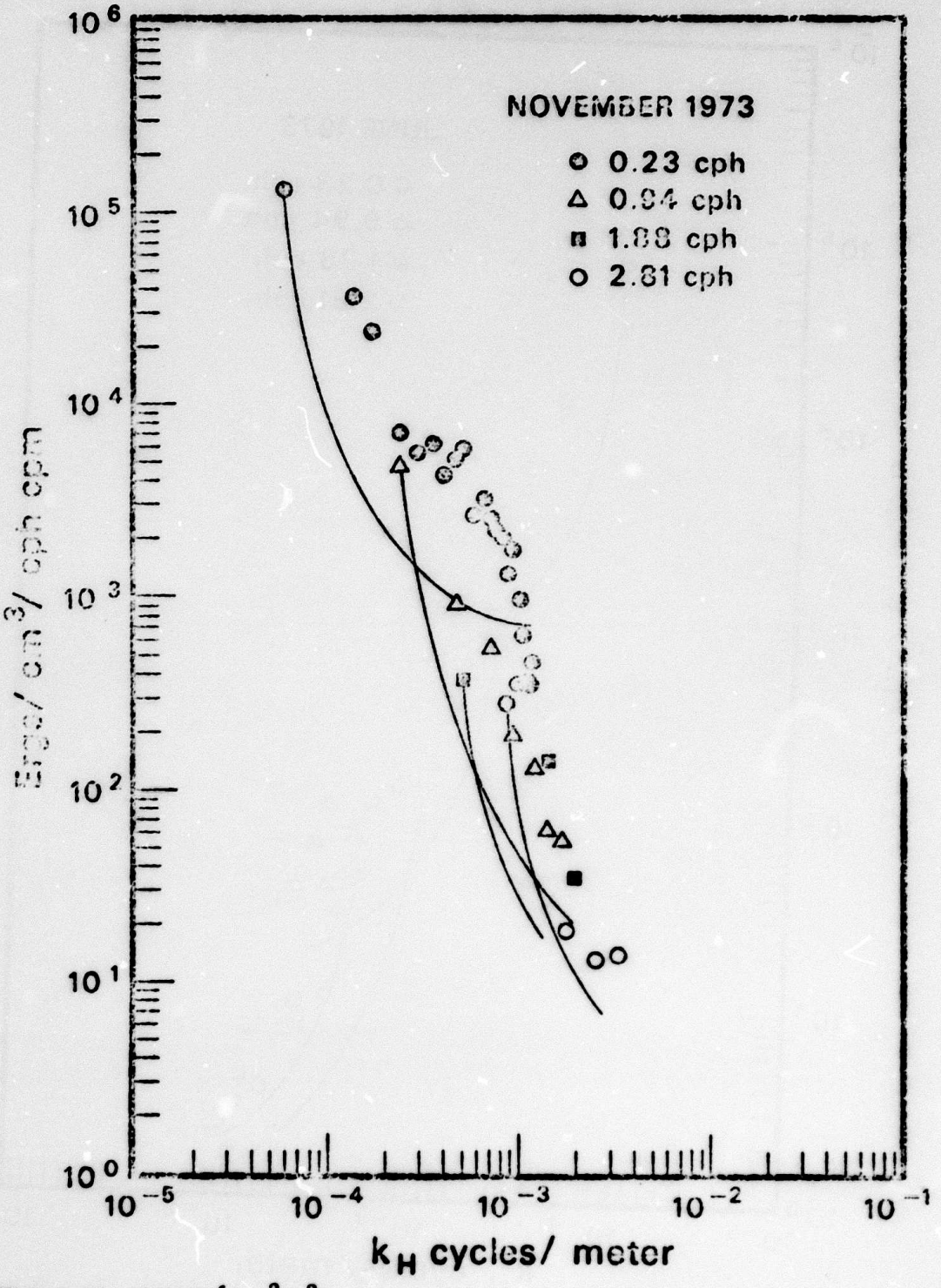

Figure 26. $[1/2D \int_D \rho N^2 W^2 dz \cdot E_{k_H}(\Omega)]$ November 1973. Frequency bandwidth 0.23 cph; wavenumber bandwidth 0.58×10^{-4} cpm; ergs/cm^3/cph cpm

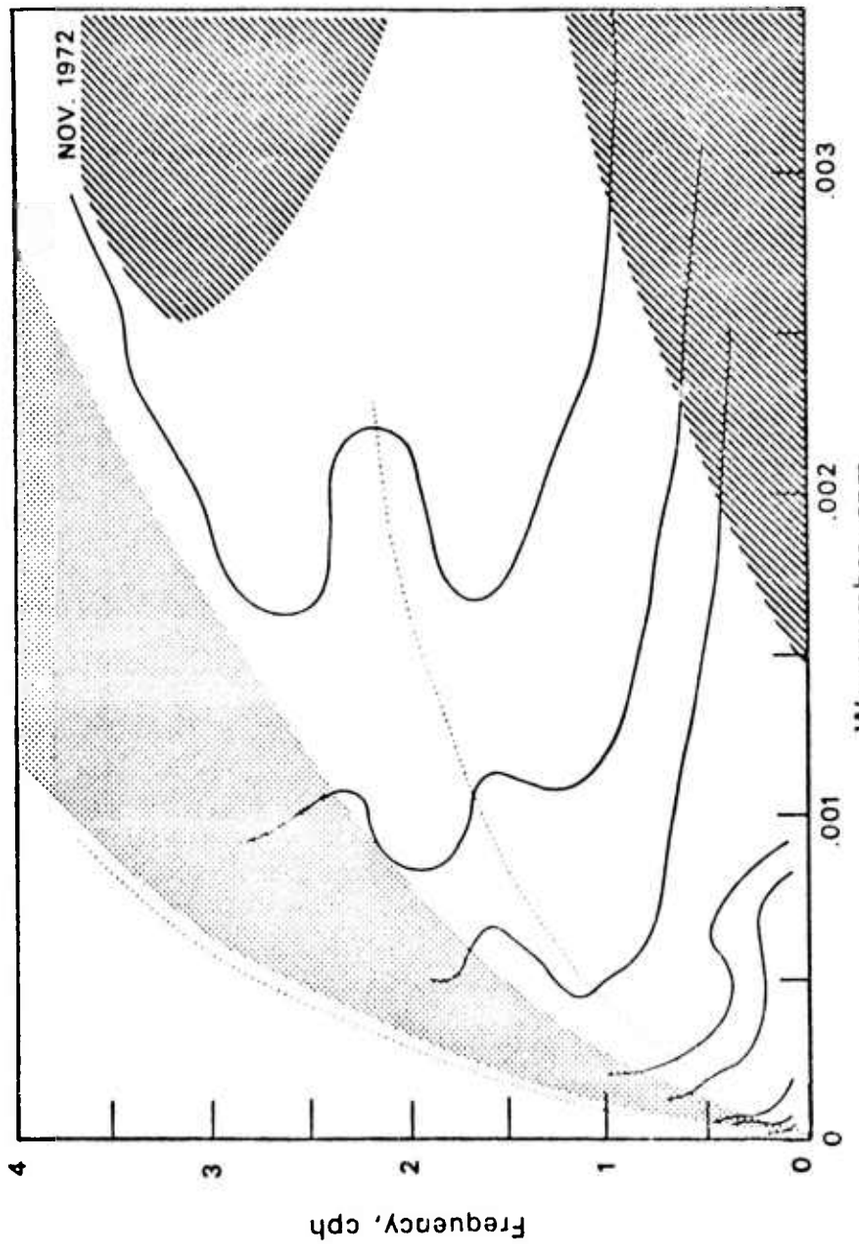

Figure 27. November 1972: Log potential energy versus frequency and wavenumber. Contour interval is 5 db down from 10^5 ergs/cm^3/cph cpm. Dotted lines give first and tenth mode dispersion lines. Dotted region denotes first spectral band, illustrating variation of wavenumber bandwidth with frequency. Slashed areas are probably contaminated by leakage of lower wavenumber energy.

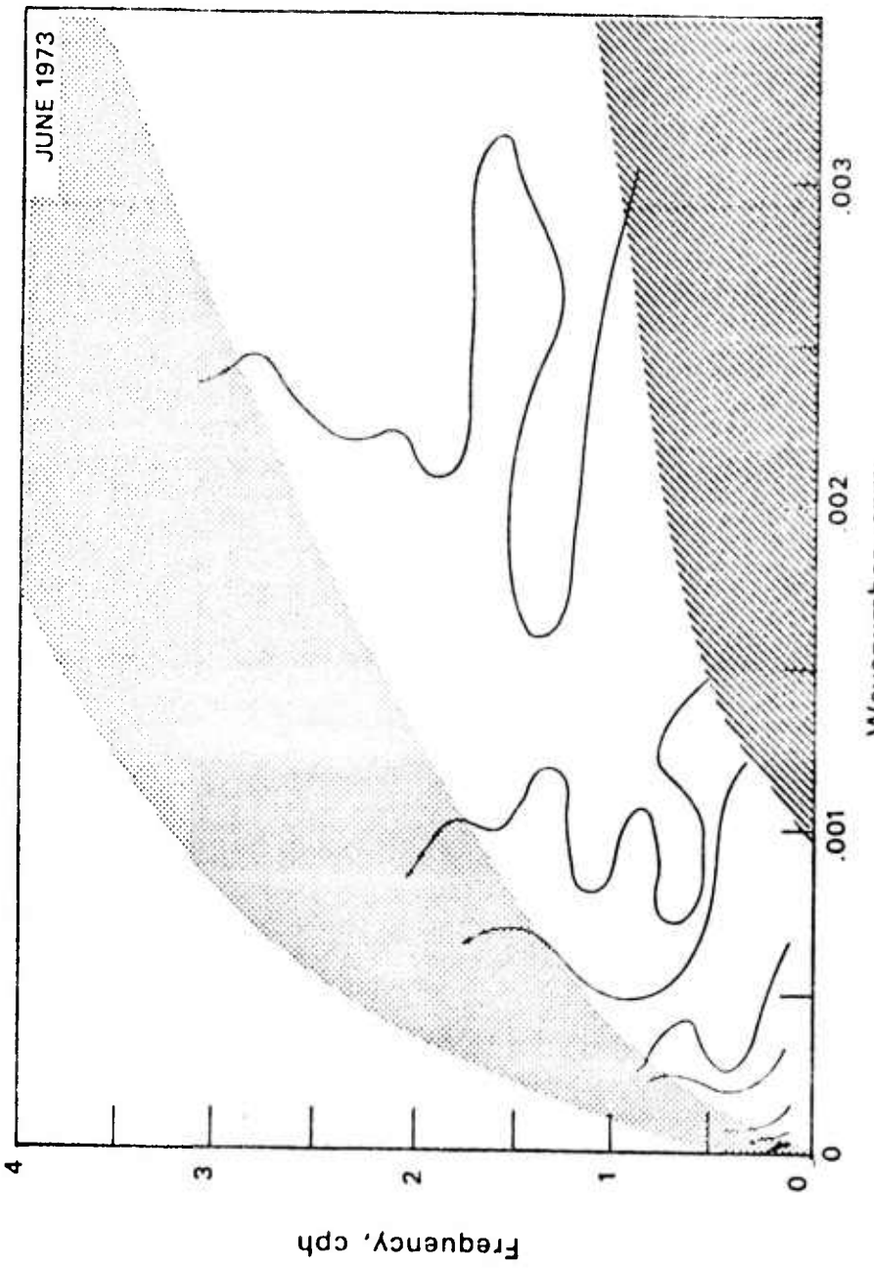

Figure 28. June 1973: Log potential energy versus frequency and wavenumber. Contour interval is 5 db down from 10^5 ergs/cm^3/cph cpm. Dotted region denotes first spectral band, illustrating variation of wavenumber bandwidth with frequency. Slashed areas are probably contaminated by leakage of lower wavenumber energy.

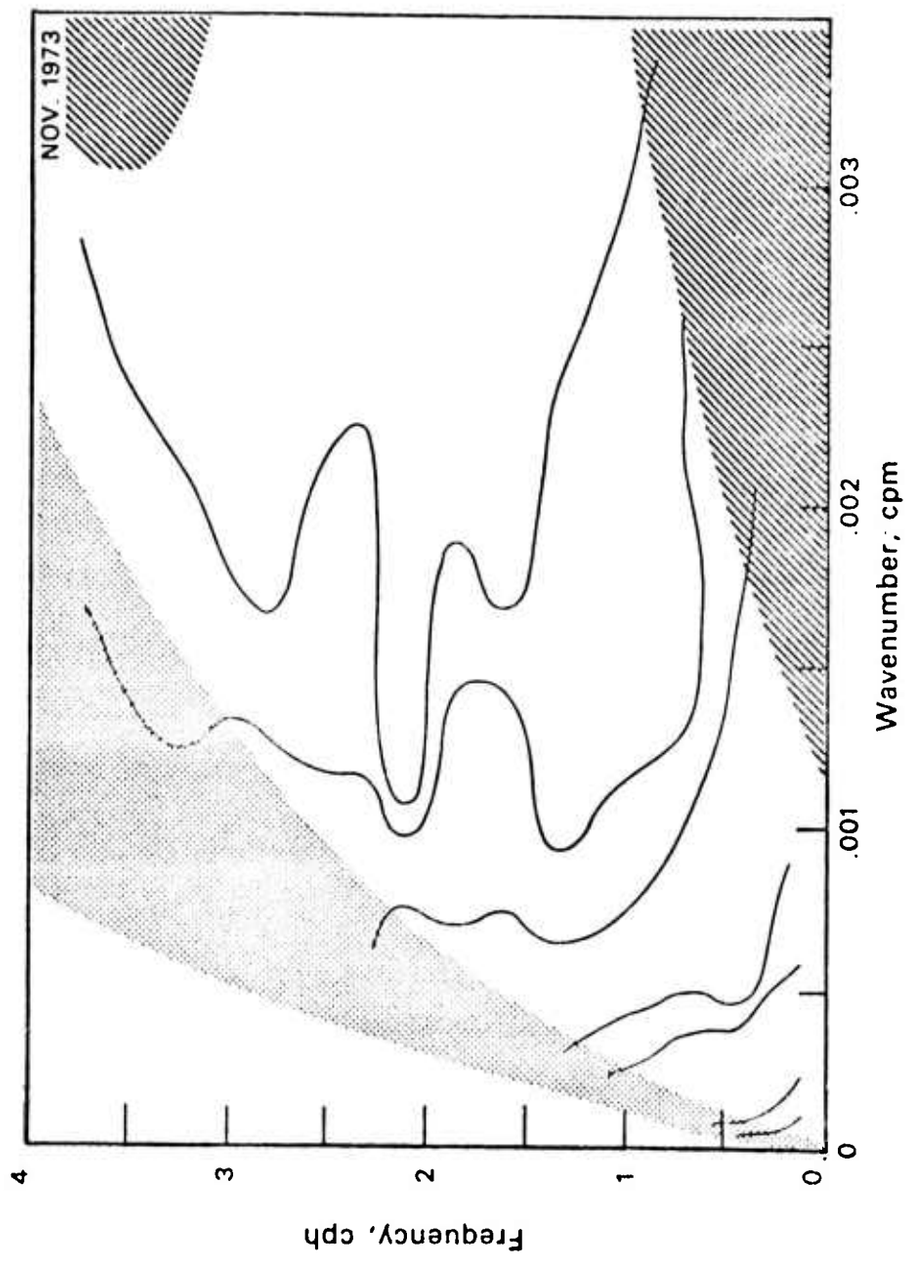

Figure 29. November 1973: Log potential energy versus frequency and wavenumber. Contour interval is 5 db down from 10^5 ergs/cm^3/cph cpm. Dotted region denotes first spectral band, illustrating variation of wavenumber bandwidth with frequency. Slashed areas are probably contaminated by leakage of lower wavenumber energy.

relation, which is also plotted on Figure 27.

It is apparent from these spectra that the number of excited internal wave modes is a strong function of frequency. Above 3 cph, the first mode clearly dominates the spectrum. Spectral levels are undetectably low above the first few modes. Although the greatest amount of energy is in the lower modes (longer horizontal wavelengths) at lower frequencies also, there is significant short wavelength energy, associated with the spectral shoulder. It would be difficult to infer the presence of this short wavelength energy from the vertical coherence information alone, as it is down 10-15 db from the long wavelength spectral maximum.

This information is alternatively contoured versus frequency and W.K.B. equivalent vertical wavenumber

$$k_z = k_H \left(\frac{\bar{N}^2 - \Omega^2}{\Omega^2 - \rho^2}\right)^{1/2}$$

where

$$\bar{N}^2 = \frac{1}{D} \int_D N^2(z)dz$$

in Figures 30-32. The frequency dependence of $E_{k_H}(\Omega)$ can be removed by multiplying by Ω^2. When this is done, the contour lines run nearly parallel to the Ω axis. This suggests a vertical wavenumber bandwidth which is independent of frequency. This simple pattern is deformed at the lowest frequency, corresponding to the increased energy in the spectral shoulder. The agreement with the Garrett-Munk 1974 spectrum is good, except in the region of the spectral shoulder.

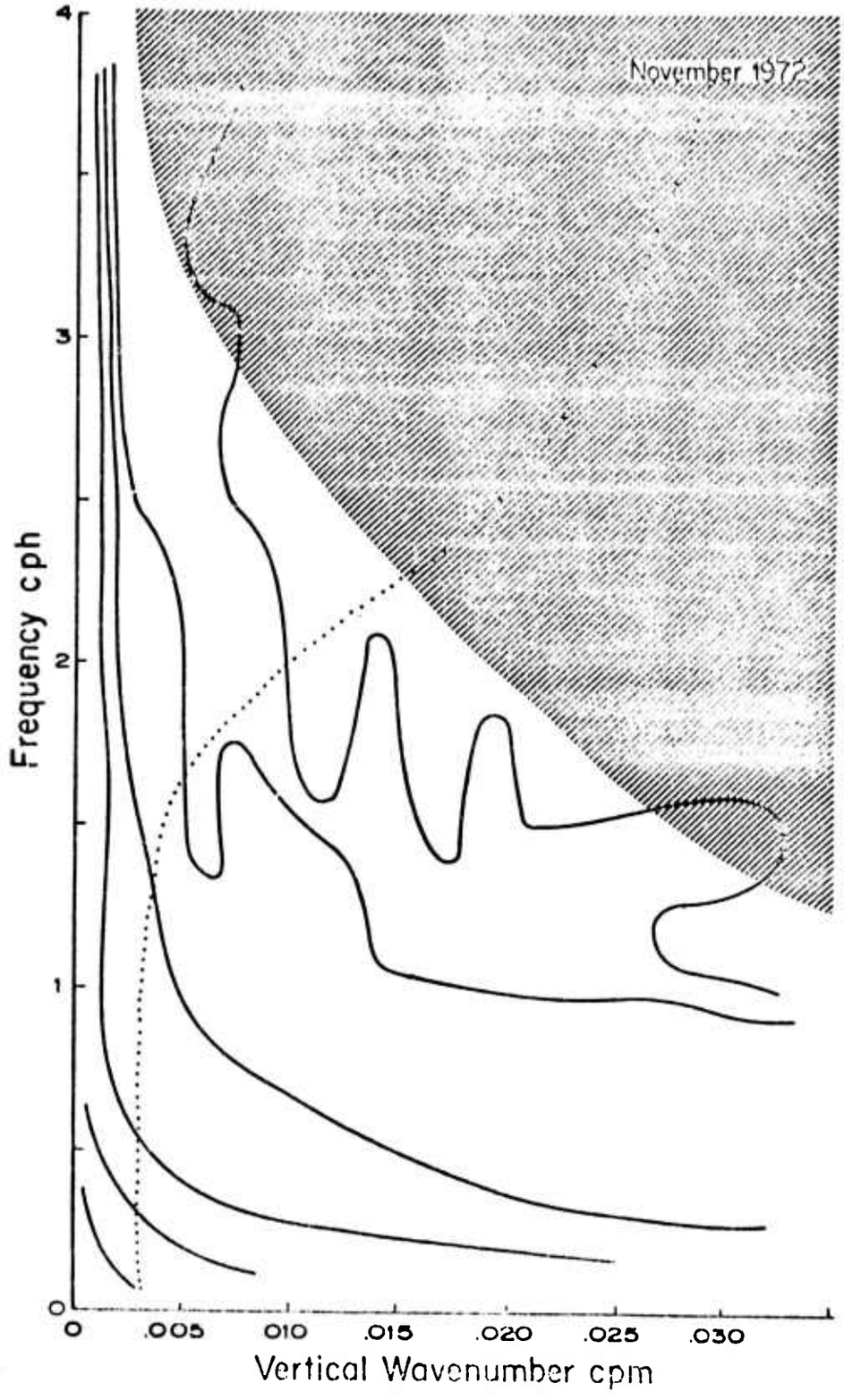

Figure 30. November 1972: Log potential energy versus frequency and W. K. B. vertical wavenumber. Contour interval is 5 db down from $.32 \times 10^4$ ergs/cm^3/cph cpm. Dotted line represents 10th mode dispersion line. Slashed region is probably contaminated by leakage of low wavenumber energy.

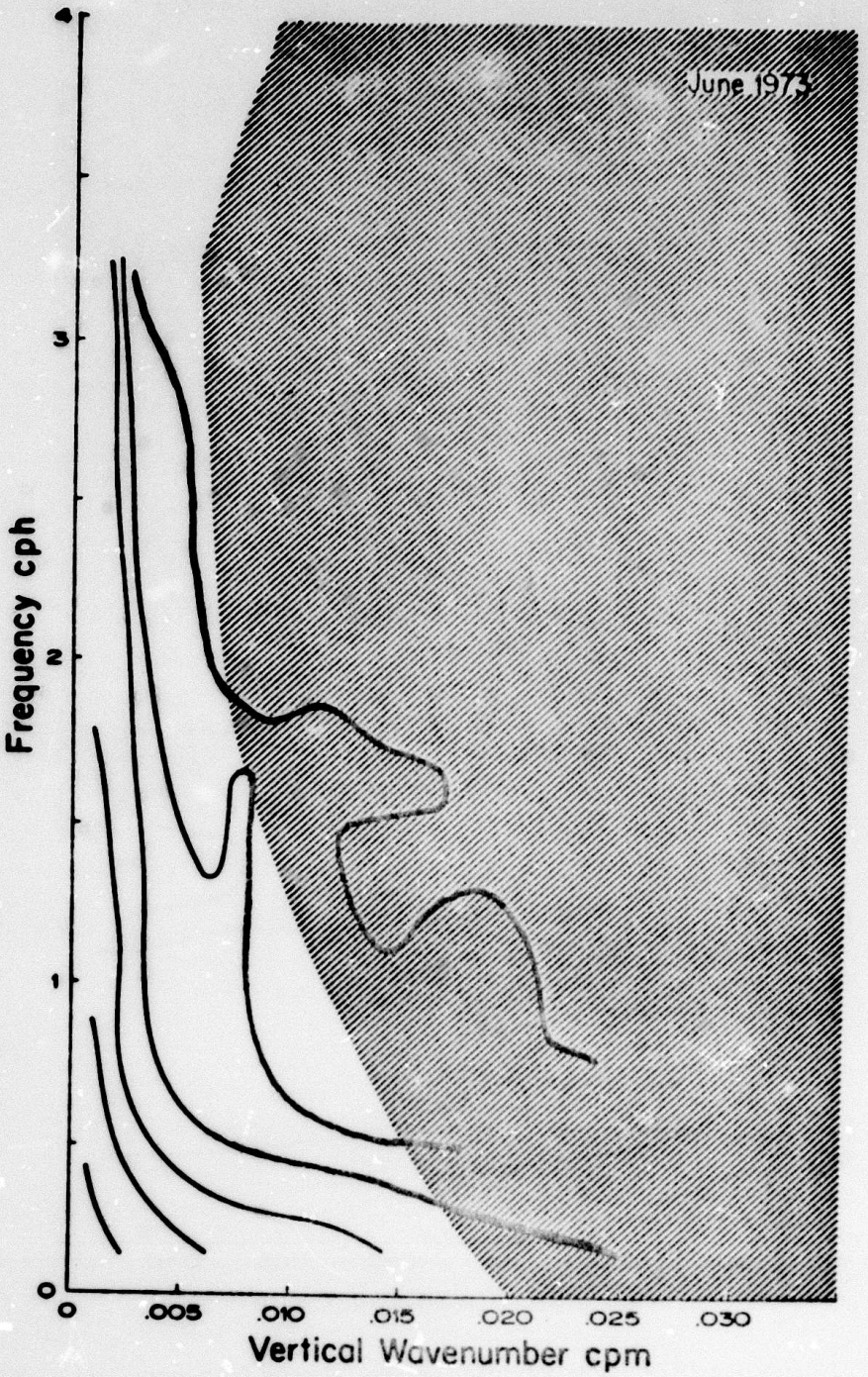

Figure 31. **June 1973: Log potential energy versus frequency and W. K. B. vertical wavenumber. Contour interval is 5 db down from $.32 \times 10^4$ ergs/cm^3/cph cpm. Slashed region is probably contaminated by leakage of low wavenumber energy.**

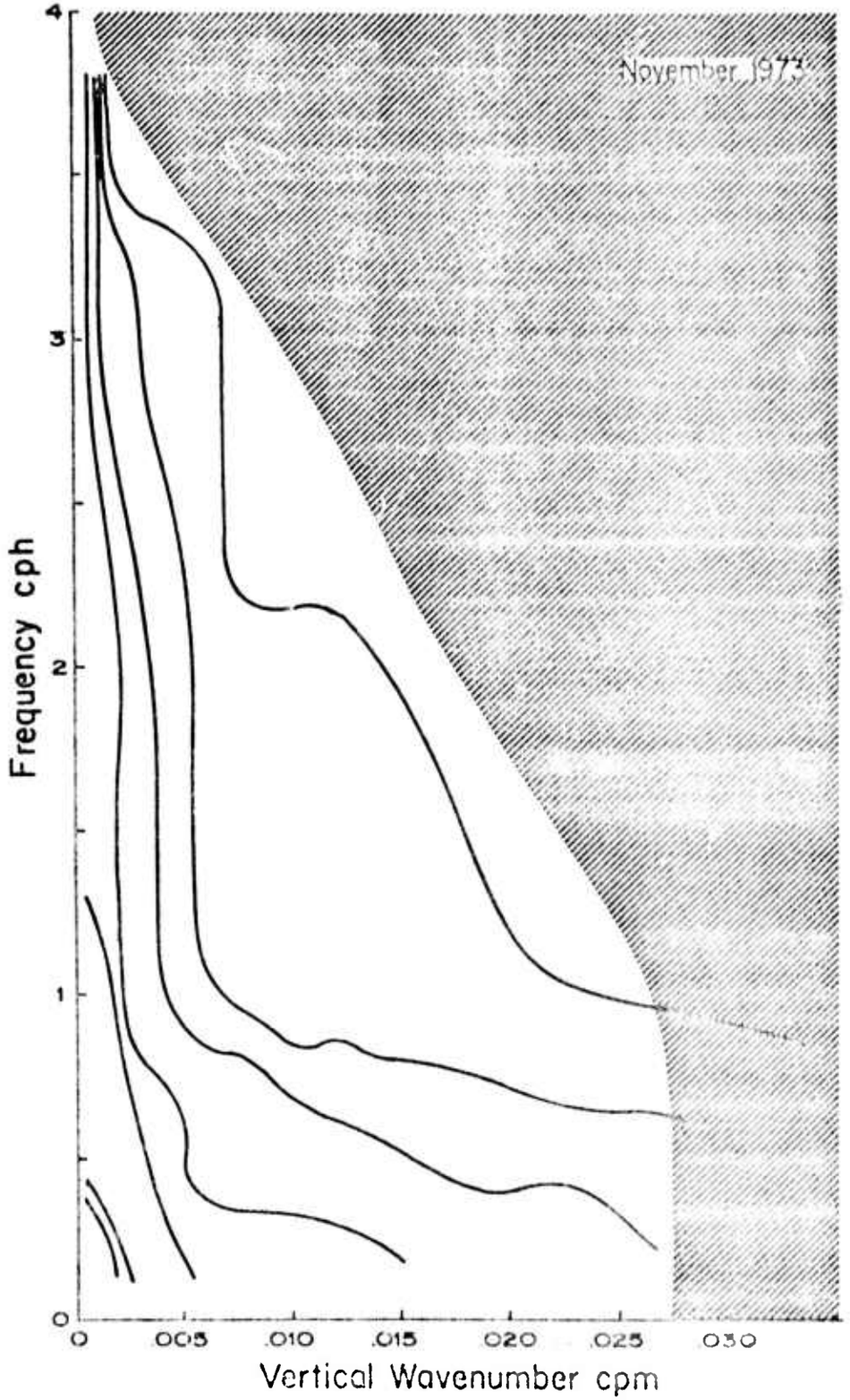

Figure 32. November 1973: Log potential energy versus frequency and W.K.B. vertical wavenumber. Contour interval is 5 db down from 10^4 ergs/cm^3/cph cpm. Slashed region is probably contaminated by leakage of low wavenumber energy.

Above 2 cph, a fixed vertical wavenumber bandwidth corresponds to a decreasing number of modes with increasing frequency. This is reflected in the increase in vertical coherence mentioned in the preceeding section.

It should be pointed out that energy in spectral regions of low phase velocity

$$\text{Cph} \equiv \frac{\Omega}{k_H} \quad 10 \text{ cm/sec}$$

might be significantly Doppler shifted. The energy must be severely shifted before any major change in the general spectral pattern occurs.

It is important to check these spectral estimates for consistency with other, independent experimental evidence. Simulated "towed spectral estimates" can be generated from Figures 27 and 29 by integrating the energy in each k_H band and dividing by k_H to convert from radial to linear co-ordinates. The assumption of horizontal directional isotropy is necessary here. The simulated towed spectra are presented in Figure 33. They have a $|k_x|^{-2}$ slope at low wavenumber, which steepens slightly for wavenumbers larger than .5 cycles per kilometer. These simulated results compare remarkably well with the towed spectra of Eli Katz (personal communication).

A second check can be made using the isotherm slope spectrum

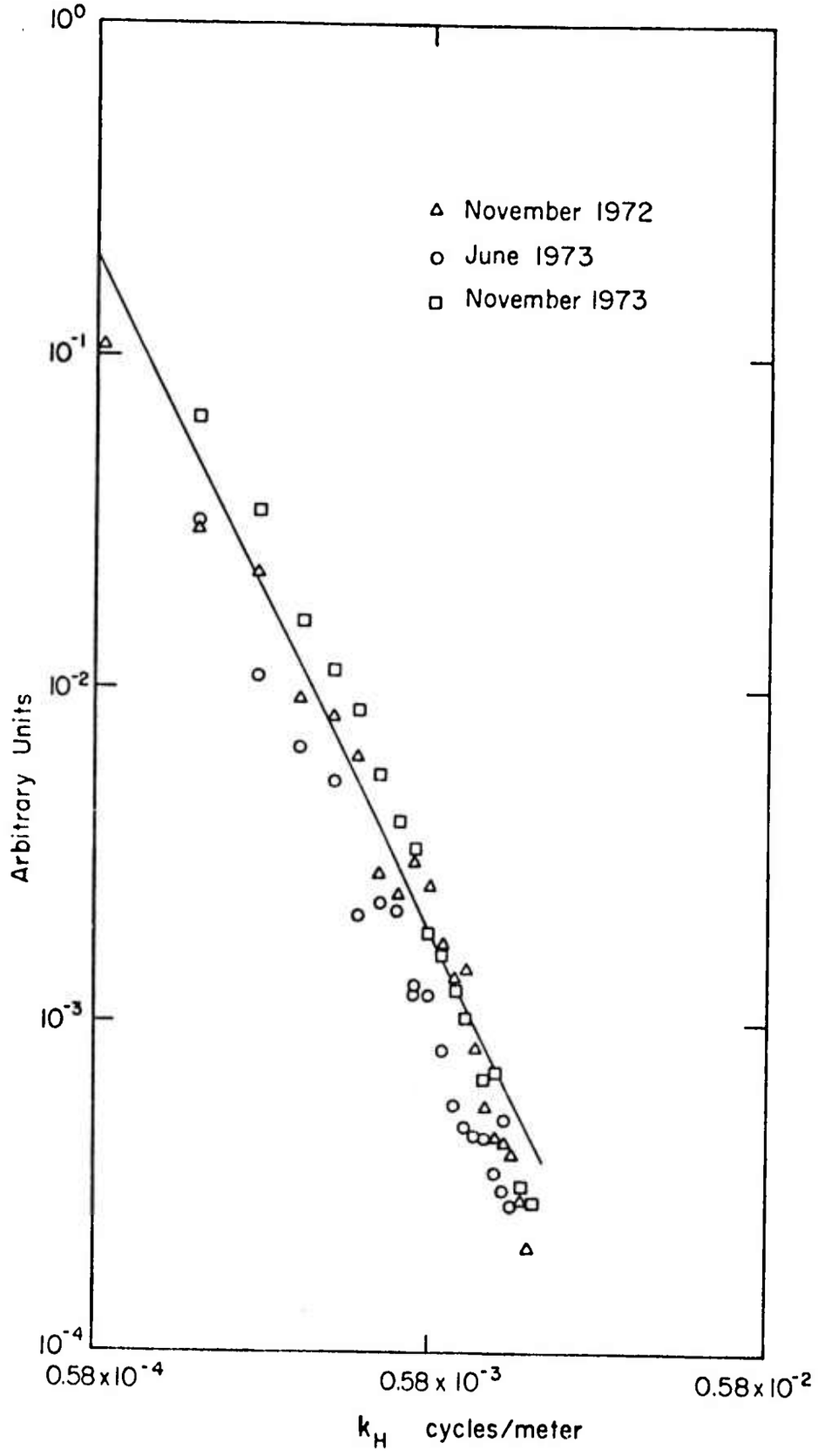

Figure 33. Simulated horizontal towed spectrum, energy/cpm derived from $E_k(\Omega)$. A k_H^{-2} reference line is drawn.

$$\langle \left(\frac{\partial \eta}{\partial x}\Omega\right)^2 \rangle \equiv \int_{\kappa} \int_{\theta} (\kappa \cos\theta)^2 dE(\kappa,\theta,\Omega)\, W^2(\kappa,\Omega,z).$$

Such a spectrum is obtainable from measurement of the tilt of isothermal surfaces, using the three profiling units on FLIP. They will be presented in the next section. Due to the κ^2 weighting, this spectrum is very sensitive to the short wavelength energy levels in a given frequency band.

Figure 34 presents the simulated slope spectra generated by performing the weighted integration of $E_k(\Omega)$. The spectral levels are underestimates, as the k integration was terminated at large k when the vertical spectral window $W_{k\kappa}(\Omega)$ indicated that the quality of $E_k(\Omega)$ was suspect. This potential underestimation is most significant in the lowest and highest frequency bands. Horizontal isotropy was again assumed, to perform this conversion.

An approximate Ω^{-1} slope is given by the simulation. This contrasts with the Garrett and Munk (1972) spectrum which predicts a white slope spectrum, independent of the number of modes chosen. Similarity between the slope spectral estimates to be presented and the simulated spectra will give confidence in the accuracy of the vertical separation.

The Isotherm Slope Spectrum

The isotherm slope spectrum

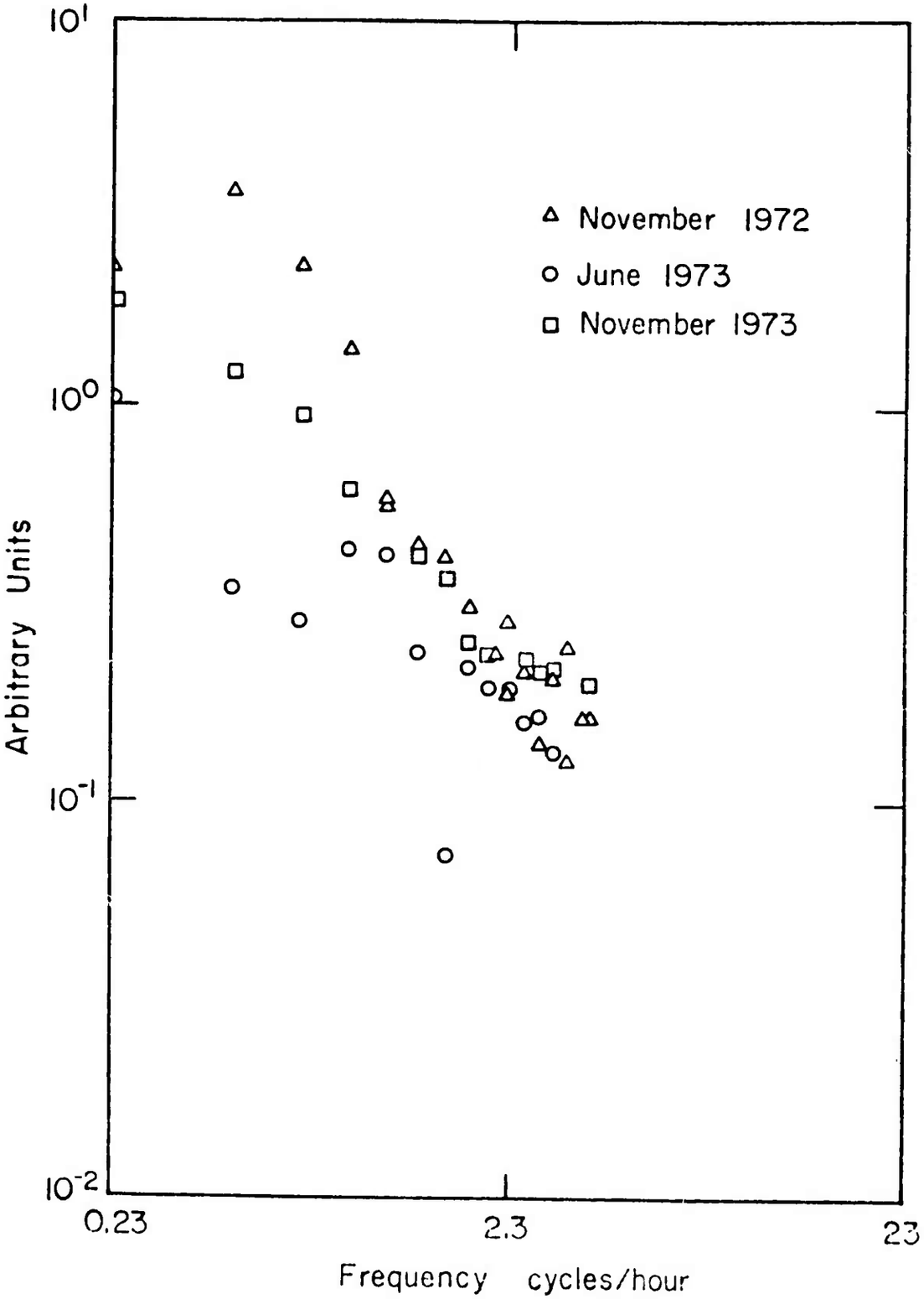

Figure 34. Simulated isotherm slope spectra, cph^{-1} versus frequency derived from $E_k(\Omega)$.

$$\hat{SL}_x(z,\Omega) \equiv \langle \left| \frac{\partial n}{\partial x} (\bar{x},z,\Omega) \right|^2 \rangle$$

is given in terms of the equivalent continuum representation by

$$\hat{SL}_x(z,\Omega) = \int_\kappa \int_\theta (\kappa \cos\theta)^2 \langle dAdA^* (\kappa,\theta,\Omega) \rangle W^2 (\kappa,\Omega,z) .$$

An approximation to the slope spectrum can be obtained from the present data by assuming

$$\frac{\partial n}{\partial x}(\bar{x},z,\Omega) \cong \frac{n(x_1,z,\Omega) - n(x_2,z,\Omega)}{|\bar{x}_1 - \bar{x}_2|} .$$

The approximate slope spectrum has the form

$$SL_x(z,\Omega) = \frac{4}{|\bar{x}_1 - \bar{x}_2|^2} \int_\kappa \int_\theta \sin^2\left(\kappa\left(\frac{|\bar{x}_1 - \bar{x}_2|}{2} \cos\theta\right)\right)$$

$$\langle dAdA^*(k,\theta,\Omega) \rangle W^2(\kappa,\Omega,z) .$$

For wavelengths long compared to the probe separation

$$\sin^2\left(\kappa \frac{|\bar{x}_1 - \bar{x}_2|}{2} \cos\theta\right) \approx \kappa^2 \frac{|\bar{x}_1 - \bar{x}_2|^2}{4} \cos^2\theta$$

and the approximation is good. Were appreciable energy concentrated in wavelengths of the same order as the array separation length or

smaller, the approximate slope spectrum would tend to underestimate the true spectrum.

Typical approximate slope spectra are presented from the November 1972 cruise in Figure 35. The slopes are taken with respect to the mean downwind and mean crosswind directions. Below 1 cph the spectrum has an $\Omega^{-1/2}$ frequency dependence. Above this frequency there is a spectral shoulder of lesser slope. At frequencies far above the Vaisala frequency, the spectrum is white. A pronounced cutoff is not apparent. There is no apparent systematic variation of the slope spectrum either with direction or depth which is present in all three cruises.

The general form of the slope spectrum is quite similar to the simulated slope spectrum inferred in the previous section from the vertical variability of the data. The discrepancy between the spectrum and the Garrett-Munk 1972-74 models, which predict an Ω^{0} spectral form might reflect the slight increase in the low frequency, high mode energy discussed in the previous section, and not included in the models. Garrett and Munk emphasize that this is an "isotherm depth difference" spectrum, not a true slope spectrum. The Garrett-Munk 1974 isotherm difference spectrum has an approximate Ω^{-1} slope in the intermediate frequency range and agrees reasonably well with this spectrum (Garrett and Munk, personal communication).

An Estimate of Horizontal Wavenumber

Figure 36 presents an isotherm displacement spectrum and an isotherm

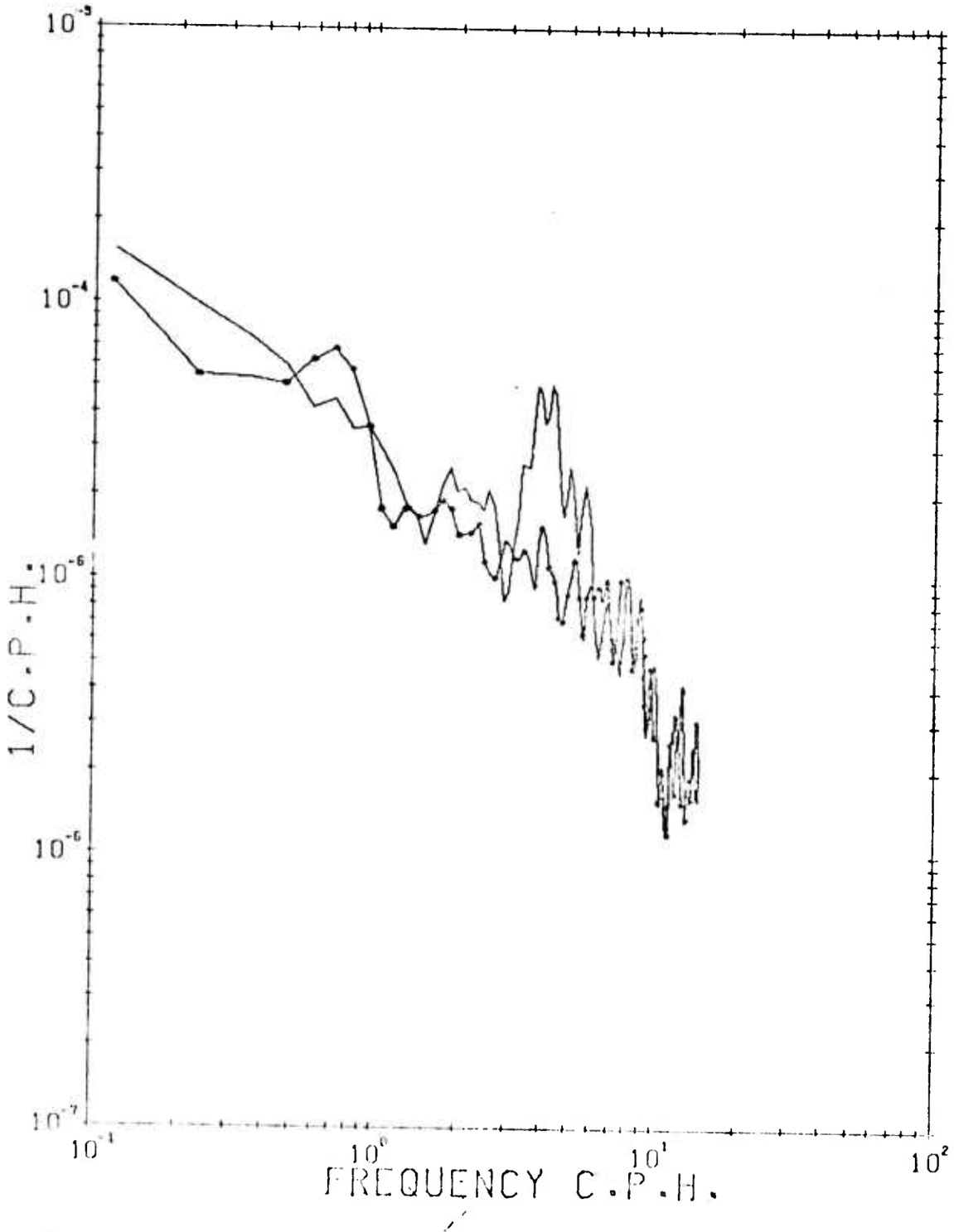

Figure 35. Isotherm slope spectra, 48 df. Dotted line: slope in mean crosswind direction. Smooth line: slope in downwind direction.

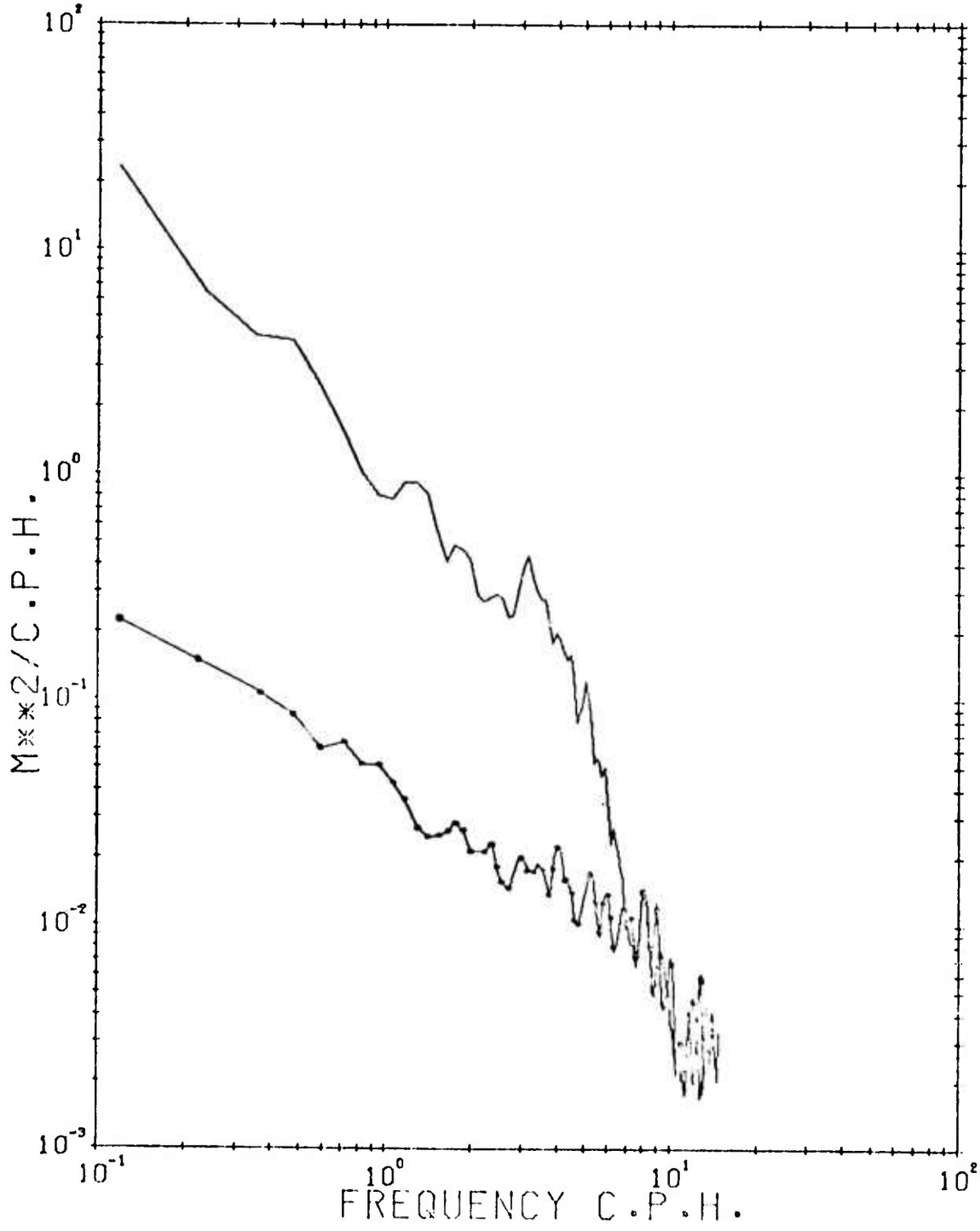

Figure 36. November 1972: Isotherm displacement spectrum and crosswind difference spectrum, 48 df.

difference spectrum from the November 1972 cruise. A comparison of the spectral forms provides some information on the wavenumber dependence of the spectrum.

A horizontal wavenumber estimate can be defined

$$\kappa_x(z,\Omega) = [SL_x(z,\Omega)/S(z,\Omega)]^{1/2}$$

$$\kappa_x(z,\Omega) = \frac{\int\int_{\kappa\ \theta} (\kappa\cos\Omega)^2 \langle dAdA^* \rangle W^2}{\int\int_{\kappa\ \theta} \langle dAdA^* \rangle W^2}^{1/2}$$

for each frequency and depth. The relationship between this horizontal wavenumber estimate and the wavenumber dependence of the spectrum is precise only in the case of uni-modal propagation

$$dE(\kappa,\theta,\omega) = dE(\theta,\omega)\ \delta(\kappa - \kappa(\omega)).$$

Here $\kappa = \kappa(\omega)$.

It is useful to consider two other cases. Were the spectrum in a given frequency band directionally isotropic, constant between wavenumbers κ_{min} and κ_{max}, and zero elsewhere, the resulting scale wavenumber magnitude would be.

$$\kappa_H = (\kappa_x^2 + \kappa_y^2)^{1/2} = (\frac{1}{3}(\kappa_{max}^2 + \kappa_{min}\kappa_{max} + \kappa_{min}^2))^{1/2}.$$

A second isotropic spectral model, with a κ^{-2} dependence between wavenumbers κ_{min} and κ_{max} and zero elsewhere, is associated with scale horizontal wavenumber

$$\kappa_H = (\kappa_{min}\ \kappa_{max})^{1/2} .$$

Figures 37-39 portray κ_H versus frequency for the November 1972 cruise. Isotherm information from mean depth 220 m was used. The first ten dispersion lines are also drawn on the plots. Below 3 cph the wavenumber increases slowly with frequency, then more rapidly, following the first mode dispersion line When Ω exceeds N, the estimate becomes erratic.

Using the models introduced above, an estimate can be made of the bandwidth of energetic wavenumbers. If it is assumed that κ_{min} is given by the first mode dispersion line, then the variation of κ_{max} is sketched in Figure 40. The dominance of the first mode above 3 cph and the general widening of the wavenumber bandwidth below are apparent in both models. However, due to the oversimplified form of the assumed wavenumber dependencies, neither model depicts the wavenumber bandwidth variation accurately in the lower frequency region.

Horizontal Coherence

Horizontal coherence measurements have been utilized by other experimenters to provide an indirect estimate of the

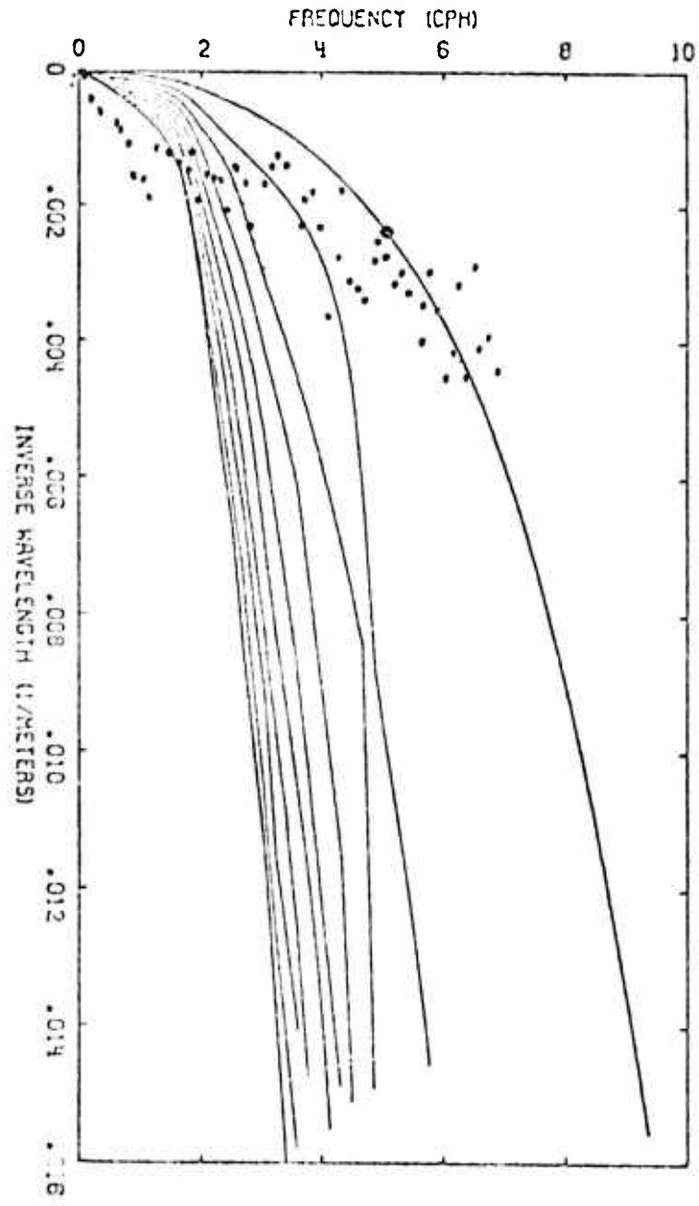

Figure 37. Horizontal wavenumber magnitude versus frequency.

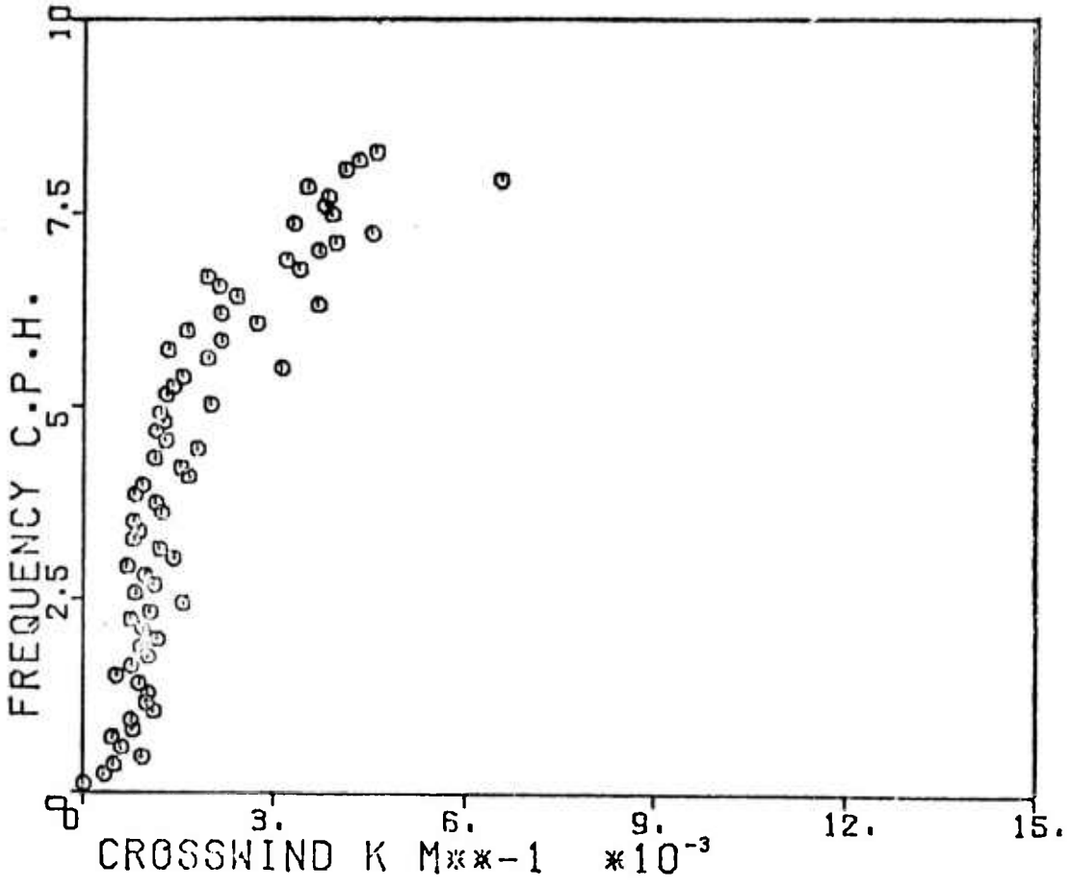

Figure 38. November 1972: Crosswind component of horizontal wavenumber

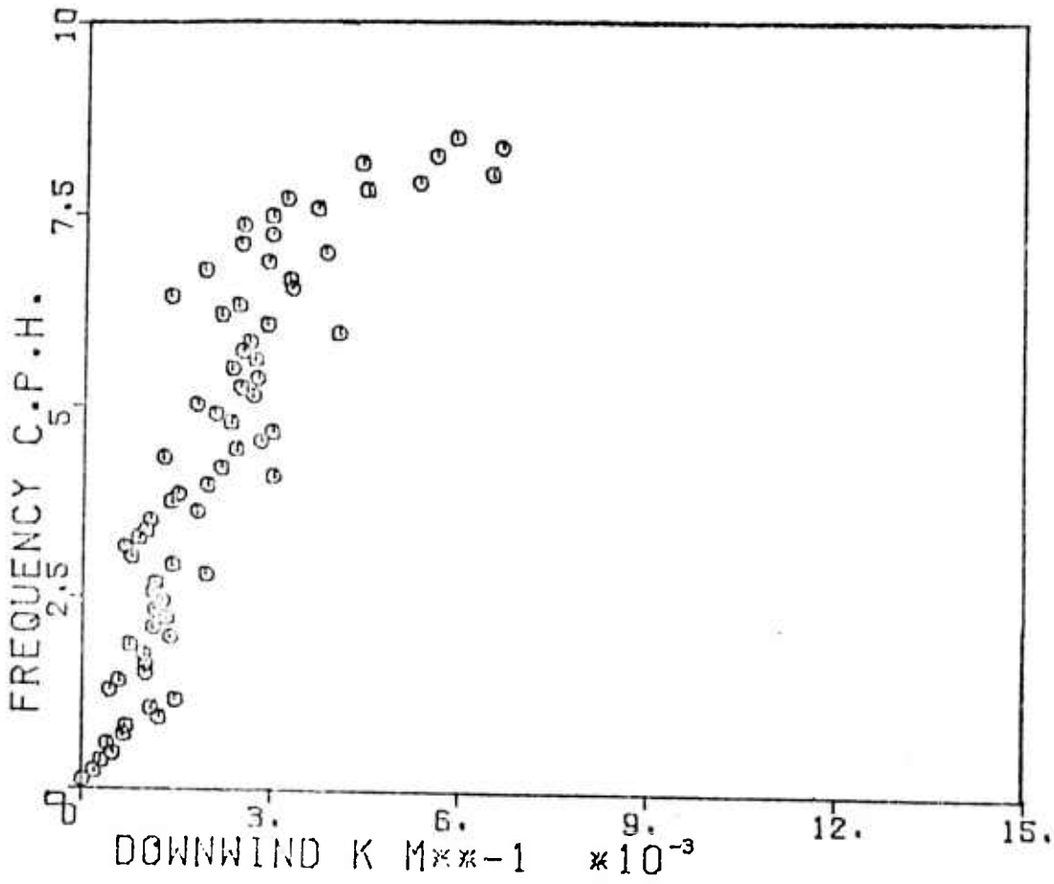

Figure 39. November 1972: Downwind component of horizontal wavenumber

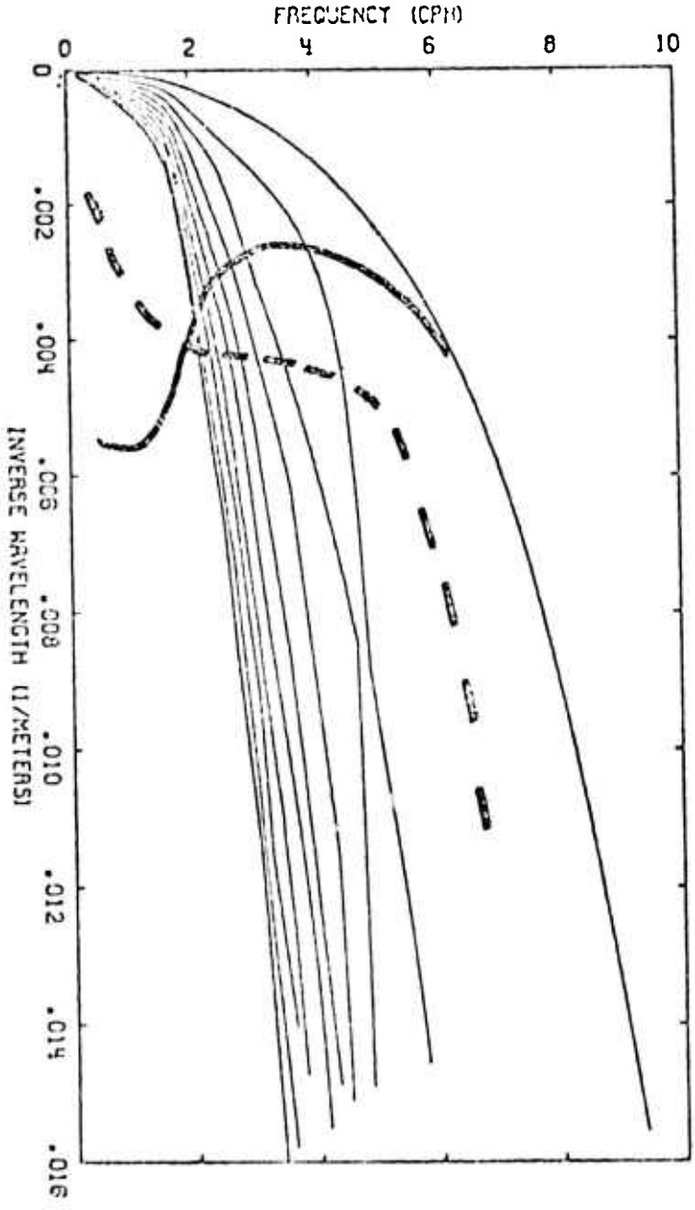

Figure 40. Sketch of κ_{max} versus frequency for κ_{min} given by first mode dispersion line, and representative data, κ_H. Solid line: κ^{-2} model; dashed line: κ^0 model.

horizontal wavenumber dependence of the spectrum. In the present case, these measurements are of somewhat limited value. The horizontal dimensions of the array are sufficiently small compared to typical internal wave scales that high coherences are measured at all frequencies where waves are present. The significant information on the wavefield is given by small deviations of the coherence from 1. A noise/signal ratio which is acceptable for measurements where lower coherences are expected might strongly affect the interpretation of high coherence measurements.

Figure 41 presents an estimate of the horizontal coherence squared between 5.6 hour records of the 14° isotherm depth fluctuation as followed by the port and starboard probes (separation 44 m). This particular data run was rapidly sampled, the Nyquist frequency being 45 cycles per hour. The associated displacement spectrum is given in Figure 8. The squared coherence is statistically insignificant above the Vaisala frequency and nearly unity from the cutoff down to approximately three cycles per hour. Below this frequency the value drops corresponding to the increased horizontal wavenumber bandwidth discussed in the preceeding section. Presumably the squared coherence should then rise toward lower frequencies. The poor resolution and stability of this record obscures any significant low frequency rise.

A contour plot of horizontal coherence squared versus depth and frequency is presented in Figure 42. Three days of data from the Hawaii cruise were utilized to produce this 28 degree of freedom

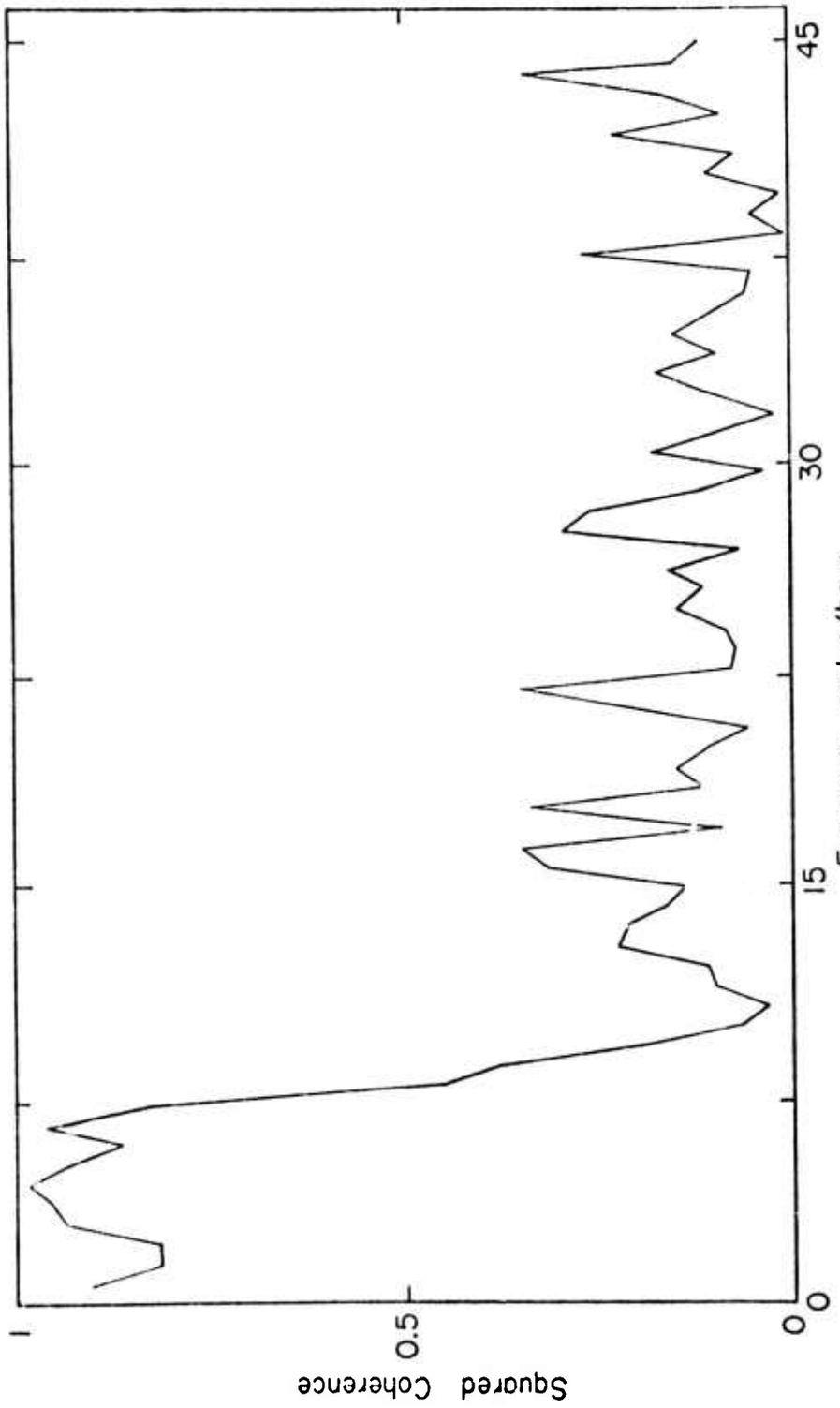

Figure 41. Horizontal coherence squared versus frequency, probe separation 30 meters, 16df.

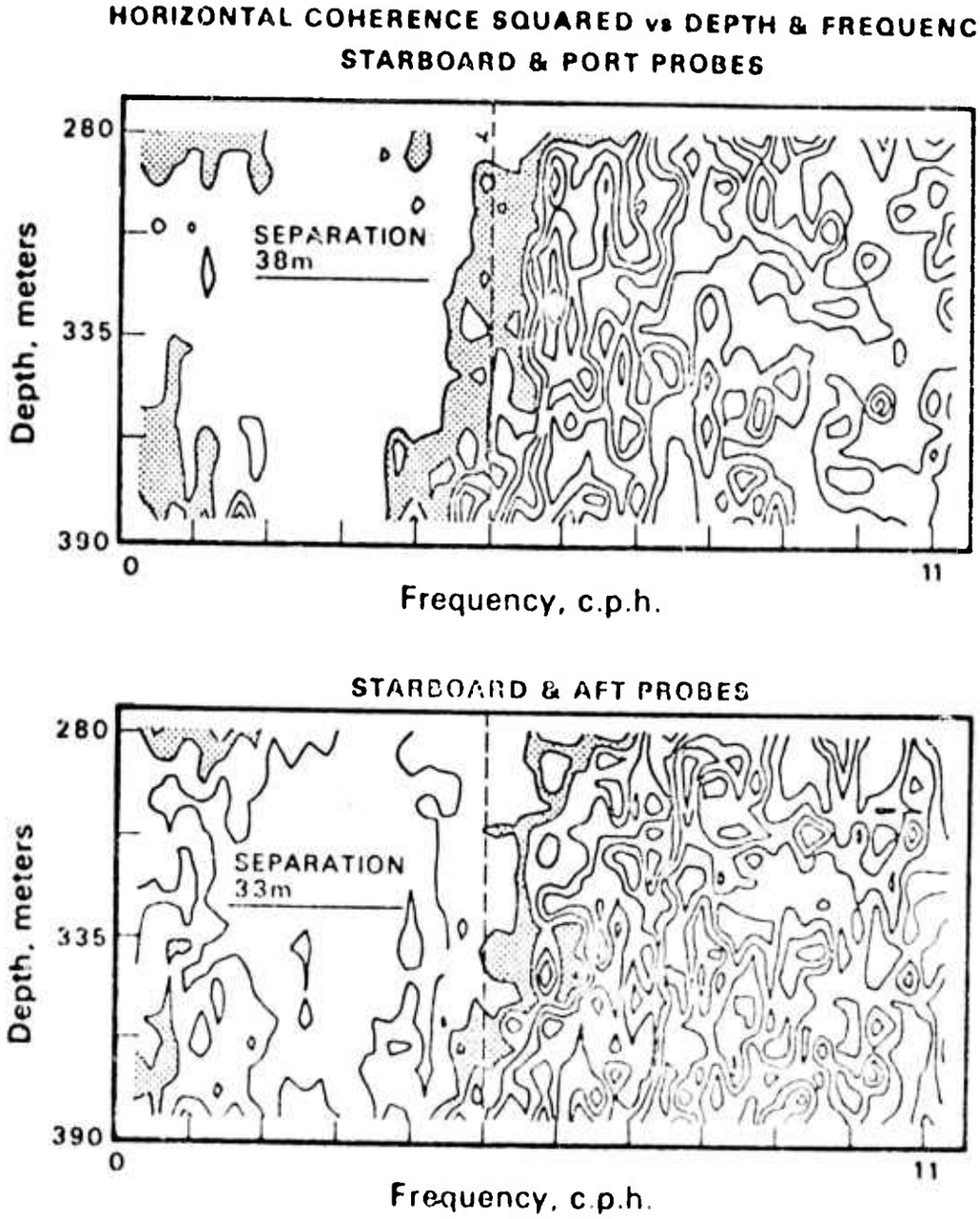

Figure 42. Horizontal coherence squared versus depth and frequency, 28 df. Shaded region represents coherence squared between .7 and .8.

estimate. The depth variability of the high frequency Vaisala cut-off is quite apparent. The squared coherence between the starboard and aft probes, which lie along FLIP's drift path, tend to cut off at a slightly higher frequency than between the starboard and port probes, which are somewhat more perpendicular to the drift direction. This effect could be a manifestation of the Doppler shifting of the measurements, or a result of short term (3 day) anisotropy of the wave field.

Given the marginal statistical stability of these estimates, only the most general conclusions can be drawn. Below 3 cph, the squared coherence across the array is approximately .7-.8, indicating a relatively wide range of horizontal wavenumbers. Above 3 cph the squared coherence tends to be greater than .9, suggesting a very narrow range of energetic wavenumbers. This supports the vertical coherence measurements, which strongly suggest that many modes are important at the low frequencies, while the first few modes dominate the spectrum in the higher frequency region.

An Investigation of Internal Wave Dispersion

In the discussion of the preceeding sections, it has been assumed that the observed motions were linear internal waves. An attempt will now be made to establish the validity of this assumption.

It should be noted that the general analysis approach has not been dependent on the fact that the motions are internal waves. The vertical separation parameter k_H was introduced as an independent

variable characterizing the oscillations of a convenient set of orthogonal functions, $W_k(\omega,z)$. Only if linear internal wave theory well relates the horizontal, vertical and temporal scales of the motions, should the parameter k_H physically correspond to a horizontal wavenumber. Using information from the three profilers on FLIP, direct estimates of horizontal wavenumber, $\hat{\kappa}$, will now be calculated, for each Ω,k band. In those regions of the wavenumber frequency domain in which $\hat{\kappa} \simeq k_H$, linear internal wave theory presumably provides a meaningful approximate characterization of the motions.

Central to this discussion is the vertically separated horizontal cross spectrum

$$VCR_k\ (\Omega,\Delta x_{ij})$$

which is obtained in a manner analogous to the vertically separated wavenumber spectrum $E_k(\Omega)$ (Appendix III). Combining these two spectra, a vertically separated slope spectrum

$$SL_k(\Omega,\Delta x_{ij}) = (2\ E_k(\Omega) - 2\ \text{Real}\ (VCR_k(\Omega,\Delta x_{ij})))\ \Delta x_{ij}^{-2}$$

can be obtained. The ratio of the slope spectrum to the energy spectrum will be used to estimate a horizontal wavenumber, κ, in the manner discussed previously.

Horizontal wavenumber magnitude estimates $\hat{\kappa}(k,\Omega)$ are presented for several frequency bands in Figures 43-45. The vertical scale in the figures is not k_H but the W.K.B. mean vertical wavenumber

$$k_z = k_H \left(\frac{\bar{N}^2 - \Omega^2}{\Omega^2 - f^2}\right)^{1/2}$$

Reference lines $\hat{\kappa} = k_H$ are also plotted for each frequency band. Agreement between measured wavenumbers and linear theory is quite good. The wavenumber ratio $k_z/\hat{\kappa}$ is approximately constant at a given frequency, as emphasized by Eckart (1960). The frequency variation of the wavenumber ratio

$$k_{z,\hat{\kappa}} = \left(\frac{\bar{N}^2 - \omega^2}{\omega^2 - f^2}\right)^{1/2}$$

is also clearly apparent.

The horizontal beamwidth of the wavefield can be related to the vertically separated squared horizontal coherence

$$R_k^2(\Omega,\Delta x_{ij}) = \frac{|VCR_k(\Omega,\Delta x_{ij})|^2}{E_k(\Omega,x_1)\,E_k(\Omega,x_j)}$$

as discussed by Munk and Phillips (1968). For small k, the coherence across the array was found to be quite high at all

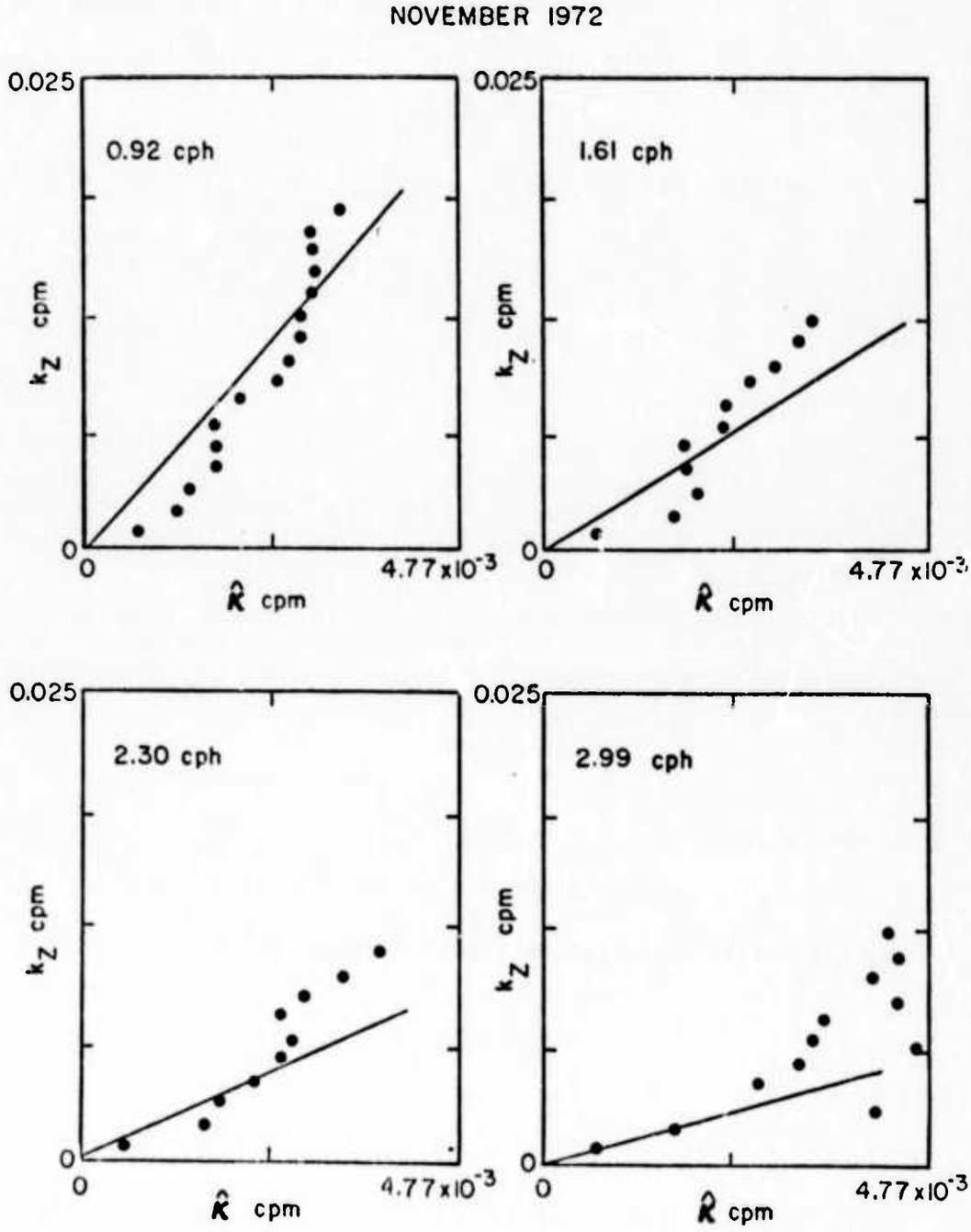

Figure 43. November 1972: Horzontal wavenumber magnitude versus W. K. B. vertical wavenumber. Solid line gives theoretical relation $k_H = \kappa$.

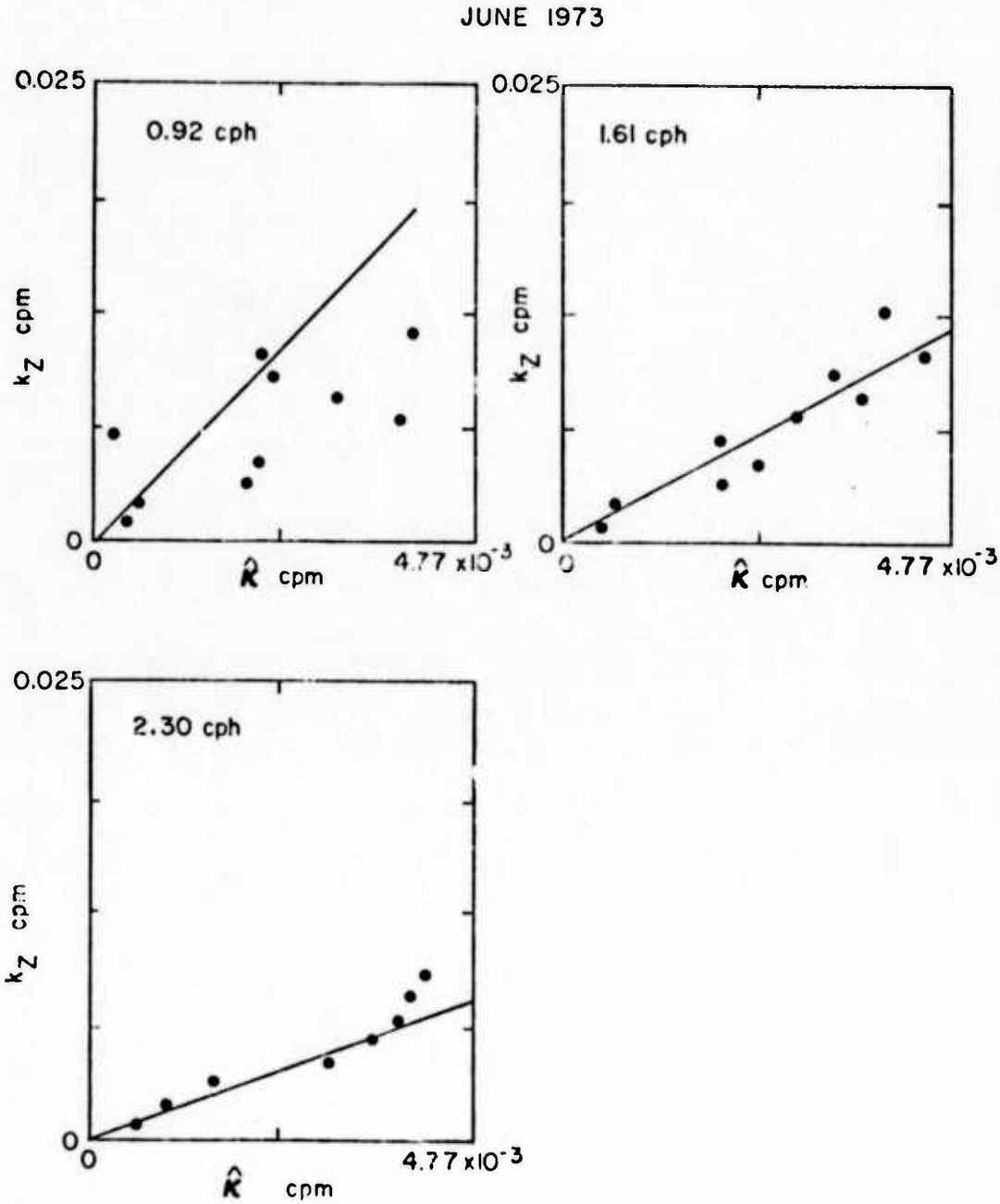

Figure 44. June 1973: Horizontal wavenumber magnitude versus W. K. B. vertical wavenumber. Solid line gives theoretical relation $k_H = \kappa$.

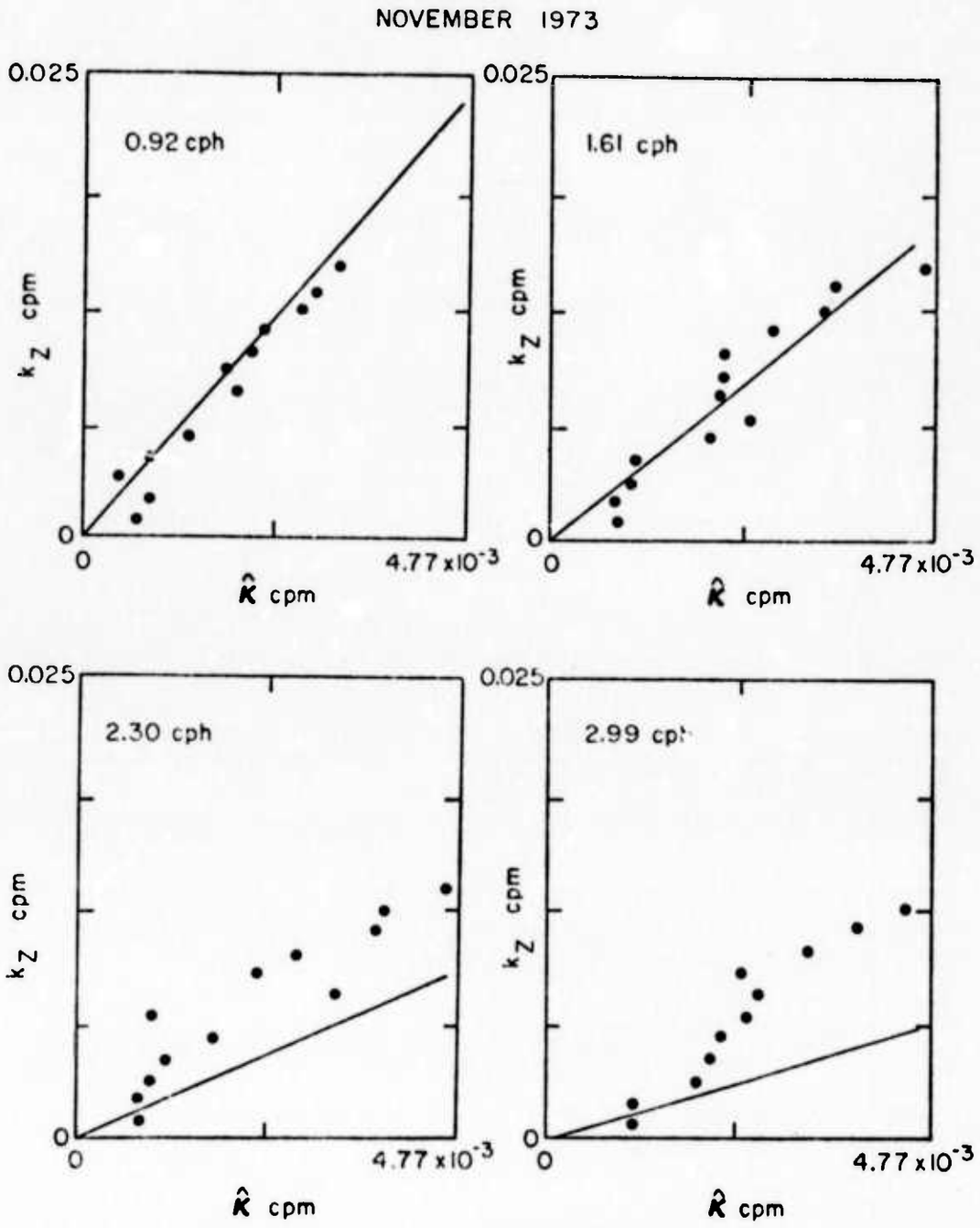

Figure 45. November 1973: Horizontal wavenumber magnitude versus W. K. B. vertical wavenumber. Solid line gives theoretical relation $k_H = \kappa$.

frequencies. With decreasing vertical wavelength it dropped rapidly. The coherence was frequently below that expected from an isotropic spectrum with energy concentrated at wavenumber k_H. The values were consistent with a modeled isotropic spectrum with energy restricted to some thin annular ring about k_H. This is reasonable, considering the finite resolution of the vertical array. Instrument noise, imprecision in the analysis, and other experimental difficulties must also play a role in reducing the coherences.

Given the low coherences, there is no way to determine any departure from isotropy in the signal. Therefore, no extensive effort was made to determine the θ dependence of the spectrum.

A previous study of the high frequency waves ($\Omega > 3$ cph), not presented here, demonstrated significant anisotropy over 1 day time periods. Directional beamwidths of 90° to 180° were found to characterize the predominantly first mode motions.

CHAPTER IV

CONCLUSIONS

Above a minimum horizontal phase velocity, 5-10 cm/sec, the observed isothermal motions could be well represented by a continuous spectrum of internal waves. The dispersion properties of these motions agreed with linear theory to within experimental accuracy. Below this minimum phase velocity, which corresponds to a minimum vertical wavelength $\lambda_z \approx 40$ m at low frequency, $\lambda_z \approx 100$ m at high frequency, the motions could not generally be successfully decomposed in terms of internal wave vertical wave functions exhibiting the dispersion properties predicted by linear theory.

At frequencies far above inertial, the internal wave spectrum can be divided into two regions, according to frequency. Horizontal coherence measurements suggest that the horizontal wavenumber bandwidth is narrow above ~ 2 cph, somewhat wider below. In the lower frequency region, the frequency dependence of the spectrum is ω^{-2}. Both the vertical coherence and horizontal slope spectrum suggest that the wavenumber bandwidth decreases with decreasing frequency.

In this frequency range, the horizontal wavenumber dependence of the wavenumber frequency spectrum can be discussed in terms of three distinct regions. At the lowest wavenumbers, there is a κ^{-2}

slope. This levels into an approximate $\kappa^0 - \kappa^{-1}$ spectral shoulder. The spectrum then decreases rapidly again at higher wavenumber into a region that is dominated by analysis noise.

These measurements do not preclude the Garrett and Munk (1972) suggestion that there is a fourth region of κ^0 slope, which embraces the first several modes (which cannot be resolved by this array).

The discovery of the $\kappa^0 - \kappa^{-1}$ region of short wavelength, low frequency energy is one of the more important results of this experiment. The prominence of the "shoulder" appears to decrease with increasing energy in the wavefield. This spectral adjustment possibly acts in such a manner that equilibrium shear levels in each frequency band are maintained. Low frequency, high mode energy has been suggested by Kenyon (1968) to result from internal wave nonlinear interaction. Cox and Sandstrom (1962) have predicted the existence of very high mode energy as a result of the sea floor scattering of barotropic motions. On the other hand, this shoulder might be the spectral signature of horizontally advecting features in the temperature field which do not correspond to density perturbations. However, as the motions marginally satisfy the internal wave dispersion relation in this spectral region, it is doubtful that advective effects have completely dominated the spectrum. Further work will have to be done to understand the role of this low frequency, short wavelength energy in the dynamics of the sea.

Above ~2 cph, the waveguide thickness decreases with

increasing frequency. In this region, the first mode becomes increasingly prominent with greater frequency, as reflected in the vertical coherence calculations as well as the vertical spectral separation. The displacement spectrum and slope spectrum have irregular slopes, due to the intermode interference discussed in Chapter III.

Given the low values of horizontal coherence measured across the array and the long horizontal wavelengths of the motions studied, it is not possible to detect any significant degree of directionality in the wavefield over 10 day periods. However, this conclusion of isotropy might result from experimental noise which also acts to reduce the coherence.

Although not discussed in this work, significant anisotropy was detected in the high frequency (ω > 3 cph) motions over 1 day records.

A further experiment is suggested, utilizing measurements of density, not temperature, and sufficient flowmeter lowerings such that a clear picture of the mean current shear can be formed. The study of relationships between slope spectral levels, mean shear, and regions in which the density profile is rapidly evolving would greatly increase understanding of upper ocean dynamics.

ACKNOWLEDGMENTS

The research was carried out under guidance of Professors Russ Davis and Fred Spiess. The method utilized for the vertical spectral analysis in Chapter III was the suggestion of Professor Davis. Discussions with Professors Charles Cox, Water Munk and Chris Garrett were most helpful.

The design and construction of the mechanical components of this experiment was supervised by Mr. Bill Davy, Marine Physical Laboratory (MPL). The safe operation of the system at sea is a result of the ideas and support of the FLIP crew led by Mr. Richard Silva and Mr. DeWitt Efird of MPL. Initial electrical design was done by M. Earl Squier, MPL, and Mr. William Whitney, MPL. The author would particularly like to thank Mr. Larry Occhiello who assumed responsibility for the electrical engineering of the experiment and spent approximately six months at sea with the author during the development and operation of the system.

Financial support for the study was provided by the Advanced Research Projects Agency of the Department of Defense and was monitored by the Office of Naval Research under Contract Number N00014-69-A-0200-6041, NR 260-104.

REFERENCES

Cairns, J. L., in press, Internal wave measurements from a midwater float. J. Geophys. Res.

Cox, C. S. and Sandstrom, H., 1962, Coupling of internal and surface waves in water of variable depth. J. Oceanographic Soc. of Japan, 20, 499-513.

Eckart, C., 1960, Hydrodynamics of Oceans and Atmospheres. Pergamon Press, New York.

Garrett, C. J. R. and Munk, W. H., 1971, Internal wave spectra in the presence of fine structure. J. Phys. Oceanog., 1, 196-202.

Garrett, C. J. R. and Munk, W. H., 1972, Space-time scales of internal waves. Geophys. Fluid Dyn., 3(3) 225-264.

Garrett, C. J. R. and Munk, W. H., in press, Space-Time scales of internal waves: A progress report. J. Geophys. Res.

Kenyon, K. E., 1968, Wave wave interactions of surface and internal waves. J. Mar. Res., 26(3) 208-231.

Munk, W. H. and Phillips, N., 1968, Coherence and band structure of inertial motion in the sea. Rev. Geophys., 6, 447-472.

Munk, W. H., Snodgrass, F. and Gilbert, F., 1964, Long waves on the continental shelf. J. Fluid. Mech., 20, part IV, 529-554.

Phillips, O. M., 1971, On spectra measured in an undulating layered medium. J. Phys. Oceanogr., 1, 1-6.

Rattray, M. Jr., Dworski, J. G. and Kovala, P. E., 1969, Generation of long internal waves at the continental slope. Deep-Sea Res., Supplement of 16, 179-195.

Seidler, G., 1971, Vertical coherence of short periodic current variations. Deep-Sea Res., 18, 179-191.

Squier, E. D., 1967, A variable frequency thermometer. Marine Physical Laboratory Technical Memoranda 183.

Stokes, G., 1847, On the theory of oscillatory waves. Cambridge Trans. 8, Paper I, page 212.

Voorhis,A., 1968, Measurements of vertical motion and the partition of energy in the New England slope water. Deep-Sea Res., 15, 599-608.

Webster, T. F., 1972, Estimates of th- coherence of ocean currents over vertical distances. Deep-Sea Res., 19, 35-44.

White, R. A., 1967, The vertical structure of temperature fluctuations within an oceanic thermocline. Deep-Sea Res., 14, 613-623.

Wunsch, Carl, 1968, On the propagation of internal waves up a slope. Deep-Sea Res., 15, 251-258.

Wunsch, Carl and Hendry, Ross, 1972. Array measurements of the bottom boundary layer and the internal wave field on the continental slope. Geophys. Fluid Dyn., 4, 101-145.

LIST OF SYMBOLS

$\bar{x}$	horizontal coordinate
z	vertical coordinate
t	time
$\bar{u}(\bar{x},z,t)$	horizontal velocity
$w(\bar{x},z,t)$	vertical velocity
$\eta(\bar{x},z,t)$	vertical displacement
D	depth interval spanned by array - typically 60-440 m.
H	depth of ocean
$T(\bar{x},z,t)$	temperature
$\rho(z)$	density
$N(z)$	Vaisala frequency
c	velocity of sound
ω	intrinsic frequency
Ω	encounter frequency
f	inertial frequency
κ	horizontal wavenumber
C_p	horizontal phase velocity
$W(\kappa,\omega,z)$	linear, shear free internal wave vertical wavefunction
k	dimensionless independent parameter characterizing the oscillatory behavior of a set of vertical internal wavefunctions $W_k(\omega,z)$ used to decompose the vertical variability of the motions
$k_H = \alpha(\omega)k$	dimensional equivalent horizontal wavenumber magnitude: $W_k(\omega,z) = W(k_H,\omega,z)$

$k_z = k_H \left(\frac{\bar{N}^2 - \Omega^2}{\Omega^2 - f^2}\right)^{1/2}$ W.K.B. equivalent vertical wavenumber

$E_p(z)$ r.m.s. potential energy

$E_k(z)$ r.m.s. kinetic energy

$\hat{C}\ (\bar{x}_1 - \bar{x}_2,\ z_1, z_2,\ t_1 - t_2)$ process covariance function

$\hat{C}R(\bar{x}_1 - \bar{x}_2,\ z_1, z_2, \omega)$ process cross spectrum

$CR(\bar{x}_1 - \bar{x}_2,\ z_1, z_2,\ \Omega)$ sample cross spectrum

$dE(\kappa, \theta, \omega)$ three dimensional internal wave spectral function

$dE(\kappa, \omega) = \int_0^{2\pi} dE(\kappa, \theta, \omega)$ two dimensional internal wave spectral function

$E_k(\Omega)$ cph^{-1} cpm^{-1} estimate of $dE(\kappa, \omega)$ in frequency band ω, vertical separation band k

$W_k(\kappa, \Omega) = W_{k\kappa}(\Omega)$ vertical spectral window

$S(z, \Omega) = CR(0, z, z, \Omega)$ m^2/cph vertical displacement frequency spectrum

$V(z, \Omega) = \Omega^2\ CR(0, z, z, \Omega)$ $(\text{cm/sec})^2/\text{cph}$

vertical velocity frequency spectrum

$VC(z_1, z_2, \Omega) = CR(0, z_1, z_2, \Omega)$ vertical cross spectrum

$VC(\Delta z, \Omega)$ vertical cross spectrum vs frequency and W.K.B. stretched separation

$$\Delta z \equiv \frac{1}{\bar{N}} \int_{z_1}^{z_2} N(z)dz$$

$VR^2(\Delta z, \Omega) = \frac{|VC(\Delta z, \Omega)|^2}{VC(0, \Omega)^2}$ vertical squared coherence

$SL_{\bar{x}}(z, \Omega)$ cph^{-1} isotherm slope spectrum

$SH_{\bar{x}}(z, \Omega)$ $\text{sec}^{-2}\ \text{cph}^{-1}$ horizontal shear spectrum

$VCR_k(\Omega,\Delta x_{ij})$	vertically separated horizontal cross spectrum
$SL_k(\Omega,\Delta x_{ij})$	vertically separated slope spectrum
$R^2_k(\Omega,\Delta x_{ij})$	vertically separated horizontal squared coherence

APPENDIX I

THE STATISTICAL DESCRIPTION OF THE MOTION

The data set can be uniquely described by the Fourier-Stieltjes representation

$$\eta(\bar{x},z,t) = \int_{\kappa=0}^{\infty} \int_{\theta=0}^{2\pi} \int_{\omega=-\infty}^{\infty} \widetilde{dA}(\kappa,\theta,\omega,z) e^{i\,\bar{\kappa}\cdot\bar{x} - \omega t}$$

where η is the vertical displacement of an isothermal surface about its mean position and

$$\widetilde{dA}(\kappa,\theta,\omega,z) = \widetilde{dA}(\kappa,\theta+\pi,-\omega,z)$$

in order that η be real valued.

The isotherm displacement variance is given by

$$\langle \eta^2(z) \rangle = \int_{\kappa}\int_{\theta}\int_{\omega} \int_{\ell}\int_{\phi}\int_{\Omega} \langle \widetilde{dA}(\kappa,\theta,\omega,z)\widetilde{dA}(\ell,\phi,\Omega,z) \rangle$$

$$e^{i\,(\bar{\kappa}+\bar{\ell})\cdot\bar{x} - (\omega+\Omega)t}.$$

If $\langle \eta^2(z) \rangle$ is to be stationary in $\bar{x}$ and t, it is necessary that

$$\langle \widetilde{dA}(\kappa,\theta,\omega,z)\widetilde{dA}(\ell,\phi,\Omega,z)\rangle = \langle \widetilde{dA}(\kappa,\theta,\Omega,z)\widetilde{dA}^{*}(\kappa,\theta,\Omega,z)\rangle$$

$$\delta(\bar{\kappa} + \bar{\ell})\,\delta(\omega + \Omega) \ .$$

The motions of primary interest to this study are those with temporal frequency ω less than the local Vaisala frequency $N(z)$. In this case, it is reasonable to separate the vertical dependence of

$$\widetilde{dA}(\kappa,\theta,\omega,z) = \tilde{\widetilde{dA}}(\kappa,\theta,\omega)\ W(\kappa,\omega,z)$$

where W is a solution of the linear, shear free internal wave equation

$$\frac{\partial^2 W}{\partial z^2} + \kappa^2 \frac{(N^2(z) - \omega^2)}{(\omega^2 - f^2)} W = 0$$

where $W = 0$ at $z = 0$ and is normalized such that

$$\frac{1}{2D} \int_{D} \rho(z)\ N^2(z)\ W^2(\kappa,\omega,z)dz = 1.$$

Now the variance is given by

$$\langle \eta^2(z)\rangle = \int_{\kappa}\int_{\theta}\int_{\omega} \langle |\tilde{\widetilde{dA}}|^2\rangle\ W^2(\kappa,\omega,z) \ .$$

With the additional restriction that $W = 0$ at a flat bottom, $z = -H$, the energy is quantized into discrete modes

$$\langle \eta^2(z) \rangle = \sum_i \int_\theta \int_\omega \langle |\tilde{\tilde{dA}}_i(\theta,\omega)|^2 \rangle W^2(\kappa_i,\omega,z)$$

where, for each frequency, the $\{W(\kappa_i,\omega,z)\}$ are an orthogonal set over the interval $(0, -H)$ under the weight function $\left(\frac{N^2 - \omega^2}{\omega^2 - f^2}\right)$.

Garrett and Munk (1972) have suggested that the effects of the particular boundary conditions at the sea surface and bottom are generally unimportant. They then introduced an "equivalent continuum" representation

$$\eta(\bar{x},z,t) \int_\kappa \int_\theta \int_\omega dA(\kappa,\theta,\omega)\, W(\kappa,\omega,z) e^{i\,\bar{\kappa}\cdot\bar{x} - \omega t}$$

such that

$$\int_{\kappa_i}^{\kappa_j} \langle |dA|^2 \rangle W^2(\kappa,\omega,z) = \sum_{\ell=i}^{j} \langle |\tilde{\tilde{dA}}_i|^2 \rangle W^2(\kappa_i,\omega,z) .$$

APPENDIX II

CHOOSING THE ORTHOGONAL FUNCTION SET

For each horizontal position $\bar{x}_j$ there are measured values of $n(\bar{x}_j, z_i, \Omega)$ at forty depths z_i. This complex, nonstationary depth series is to be expanded as a sum of orthogonal functions

$$n(z_i) = \sum_{n=1}^{40} a_n F_n(z_i)$$

with

$$a_n = \int_D n(z) F_n(z) Y(z) dz$$

where F_n is the n^{th} function in the desired orthogonal set and Y is a weight function to be determined.

In order that the potential energy be given by the sum of the squares of the coefficients $\{a_n\}$, it is necessary that

$$\sum_{n=1}^{40} <|a_n|^2> = 1/2\ \rho\ D^{-1} \int_D N^2 <|n|^2> dz$$

$$= 1/2\ \rho\ D^{-1} \int_D N^2 < \sum_{\ell} a_\ell F_\ell \sum_{m} a_m^* F_m > dz$$

$$= 1/2\ \rho\, D^{-1} \sum_{\ell} \sum_{m} \langle a_\ell\ a_m^* \rangle \int_D N^2\, F_\ell\, F_m\, dz\,.$$

This requirement can be satisfied if $\langle a_\ell\ a_m^* \rangle = \langle |a_m|^2 \rangle\ \delta_{\ell m}$

or $\int_D N^2\, F_\ell\, F_m\, dz = \delta_{\ell m}$ where the weight function Y is seen to be N^2.

It will now be demonstrated that, if $\{G_n(z_i)\}$ is the set of eigenfunctions of the N weighted co-spectral matrix

$$\langle N(z_i)\ n(x_o, z_i, \Omega)\ n^*(x_o, z_j, \Omega)\ N(z_j) \rangle$$

then the functions

$$\{F_n(z_i)\} = \{G_n(z_i)/N(z_i)\}$$

are the desired complete orthogonal set.

Write

$$N(z_i)\ n(x_o, z_i, \Omega) = \sum a_n\ G_n(z_i)$$

$$a_n = \int_D N(z_i)\ n(z_i)\ G_n(z_i) dz\ .$$

The N weighted co-spectral matrix can be written

$$\langle N(z_i)\, n(z_i)\, n^*(z_j)\, N(z_j) \rangle = \sum_n \langle |a_n|^2 \rangle\, G_n(z_i)\, G_n(z_j)$$

where from linear algebra we have

$$\sum_i G_n(z_i)\, G_\ell(z_i) = \delta_{n\ell}$$

and

$$\langle a_n\, a_\ell^* \rangle = \langle |a_n|^2 \rangle\, \delta_{n\ell} \rangle = \lambda_n\, \delta_{n\ell}$$

where λ_n is the n^{th} eigenvalue of the matrix. By substitution $F(z) = G(z)/N(z)$, it is seen that

$$n(\bar{x}_j, z_i, \Omega) = \sum_n a_n\, F_n(z_i)$$

$$a_n = \int_D N^2\, n\, F_n\, dz$$

and

$$\int_D F_n\, F_\ell\, N^2 dz = \delta_{n\ell} \ .$$

If the weighted co-spectral matrix has no zero eigenvalues, the $\{G_n(z_i)\}$ are a complete set. It can easily be verified that the $F_n(z_i)$ are also complete, provided that $N(z) > 0$ for all z.

APPENDIX III

A PRIORI OPTIMAL CROSS SPECTRAL SEPARATION

Model the signal as a sum of "modes"

$$n(z_i, x_j) = \sum_{m=1}^{120} A_m(x_j)\, F_m(z_i)$$

and represent it as a sum of eigenfunctions

$$n(z_i, x_j) = \sum_{n=1}^{40} a_n(x_j)\, f_n(z_i)$$

where

$$a_n(x_j) = \int_D n(z_i, x_j)\, f_n(z_i)\, \text{Weight}\,(x_i)dz$$

$$= \int_D \sum_{m=1}^{120} A_m\,(x_j)\, F_m(z_i)\, f_n(z_i)\, \text{Weight}(z_i)sz$$

$$= \sum_{m=1}^{120} A_m(x_j)\, C_{mn}.$$

and

$$C_{mn} = \int_D F_m \, f_n \, \text{Weight} \, dz \, .$$

Now

$$\langle a_n(x_i) \, a_n^*(x_j) \rangle =$$

$$= \sum_{m=1}^{120} \sum_{M=1}^{120} \langle A_m(x_i) \, A_m^*(x_j) \rangle \, C_{mn} \, C_{Mn}$$

$$= \sum_{M=1}^{120} \langle A_m(x_i) \, A_m^*(x_j) \rangle \, C_{mn}^2 .$$

The quantities

$$\langle a_n(x_i) \, a_n^*(x_j) \rangle$$

can be calculated from which we wish to estimate

$$\langle A_m(x_i) \, A_m^*(x_j) \rangle .$$

The estimate is formed as a linear sum

$$\langle A_m(x_i)\, A_m^*(x_j)\rangle = \sum_{\ell=1}^{40} \alpha_{m\ell}\ \langle a_\ell(x_i)\, a_\ell^*(x_j)\rangle$$

$$= \sum_{\ell=1}^{40} \alpha_{m\ell} \sum_{m=1}^{120} \langle A_n(x_i)\, A_n^*(x_j)\rangle\, C_{n\ell}^2$$

$$= \sum_{n=1}^{120} W_{mn}\, \langle A_n(x_i)\, A_n^*(x_j)\rangle$$

The cross spectral window is

$$W_{mn} = \sum_{\ell=1}^{40} \alpha m_\ell\, C_{n\ell}^2$$

which is the same window that is associated with the vertical spectral separation in Chapter III. Thus the same coefficients $\alpha_{m\ell}$ which were used for the optimal vertical separation can be used to form the optimal cross spectral estimate.